DISSERTATION

INVESTIGATING PLASMA MODIFICATIONS AND GAS-SURFACE REACTIONS OF TiO_2-BASED MATERIALS FOR PHOTOCONVERSION

Submitted by

Daniel J.V. Pulsipher

Department of Chemistry

In partial fulfillment of the requirements

For the Degree of Doctor of Philosophy

Colorado State University

Fort Collins, Colorado

Fall 2012

Doctoral Committee:

Advisor: Ellen R. Fisher

C. Michael Elliott
Alan VanOrden
Steven H. Strauss
Azer Yalin

ABSTRACT

INVESTIGATING PLASMA MODIFICATIONS AND GAS-SURFACE REACTIONS OF TiO_2-BASED MATERIALS FOR PHOTOCONVERSION

Plasmas offer added flexibility for chemists in creating materials with ideal properties. Normally unreactive precursors can be used to etch, deposit and modify surfaces. Plasma treatments of porous and compact TiO_2 substrates were explored as a function of plasma precursor, substrate location in the plasma, applied rf power, and plasma pulsing parameters. Continuous wave O_2 plasma treatments were found to reduce carbon content and increase oxygen content in the films. Experiments also reveal that Si was deposited throughout the mesoporous network and by pulsing the plasma, Si content and film damage could be eliminated. Nitrogen doping of TiO_2 films ($N:TiO_2$) was accomplished by pulsed plasmas containing a range of nitrogen precursors. $N:TiO_2$ films were anatase-phased with up to 34% nitrogen content. Four different nitrogen binding environments were controlled and characterized. The produced $N:TiO_2$ films displayed various colors and three possible mechanisms to explain the color changes are presented.

Both O_2 treated and $N:TiO_2$ materials were tested in photocatalytic devices. Preliminary results from photocatalytic activities of plasma treated P25 TiO_2 powders showed that nitrogen doping treatments hinder photocatalytic activity under UV light irradiation, but silicon deposition can improve it. $N:TiO_2$ materials were tested in photovoltaic devices to reveal improved short-circuit current densities for some plasma-modified films.

To understand the gas-phase and surface chemistry involved in producing the N:TiO_2 films, NH and NH_2 species in pulsed NH_3 plasmas were explored by systematically varying peak plasma power and pulsing duty cycle. Results from these studies using gas phase spectroscopy techniques reveal interconnected trends of gas-phase densities and surface reactions. Gas-phase data from pulsed plasmas with two different types of plasma pulsing reveal diminished or increased densities at short pulses that are explained by plasma pulse initiation and afterglow effects. Overall this work reveals characteristics of the plasma systems explored, knowledge of the resulting materials, and control over plasma etching, deposition, and modification of TiO_2 surfaces.

ACKNOWLEDGMENTS

I am grateful for the opportunity to further my knowledge and experience in chemistry and related disciplines. I hunger to learn and develop in the sciences and this program at Colorado State University and my undergraduate program at Idaho State University have allowed me the needed association with great minds and the time for study and reflection. I thank the patience of those who have invested their efforts into my future namely my advisor, Prof. Ellen R. Fisher, Prof. C Michael Elliott, Dr. Patrick McCurdy, Fisher and Elliott group members, my teachers, and my family. I am also grateful for the funding that made this work possible namely: the National Science Foundation, the Center for Revolutionary Solar Photoconversion, and the various teaching assignments offered.

TABLE OF CONTENTS

ABSTRACT……………………………………………………………………...ii

ACKNOWLEDGMENTS…………………………………………………………iv

TABLE OF CONTENTS………………………………………………………..v

LIST OF TABLES………….…………………………………………….....viii

LIST OF FIGURES……………………………………………………………..ix

CHAPTER 1. Introduction……………………………………….……...1

1.1 Plasma Capabilities……………………………………………………1

1.2 Interesting Properties of TiO_2……………………………….……...…5

1.3 Exploring Surfaces…………………………………………………….7

1.4 Evaluating Plasma Systems…………………………….……………..8

1.5 Overview of Research…………………………………………………..10

1.6 References…………………………………………………………………13

CHAPTER 2. Experimental Methods………………………………………….15

2.1 Plasma Processing……………………………………………………15

2.2 Substrate Preparation………………………………………………...18

2.3 Substrate Characterization……………………………………………...20

2.4 Performance Characterization…………………………………………..23

2.5 Optical Plasma Diagnostics ……………………………………………24

2.6 References……………………………………………………………29

CHAPTER 3. O_2 Plasma Treatment of Mesoporous and Compact TiO_2 Photovoltaic Films: Revealing and Eliminating Effects of Si Incorporation…………………………..31

3.1 Introduction……..…………………………………………………31

3.2 Results and Discussion…………………………………………………………34

3.3 Summary……………………………………………………………………..52

3.4 References…………………………….…………………………………...54

CHAPTER 4. Controlled Nitrogen Doping and Film Colorimetrics in Porous TiO_2 Materials Using Plasma Processing……………………………….……………...…….57

4.1 Introduction……..…………………………………………………………57

4.2 Results……………..……………………………….………..…………....61

4.3 Discussion…………...…..……………………………………………….....82

4.4 Summary..………………………….…………………………………….....89

4.5 References…………………………………………………………………90

CHAPTER 5. Examining Preliminary Photocatalytic and Photovoltaic Devices of Plasma Treated TiO_2………………………………………….……………....……95

5.1 Introduction……..…………………………………………………………95

5.2 Results……………………………………………………………………..97

5.3 Discussion…………...…..……………………………………………….111

5.4 Summary..………………………….…………………………………….119

5.5 References………………………………………………………………..121

CHAPTER 6. NH_2 and NH Surface Production in Pulsed NH_3 Plasmas on TiO_2: a Steady-State Probe of Short Pulse Plasmas…………………………….………...….…123

6.1 Introduction……..………………………………………………………..123

6.2 Results……………..……………………………….………..…………..126

6.3 Discussion…………...…..……………………………………………….145

6.4 Summary..………………………….…………………………………….156

6.5 References……………………………………………………………..……158

CHAPTER 7. Research Summary and Perspectives…………………………………160

7.1 Research Summary…………………………………………………………160

7.2 Future Directions…………………………………………………………...162

7.3 References………………………………………………………………….165

LIST OF TABLES

TABLE **PAGE**

2.1 Notation for TiO_2 film treatments……………………………………………………21

2.2 OES wavelengths………………………………………………………………………28

3.1 XPS atomic composition for untreated and O_2 plasma-treated TiO_2 films………….39

4.1 XPS Atomic Concentrations for N:TiO_2 films………………………………………62

4.2 Percent relative peak area for decomposed XPS Ti $2p_{3/2}$ peaks……………………..69

4.3 Comparison of N 1s and Ti 2p XPS atomic percentages…………………………….71

4.4 Tauc bandgaps for modified films…………………………………………………...76

5.1 XPS compositions of NH_3 plasma treated samples………………………………...103

5.2 XPS compositions of O_2 and HMDSO plasma treated samples……………………108

6.1 $S(NH_2)$ and $S(NH)$ measured at different P_p and XPS compositional data…………139

6.2 $S(NH_2)$ and $S(NH)$ measured at different *d.c.* and XPS compositional data……….140

6.3 Relevant gas-phase reactions resulting in NH_2 and NH production………………..144

LIST OF FIGURES

FIGURE **PAGE**

2.1 Inductively coupled reactor schematic……………………………………………….17

2.2 Schematic diagram of the IRIS apparatus…………………………………………25

3.1 XPS O 1s high resolution spectra…………………………………………………36

3.2 XPS O 1s, Ti 2p, Si 2p high resolution spectra coil treated films…………………...38

3.3 XPS atomic concentration data as a function of Ar^+ sputter time…………………...43

3.4 O 1s XPS high resolution spectra acquired during sputtering experiments…………45

3.5 Langmuir probe data as a function of applied rf power……………………………...47

3.6 Si/O ratio as determined by XPS high resolution spectra……………………………49

3.7 SEM images of mesoporous TiO_2 films……………………………………………..51

4.1 XRD of a NH_3(30)/NH_3 film……………………………………………………...64

4.2 High resolution XPS N 1s spectra with deconstructed fits…………………………..66

4.3 High resolution XPS Ti $2p_{1/2}$ and Ti $2p_{3/2}$ spectra with deconstructed fits…………..68

4.4 FTIR spectra of urea and urea treated TiO_2 powders………………………………..73

4.5 Photograph of films depicting the range of colors achieved…………………………75

4.6 Diffuse reflectance UV-Vis spectra of untreated and treated TiO_2 films……………78

4.7 The correlation between calculated E_g and amount of N 1s nitrogen………………..80

4.8 Correlations between calculated E_g and N*/Ti* ratios………………………………81

5.1 UV-vis absorbance spectra for the decomposition of RhB…………………………..98

5.2 Photocatalytic behavior of as received P25 at different solution temperatures……..99

5.3 SEM micrographs of as received P25 powders and P25s powders………………...101

5.4 Comparison of the photocatalytic behavior of treated TiO_2 powders……………...102

5.5 Relationship between N/Ti ratio with *d.c.* and atomic % Si with *P*………………..105

5.6 The photocatalytic behavior of TiO_2 films with SiO_2 incorporation……………….107

5.7 The photocatalytic behavior of TiO_2 films under visible light……………………..109

5.8 η_{eff}, J_{sc}, V_{oc}, and *FF* values collected from completed DSSCs……………………..110

5.9 *IPCE* curves collected as a function of wavelength from completed DSSCs………112

5.10 Voltage transient curves collected from completed DSSCs………………………113

6.1 Normalized LIF intensity of NH_2 and NH radicals as a function of P_p…………….128

6.2 OES spectra of 50 W and 300 W peak power plasmas……………………………..129

6.3 Actinometric OES data as a function of P_p ………………………………………...131

6.4 Normalized LIF intensity of NH_2 and NH radicals as a function of *d.c*..….……...132

6.5 Actinometric OES data of excited state species as a function of *d.c*..……………..134

6.6 Actinometric OES data of hydrogen atoms as a function of *d.c*…………………....135

6.7 LIF images and IRIS data for NH_2 molecules at P_p = 50 and 300 W……………...137

6.8 Scatter coefficients of NH and NH_2 as a function of P_p…………………………....142

6.9 Scatter coefficients of NH_2 and NH as a function of *d.c*…………………………...143

6.10 Possible species density profiles as a function of time……………………………148

CHAPTER 1

INTRODUCTION

This chapter introduces capabilities of plasma systems for chemists. General trends in plasma properties are given to aid in choosing initial plasma parameters emphasizing etching, surface functionalization, or deposition. Important properties of TiO_2 materials are discussed. Significant information retrieved from materials and plasma characterization methods are described. A brief overview of the chapters contained in this dissertation concludes this chapter.

1.1 Plasma Capabilities

Plasma, the fourth state of matter, is generally associated with the extreme temperatures of matter found in the sun. In contrast to these extreme temperatures found in thermal plasmas, non-thermal plasmas are more manageable and are currently used in manufacturing and laboratories around the world. A plasma consists of neutrals, electrons, radicals, and ions that collectively are quasineutral. Different types of plasmas are distinguished by the relative temperatures and densities of each of these species. For thermal plasmas, electron temperatures (T_e) are in equilibrium with the temperature of neutral (T_n) and ionic (T_i) species, whereas T_e values in non-thermal plasmas by far exceed T_n. In the experiments presented in this dissertation, low pressure non-thermal plasmas are created electrically by induction using an alternating current oscillating at a

frequency of 13.56 MHz. Alternatively, plasmas can be created electrically through capacitive coupling. Inductively-coupled plasmas have the benefit of higher electron densities when compared to capacitively-coupled plasmas when both are using the same frequency.[1] A concept important in the use of inductively-coupled plasmas is the skin effect which is caused by the efficient electromagnetic shielding capabilities of plasmas. The oscillating magnetic field that is used to sustain the plasma also induces an electric field and both have limited penetration depth (measured in Debye lengths, described below) because the plasma is an excellent electromagnetic shield, the majority of ionization occurs near the walls or “skin” of the reactor and then the excited species diffuse toward the center of the reactor.[1]

To a materials chemist, plasmas offer added versatility and more degrees of freedom in tailoring the physical and chemical properties of materials to specific applications. Plasmas can be used to activate starting materials that are normally relatively unreactive such as argon, nitrogen, or fluoroheaxanes. Plasmas produced from these systems can then be used to etch, implant chemical functionality or coat surfaces with thin films. Thus, a plasma chemist is not just limited to reactive parent molecules, but rather can exploit a wide range of starting materials to develop specific recipes to create specialized materials.

This dissertation demonstrates the three plasma treatment capabilities of etching, modifying, and depositing materials. Plasma etching can proceed via either physical or chemical mechanisms. Physical etching occurs when ions acquire enough energy to physically displace surface atoms and break bonds in the material. This is an anisotropic process wherein heavier bombarding species are more effective etchants. Chemical

etching occurs when active species are created in the plasma that react at surfaces to create often volatile products that can easily desorb from the surface. Chemical etching is typically isotropic, does not necessitate high energy ion bombardment, and is not limited to just ionic species. Plasma surface modification involves grafting species or functional groups to a surface. One example would be implantation of hydroxyl groups into a polymer surface using a water vapor plasma. Finally, plasma deposition occurs by coating a surface with a thin film. Plasma conditions used for deposition can result from mild plasma powers for polymeric monomers to high plasma powers as are employed when depositing materials from a sputter target. In any given plasma treatment, any or all of these three processes can be occurring simultaneously, and thus competitively. For this reason, the many controllable plasma processing parameters can be optimized to favor the desired processes.

In initiating a new plasma treatment, it is valuable to have a general awareness for how simple plasmas react to changes in its adjustable parameters. Chemical knowledge of particular plasma precursors used is necessary to make better estimations of plasma parameters needed for a desired treatment. When holding all variables constant in plasma systems composed of simple gases such as Ar, an increase in applied plasma power (P) will increases the density of electrons, ions, and radicals, but will also increase their kinetic temperature, and thus, their accelerating voltage across the plasma sheath, which is the term used to describe the buildup of negative charge on all plasma surfaces. This results from electrons being lighter and more mobile to the alternating electromagnetic field than other plasma species. Electrons are, therefore, the first to meet the plasma confining materials. The sheath enables the transport and acceleration of positively

charged species to substrates. The size of the plasma sheath in non-thermal plasmas is related to the Debye length (λ_D) given by Equation 1.1,

$$\lambda_D = \sqrt{\frac{\varepsilon_0 k_B T_e}{n_e e^2}} \tag{1.1}$$

where ε_0 is the permittivity of free space, k_B is the Boltzmann constant, n_e is the density of electrons, and e is the charge of an electron.[2] The Debye length is the distance required to shield an external charge and plasma sheaths can be multiple Debye lengths thick. Plasma sheaths can be increased by increasing plasma power and lowering plasma pressures to increase electron energy (T_e) and lower electron density. Plasma quasineutrality allows further lowering of electron densities by adding electronegative precursors such as O_2, SF_6, and $TiCl_4$ to the plasma. Lower pressures will also result in more energy/molecule and a higher mean free path ($\lambda_m = \frac{RT}{\pi d^2 N_A p}$) for all species with fewer collisions in the sheath. Thus, physical etching and/or film densification is likely to occur at high powers and low pressures. Deposition can be enhanced by supplying enough energy/molecule to activate monomer units without completely fragmenting them and then allowing the activated monomer enough time to react at the surface. Lower plasma duty cycles and shorter gas residence times have been found to increase monomer deposition and preserve monomer functionality.[3, 4] A plasma duty cycle (*d.c.*) is defined as the ratio of plasma on time to the total pulse cycle time. Gas residence time is the time a gas stays in a system, and can be controlled by throttling the systems pumping speed. Substrate cooling can help condense monomer units and preserve monomer functionality.[5] The parameters and trends noted here help in fine tuning plasma conditions, but the foremost controllable plasma parameter that will result in a desired treatment is the choice of chemical precursor.

1.2 Interesting Properties of TiO_2

The primary material of interest in this dissertation is TiO_2. TiO_2 along with other wide-bandgap metal oxides like ZnO have aroused significant scientific interest because of their low cost, general robustness, and applicability to a wide range of commercial products.[6] A major commercial application of these white, wide-bandgap metal oxides has been in white pigments and in sunscreens.[7] In 1972, more interest in TiO_2 was sparked by Honda and Fujishima who published their work on TiO_2 in the photolysis of water.[8] Subsequently, the Grätzel cell, which employs TiO_2 as a wide bandgap acceptor, was introduced in 1991.[9] Today, TiO_2 is used less in sunscreens unless the powders are modified because of the free radicals created on its surface when exposed to sunlight.[10, 11] Although it is still used in pigments, its use in photocatalysis as self-cleaning and antifogging coatings on a variety of surfaces is seeing much more widespread use. One example of this has been marketed by Oxititan, and it is found in a component of commercialized photovoltaics such as those found in G24i's product line of backpacks, wireless keyboards, etc. Much has been written on the photocatalytic[12] and photovoltaic[13] uses of TiO_2; here, a brief explanation is given of the concepts that are important to the photocatalytic and photovoltaic devices that were created in this dissertation to gain insight into the material treatments.

TiO_2 is capable of absorbing UV light (< 400 nm) and creating electron hole pairs that can be used to oxidize and/or reduce surface absorbed species without the use of cocatalysts.[6] Due to the amphoteric nature of TiO_2, it absorbs both polar and nonpolar moieties.[14] Both water and oxygen readily absorb to the TiO_2 surface; therefore, the actual decomposition reactions generally take place through the reduction of water to

form hydroxyl radicals and the oxidation of oxygen to form superoxides that can continue to react with water to form more hydroxyl radicals. TiO_2-based materials are labeled as sterilizing, deodorizing, purifying, and self-cleaning materials because of these photocatalytic and hydrophilic properties.

TiO_2 is used in photovoltaics to accept electrons from attached photosensitizing materials. A dye sensitized solar cell (DSSC) is composed of a light absorber, typically ruthenium-based, a wide bandgap oxide (TiO_2), conductive electrodes (F doped SnO_2 and platinum coated), and an electrolyte (I^-/I_3^-). DSSCs perform with the highest efficiencies when TiO_2 is used as the wide bandgap electron acceptor.[15, 16] The TiO_2 quickly accepts electrons to disassociate excitons created in the dye. The surface of TiO_2 is known to have trap states that increase the transport time of electrons through the mesoporous network to the back contact.[17] Plasma surface treatments address problems related to the surface states of TiO_2. Reducing or increasing trap states on the TiO_2, helps elucidate fundamental information about the material and its electron transporting mechanism. Electrons may move by a hopping mechanism, where it “hops” from one trap to the other and these hopping rates compete with charge recombination rates to result in reduced recombination. Alternatively, too many trap states and/or deep trap states can increase recombination and slow electron transport.[17]

There have been many experiments in doping TiO_2 materials to make it more sensitive to longer wavelengths of light because of its limitations in absorbing solar radiation.[18-20] Sol-gel methods often in conjunction with hydrothermal or solvothermal methods are common ways to create doped TiO_2.[21] The sol-gel method consists of four stages: hydrolysis, polycondensation, drying and thermal decomposition. By adding a

precursor during the gelation stage, doped TiO_2 often results and cations dopants are easier to introduce through this method.[21, 22] In addition to the sol-gel method, anion doped TiO_2 can be prepared by heating in an ammonia environment,[23] sputtering, ion implantation, and by plasma modification.[24] Here we use plasmas to dope and treat TiO_2 materials.

1.3 Exploring Surfaces

This dissertation focuses on plasma treating TiO_2 materials to improve its properties for use in a range of devices and products. This is done by demonstrating possible plasma treatments of TiO_2, understanding the changes induced in the treated TiO_2, and elucidating the underlying chemical mechanisms that lead to the treatments. In characterizing treated materials, X-ray photoelectron spectroscopy (XPS) proves vital in determining chemical composition of surfaces. XPS gives both elemental composition of the top 10 nm of material and it provides information on the binding environments of those elements. XPS also allows angle resolved and sputtering depth profiling studies. From these data, the dominant plasma treatment in a given system (i.e. surface deposition, functionalization, or implantation) can be elucidated. Deposition masks the underlying surface and the composition changes dramatically with depth profiling studies. Specific binding environments help identify the functional groups on the surface and loss of specific compositions after sputtering further confirms surface functionalization. Electrical and optical properties of semiconductors can vary with the same dopant being implanted into interstitial or substitutional positions in a lattice and

XPS can be used to distinguish between the two positions.[25] An interstitial dopant is more mobile than a substitutional dopant and could more easily move to fill a vacancy.[26]

To determine if etching and film damage has occurred, a scanning electron microscope (SEM) with an energy dispersive spectrometer (EDS) reveals morphology and thickness changes before and after treatments. EDS can be used in conjunction with XPS to determine the depth of deposition or surface implantation. Other analytical techniques used in elucidating material changes in these surfaces include: contact angle goniometry to determine surface energy and functionality, UV-Vis spectroscopy to determine electronic bandgap and absorption changes, and Fourier transform infrared spectroscopy (FTIR) to confirm function groups.

Photocatalytic and photovoltaic experiments give additional information about the changes that occur in treated materials. An increase or decrease in photocatalytic or photovoltaic performance reveals changes in optical absorption, surface charge, trap states, charge transport, and/or morphology of the material. Combining all these tools, will lead to increased knowledge of TiO_2, of plasma processing TiO_2 and other metal oxides and will ultimately improve devices using wide bandgap oxides.

1.4 Evaluating Plasma Systems

Plasmas are complex systems that do not always follow preconceived trends; therefore diagnostic instrumentation is needed to understand how applied parameters are affecting the plasma. Due to the many different plasma configurations used, it can be difficult to repeat a plasma experiment in reactors of different configurations unless characteristic information is given about the plasmas. Langmuir probes are often used to

determine important plasma characteristics such as electron density (N_e), ion density (N_i), plasma potential (V_p), and the floating potential (V_f). Langmuir probes are by nature intrusive and slightly alter the plasma. Alternatively, optical measurements can be used to determine some plasma characteristics. Optical emission spectroscopy (OES) collects light emitted from excited state species in the plasma. OES is used to describe trends of excited-state species densities in conjunction with an actinometer, which acts as something of an internal standard. With additional information of each species' excitation cross-section, absolute densities can be determined. The actinometric equation is:

$$\frac{I_x}{I_{act}} = \frac{\Gamma_x k_x n_e[X]}{\Gamma_{act} k_{act} n_e[act]} \tag{1.2}$$

where I is the intensity of emission, Γ is the branching ratio for emission relative to all other de-excitation paths, and k is the excitation efficiency (including the excitation cross-section) for the species of interest (x) and for the actinometer (act).[27] Further information can be determined by the relative intensities of different emission lines (transitions) in OES such as vibrational temperatures and electron temperatures.[28] Laser induced fluorescence (LIF) analyzes specific ground state plasma species to reveal tends in species densities. Vibrational and rotational temperatures can be determined from LIF excitation spectra. Additional information to help decipher plasma-surface reactions can be collected using our imaging of radicals interacting with surfaces (IRIS) technique which utilizes LIF (see Chapter 6) and provides *in situ* information on how species interact during plasma processing of a surface.

1.5 Overview of Research

This dissertation examines the following: 1) various plasma treatments and post-treatment material properties of TiO_2; 2) performance of the treated materials in photodevices; and 3) important gas and surface reactions in NH_3 plasmas. This research was initiated by undertaking the task of repeating a literature study of O_2 plasma modification of TiO_2 and expanding to additional modification systems. Chapter 3 discusses how this led to new information that demonstrated XPS assignments made in the literature were wrong. Chapter 3 compares continuous wave (CW) and pulsed plasma treatments of porous and compact TiO_2 films are compared, thereby reiterating the benefits of pulsed plasmas. Chapter 3 also demonstrates how plasmas can modify porous networks. Parametric control of pulsed plasmas is obtained by varying *d.c.* Langmuir probe measurements characterize the plasma and confirm plasma sputtering.

Chapter 4 explores nitrogen implantation into porous TiO_2 films. In performing the plasma treatments, post plasma treatment cooling resulted in the nitrogen occupying two different nitrogen binding environments, revealed by XPS. Further experimentation showed five separate nitrogen XPS binding environments could be created by selecting plasma processing conditions, precursors, and post-process annealing times. Four of the five N 1s peaks are assigned. After nitrogen plasma treatments, the initially white films ranged in color from dark black, to army green, to brown, to gold, to yellow, and to grey. Tauc bandgaps were calculated for the films and correlations were made between these values and XPS data to determine possible optical mechanisms for the resulting film colors.

Chapter 5 describes unfinished work examining the change in photodevices that results from many of the same plasma treatments discussed in Chapters 3 and 4, except the porous films are made of P25 and Solaronix films for photocatalytic and photovoltaic devices, respectively. Hypotheses are given that explain the photocatalytic and photovoltaic performance of the different treated materials. The some plasma treatments introduce recombination centers that limit the photocatalytic activity of the powders. Two different ways of plasma depositing silica into the P25 powders is explored along with a combination of nitrogen doped P25 powders that are additionally plasma coated with silica. The photovoltaic studies examine the effects of different nitrogen binding environments on the characteristic DSSC observables.

Chapter 6 investigates the molecular-level chemistry of NH_3 plasmas applied to create nitrogen-doped TiO_2 films. IRIS and OES data are used to determine important gas-phase reactions involving NH_2 and NH radicals. A novel steady-state technique is used to probe short pulsed plasmas and demonstrate short time-scale transient density profiles. Some species densities are higher and some are lower at short plasma-on times. Other species densities are lower at short plasma-off times. NH_2 and NH reactions with TiO_2 surfaces are significantly correlated to several gas-phase species in NH_3 plasmas. Variations in NH_2 and NH scatter are also discussed as a function of NH_3 plasma ion content which is varied by changing plasma *d.c.* and using a grounded mesh to remove the majority of ions from the plasma molecular beam. This chapter demonstrates the importance of various surface reactions deduced from correlating NH_2 and NH scatter coefficients with trends in densities of reactive gases and trends in plasma ion content. Finally, Chapter 7 provides insights into the many possible future directions for this

research, specifically in terms of exploring new materials, improving devices, and exploring other plasma systems.

1.6 References

1. Chabert, P.; Braithwaite, N., *Physics of Radio-Frequency Plasmas*. Cambridge University Press: Cambridge, 2011.
2. Fridman, A., *Plasma Chemistry*. Cambridge University Press: Cambridge, 2008; p 570-571.
3. Fahmy, A.; Mix, R.; Schonhals, A.; Friedrich, J., Structure of plasma-deposited copolymer films prepared from acrylic acid and styrene: Part I dependence on the duty cycle. *Plasma Processes and Polymers* **2012,** *9* (3), 273-284.
4. Kinoshita, K.; Nakano, A.; Kawahara, J.; Kunimi, N.; Hayashi, Y.; Kiso, O.; Saito, N.; Nakamura, K.; Kikkawa, T., Vapor phase reactions in polymerization plasma for divinyisiloxane-bis-benzocyclobutene film deposition. *Journal of Vacuum Science & Technology A* **2006,** *24* (6), 2192-2198.
5. Lopez, G. P.; Chilkoti, A.; Briggs, D.; Ratner, B. D., Substrate-temperature effects on film chemistry in plasma deposition of organics .3. Analysis by static secondary ion mass-spectrometry. *J. Polym. Sci. Pol. Chem.* **1992,** *30* (11), 2427-2441.
6. Zhang, H. J.; Chen, G. H.; Bahnemann, D. W., Photoelectrocatalytic materials for environmental applications. *Journal of Materials Chemistry* **2009,** *19* (29), 5089-5121.
7. Lewicka, Z. A.; Benedetto, A. F.; Benoit, D. N.; Yu, W. W.; Fortner, J. D.; Colvin, V. L., The structure, composition, and dimensions of TiO_2 and ZnO nanomaterials in commercial sunscreens. *Journal of Nanoparticle Research* **2011,** *13* (9), 3607-3617.
8. Fujishima, A.; Honda, K., Electrochemical photolysis of water at a semiconductor electrode. *Nature* **1972,** *238* (5358), 37-+.
9. O'Regan, B.; Gratzel, M., A low-cost, high-efficiency solar cell based on dye-sensitized colloidal TiO_2 films. *Nature* **1991,** *353* (6346), 737-740.
10. Serpone, N.; Dondi, D.; Albini, A., Inorganic and organic UV filters: Their role and efficacy in sunscreens and suncare product. *Inorganica Chimica Acta* **2007,** *360* (3), 794-802.
11. Virkutyte, J.; Al-Abed, S. R.; Dionysiou, D. D., Depletion of the protective aluminum hydroxide coating in TiO_2-based sunscreens by swimming pool water ingredients. *Chemical Engineering Journal* **2012,** *191*, 95-103.
12. Thompson, T. L. Photocatalysis on Titanium Dioxide Surfaces. Dissertation, University of Pittsburgh, Pittsburgh, 2006.
13. Liu, B. Titanium dioxide nanostructures for photovoltaics and photocatalysis. University of Minnesota, Minneapolis, 2011.
14. Masao Kaneko, I. O., *Photocatalysis: science and technology*. Springer: 2002; p 114-118.
15. Chiba, Y.; Islam, A.; Watanabe, Y.; Komiya, R.; Koide, N.; Han, L. Y., Dye-sensitized solar cells with conversion efficiency of 11.1%. *Japanese Journal of Applied Physics Part 2-Letters & Express Letters* **2006,** *45* (24-28), L638-L640.
16. Jayaweera, P. V. V.; Perera, A. G. U.; Tennakone, K., Why Gratzel's cell works so well. *Inorganica Chimica Acta* **2008,** *361* (3), 707-711.

17. Hao, E. C.; Anderson, N. A.; Asbury, J. B.; Lian, T. Q., Effect of trap states on interfacial electron transfer between molecular absorbates and semiconductor nanoparticles. *Journal of Physical Chemistry B* **2002,** *106* (39), 10191-10198.
18. Teh, C. M.; Mohamed, A. R., Roles of titanium dioxide and ion-doped titanium dioxide on photocatalytic degradation of organic pollutants (phenolic compounds and dyes) in aqueous solutions: A review. *Journal of Alloys and Compounds* **2011,** *509* (5), 1648-1660.
19. Liu, G.; Wang, L. Z.; Yang, H. G.; Cheng, H. M.; Lu, G. Q., Titania-based photocatalysts-crystal growth, doping and heterostructuring. *Journal of Materials Chemistry* **2010,** *20* (5), 831-843.
20. Henderson, M. A., A surface science perspective on TiO_2 photocatalysis. *Surface Science Reports* **2011,** *66* (6-7), 185-297.
21. Gupta, S. M.; Tripathi, M., A review on the synthesis of TiO_2 nanoparticles by solution route. *Central European Journal of Chemistry* **2012,** *10* (2), 279-294.
22. Cheng, P.; Deng, C. S.; Gu, M. Y.; Dai, X. M., Effect of urea on the photoactivity of titania powder prepared by sol-gel method. *Materials Chemistry and Physics* **2008,** *107* (1), 77-81.
23. Asahi, R.; Morikawa, T.; Ohwaki, T.; Aoki, K.; Taga, Y., Visible-light photocatalysis in nitrogen-doped titanium oxides. *Science* **2001,** *293* (5528), 269-271.
24. Fujishima, A.; Zhang, X.; Tryk, D. A., TiO_2 photocatalysis and related surface phenomena. *Surface Science Reports* **2008,** *63* (12), 515-582.
25. Peng, F.; Cai, L. F.; Yu, H.; Wang, H. J.; Yang, J., Synthesis and characterization of substitutional and interstitial nitrogen-doped titanium dioxides with visible light photocatalytic activity. *Journal of Solid State Chemistry* **2008,** *181* (1), 130-136.
26. Pierret, R. F., *Semiconductor Device Fundamentals*. Addison-Wesley: 1996.
27. Labelle, C. B.; Gleason, K. K., Pulsed plasma deposition from 1,1,2,2-tetrafluoroethane by electron cyclotron resonance and conventional plasma enhanced chemical vapor deposition. *Journal of Applied Polymer Science* **2001,** *80* (11), 2084-2092.
28. Cuddy, M. F. Contributions of gas-phase plasma chemistry to surface modifications and gas-surface interactions: investigations of fluorocarbon rf plasmas, Colorado State University Dissertation, Fort Collins, 2012.

CHAPTER 2

EXPERIMENTAL METHODS

This chapter illustrates the standard equipment, materials, and instrumentation used for the work presented in this dissertation. Section 2.1 outlines the apparatus, precursors, and plasma conditions used to treat the samples. Sections 2.2-2.4 review how to make and characterize treated films including the indirect characterization of the materials used in photocatalytic and photovoltaic experiments. Finally, Section 2.5 describes the IRIS setup along with the LIF and OES techniques used for optical diagnosis of the plasmas.

2.1 Plasma Processing

A tubular, glass inductively coupled rf plasma reactor,[1] shown schematically in Figure 2.1, was used to modify mesoporous and compact TiO_2 films. A few modifications specific to experiments performed in this work are briefly described here. Cylindrical glass and ceramic sleeves were used to ease cleaning of the reactor and to minimize effects of ion bombardment on the walls of the reactor. For the O_2 sputtering experiments in Chapter 3, an alumina ceramic substrate holder held the samples in a position essentially perpendicular to the gas flow; otherwise the substrates were placed parallel to the gas flow. Substrates were positioned in the middle of the plasma coil unless otherwise specified and were treated for either 2 or 30 min, Figure 2.1.

An rf power generator (Advanced Energy, RF55) delivered 13.56 MHz of continuous or pulsed power to an 8.25 turn nickel plated copper coil through a matching network consisting of a variable capacitor. Applied rf power (*P*) ranged from 75 to 220 W for CW plasmas, giving a plasma density of 0.083 to 0.24 W/cm^3, assuming that the plasma fills the volume of the reactor. With pulsed plasmas, *d.c.* is defined as the ratio of plasma on time to the total pulse cycle time and the equivalent CW power (P_{eq}) is the product of the *d.c.* and the peak applied rf power (P_p). Here, P_p was either 500 W or 315 W for pulsed plasmas using *d.c.* values of 10-90% for P_p = 500 W and of 70% for P_p = 315 W. This latter condition yielded the highest plasma density of 0.56 W/cm^3. Plasma characteristics in Chapter 3 were measured by a Scientific Systems SmartPROBE (0.19 mm tip radius and 10 mm tip length) and were analyzed by Straatum's SmartSoft v6.01 software. Ion number densities (N_i) were calculated using Laframbois theory with the Bohm factor.

Base pressure in the system was 5-10 mTorr. Plasma precursors were typically admitted to the reactor through 10 or 20 sccm MKS mass flow controllers. Needle valves were used for liquid precursors. The system pressure was held constant throughout a treatment with partial pressures ranging from 30 to 200 mTorr, as measured by a 1 Torr Baratron capacitance manometer (MKS, type 127). All O_2 (General Air, > 99.5%) treatments were performed at an O_2 partial pressure of 200 ± 5 mTorr. Unless otherwise noted, ammonia (Matheson Tri-Gas, product grade), hydrogen (Airgas, product grade), and nitrogen (Airgas, UHP) flow was regulated to maintain a total reactor pressure of 60 ± 5 mTorr for processing TiO_2 films.

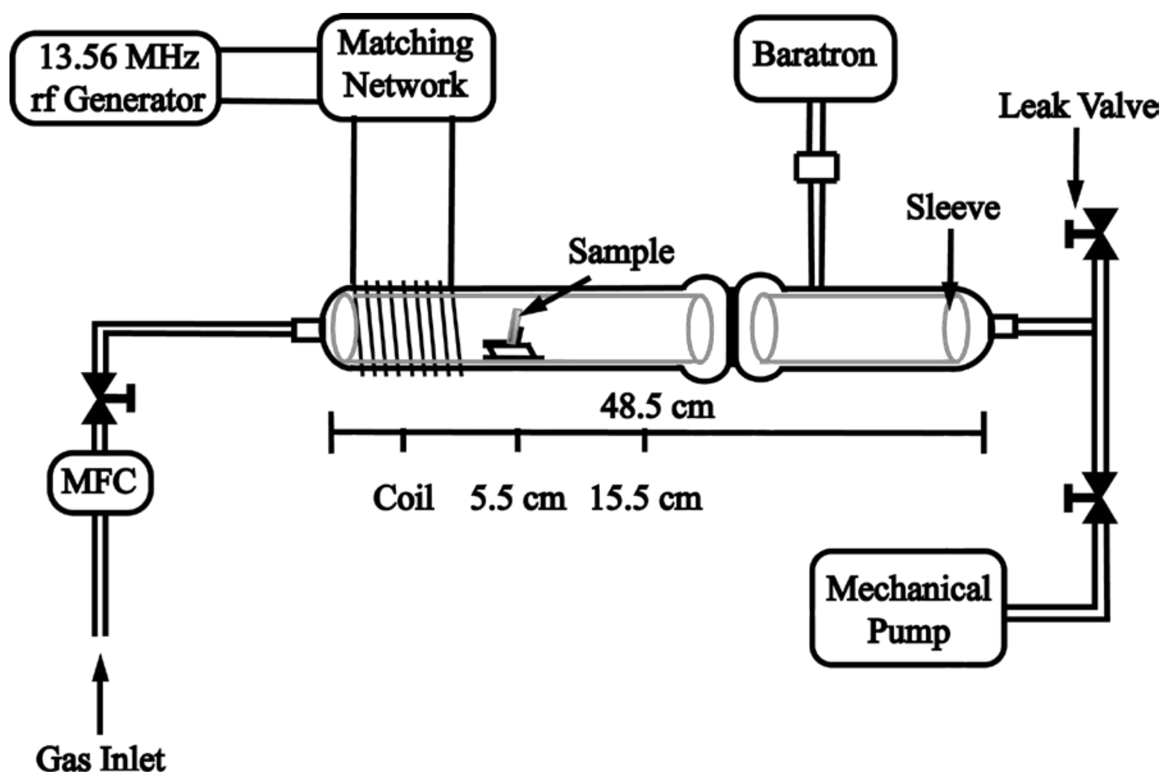

Figure 2.1. Schematic diagram of the inductively coupled plasma reaction used to modify TiO_2 films. Samples were placed at the various locations noted (in the coil, 5.5 and 14.5 cm downstream from the coil). Gas flow was controlled by a mass flow controller (MFC) or needle valves.

Hexamethyldisiloxane (HMDSO) (Aldrich, ≥ 99.5%) was used as a liquid precursor that was degassed through at least three iterations of first freezing the precursor, evacuating the gases in the flask, and then thawing the precursor. HMDSO plasmas were patterned after previous work.[2] A 10:90 mTorr mixture of HMDSO:O_2 was used to coat films with SiO_2 for a treatment time of 30 seconds and at a P = 100 W. Solid precursors were pressed into pellets of ~0.4 g with ½ inch diameters by a (Carver 4350) pellet press. Pellets of urea (Acros, ACS) were used to dope TiO_2 with nitrogen, Chapter 4, and they were positioned ~1 cm upstream from the sample. Films were cleaned prior to all nitrogen doping procedures with a 200 ± 5 mTorr pulsed oxygen (99.9% Airgas) plasma for 2 min at a 70% *d.c.* with a 30 ms on time.

2.2 Substrate Preparation

In Chapters 3 and 4, mesoporous TiO_2 films were prepared from a 5 nm anatase TiO_2 powder paste with 12 wt% titania (99.99%), 12 wt% polyethylene glycol (Fluka, 20,000 Mw), 14 wt% DI water (Millipore, 18 MΩ) and 62 wt% ethanol (AAPER, 200 proof). For photocatalytic experiments in Chapter 5 the paste consisted of 3.0 g Aeroxide P25 (Acros, as received) powder, 0.75 ml acetic acid (Mallinckrodt, ACS), 3.5 ml of DI water, 15 ml of ethanol (Pharmco, 99.5%), and 3.5 g of polyethylene glycol (Fluka, 20,000 Mw). The paste was doctor bladed onto F:SnO_2 (FTO) coated glass (Hartford Glass, TEC15 grade, 2.3 mm thick) with Scotch® tape used as a spacer for initial experiments and for creating solar cells; otherwise 1" x 1.5" (VWR) glass slides were used. Mesoporous T/SP TiO_2 substrates used in Chapter 6 were made from Solaronix paste Ti-Nanoxide T/SP that was doctor-bladed onto FTO glass substrates. The films

were allowed to dry and then calcined at 450 °C for 45 min. The term "mesoporous" is used to differentiate these films from the compact films we produced.

Note that SEM images of the films formed from 5 nm anatase powder result in materials with particle agglomerate diameters of 296 ± 125 nm and pore sizes in the range of ~40-70 nm. Thus, these materials roughly conform to the IUPAC classification of mesoporosity for materials with pore diameters of 2-50 nm.[3] These films were 5.17 ± 0.53 μm thick as measured by SEM. The mesoporous T/SP TiO_2 films were 10.1 ± 0.04 μm thick. Compact TiO_2 films used in the O_2 sputtering plasmas described in Chapter 3 were formed using a 2% (v/v) solution of titanium(IV) butoxide (Aldrich, 97%) in hexanes (Fisher, HPLC). FTO glass substrates were dipped three times in the solution, allowed to react for 15 min between immersions, and annealed at 450 °C for 45 min. These films had thicknesses of 320 ± 35 nm (measured by SEM). For IRIS experiments, glass slides were dip coated once in a 4% (v/v) solution of titanium isobutoxide diluted with hexanes and then sintered at 450 ºC for 45 min. These dense TiO_2 films contained no pores and were 162 ± 33 nm thick (measured by SEM).

Plasma treatments resulted in substrate temperatures of 210-230 °C for treatments lasting 2-30 min. These elevated temperatures, along with reactive sites created during plasma treatment, allow chemical reactions to take place even after the discharge is extinguished. Consequently, the environment in which the substrate is allowed to cool to near room temperature can affect the properties of the films. Thus, plasma-treated TiO_2 films were cooled under the flow of ammonia, hydrogen, nitrogen, and/or argon (Airgas, industrial grade) gases for at least 10 min to explore effects on film composition and optical properties. To identify the different treatments, we have developed a shorthand

notation that describes both the plasma treatment and the subsequent cooling environment, Table 2.1. For example, a TiO_2 sample treated for 2 min with an NH_3 plasma and allowed to cool under an O_2 flow is designated as NH_3/O_2. Likewise, a sample treated in the same manner, but with a 30 min plasma exposure is designated as $NH_3(30)/O_2$. The H_2,N_2/N_2 designation represents a TiO_2 film treated in series with a 2 min hydrogen plasma, then a 2 min nitrogen plasma, followed by cooling under N_2. Films designated as "annealed" consist of NH_3/NH_3 films heated under atmosphere in a furnace at 450 °C; annealing time was 30 min unless otherwise stated.

For some experiments (e.g. the O_2 plasma modification studies, Chapter 3) complete modification of the mesoporous TiO_2 network was demonstrated by dying the films overnight in methylene blue (Aldrich, > 82%). The dyed films were treated in an O_2 plasma for 30 second intervals using either (a) 220 W CW, (b) 500 W, 40% *d.c.* (30 ms on time), or (c) 275 W, 25% *d.c.* (10 ms on time). After each time interval, the films were visually checked for residual dye. Cross-sectional data from a JSM-6500F (JEOL Ltd, Japan) field emission SEM equipped with an energy dispersive spectrometer (EDS) (Thermo Fisher Scientific, Inc.) of plasma nitride mesoporous TiO_2 films also confirmed complete modification of the mesoporous network.

2.3 Substrate Characterization

Control and modified film composition was determined by XPS using a Physical Electronics PE5800 ESCA/AES system. Spectra were collected using a monochromatic Al K_α x-ray source. A low energy (~1 eV) electron neutralizer was used for charge neutralization.

Table 2.1. Notation for TiO_2 film treatments

Film Label[a]	Plasma gas[b]	Time (min)[c]	Resting gas[d]
NH_3(30)/NH_3	NH_3	30	NH_3
NH_3/NH_3	NH_3	2	NH_3
NH_3(30)/O_2	NH_3	30	O_2
NH_3/O_2	NH_3	2	O_2
H_2,N_2/N_2	H_2 then N_2	2	N_2
H_2/N_2	H_2	2	N_2
H_2/NH_3	H_2	2	NH_3
N_2/N_2	N_2	2	N_2
Annealed	--	--	Air
Urea/NH_3	Urea	2	NH_3
Untreated TiO_2	--	--	--

[a]Indicates designation used throughout text for conditions given. [b]Gas used for plasma treatment; for H_2,N_2/N_2 treatments, films were treated for 2 min in each plasma environment. [c]Time of initial plasma treatment. [d]Gas environment used post plasma treatment. Resting time for all films was at least 10 min.

Both survey scans and high resolution scans (23.5 eV pass energy with 0.100 eV/step) were acquired for the TiO_2 films. Spectra were either shifted to the Ti $2p_{3/2}$ peak at 458.6 eV in TiO_2[4-6] or to the Au $4f_{7/2}$ peak at 84.0 eV[7, 8] by using a cleaned gold O-ring attached to the surface. Curve fitting was performed using a combination of Gaussian and Lorentzian functions (10-15%) with each FWHM (full width at half maxi-mum) < 2 eV. A 2 kV 3x3 mm Ar ion beam from a Physical Electronics ion sputtering gun (11-066) was used to sputter the films. Additional compositional analyses were performed to determine the crystallinity of the treated films using X-ray diffraction (XRD) spectroscopy (Scintag X-2 with a Cu X-ray source and Peltier detector). The angle was swept from 5-90° at 0.02°/sec. The samples were analyzed in their porous form on fluorinated tin oxide (FTO) coated glass substrates.

Static water contact angles were measured under ambient laboratory conditions with a contact angle goniometer (Krüss DSA10). Reported contact angle measurements are the mean of 2-5 measurements on each of 2-3 samples for each experimental condition. The water drop profiles were fit using a tangent fitting profile. For many of the TiO_2 films, static contact angle measurements were impossible to perform as the water drop disappeared into the mesoporous network. In these instances, we were able to quantify the time it took for the water drop to disappear by acquiring a series of images in the movie mode of the DSA10. A JEOL, JSM-6500F field emission SEM was used to investigate the morphology of deposited materials and for micropattern imaging. All samples were grounded with double sided carbon tape and copper tape prior to analysis.

Diffuse reflectance spectra were collected with a Varian Cary500 UV-Vis spectrometer with a praying mantis diffuse reflectance attachment. A Teflon standard

reference was used. Absorption coefficients of the films were determined from the spectra by use of the Kubelka-Munk function, F(r).[9] Tauc plots were constructed with the assumption of an indirect, allowed bandgap material.[10] Tauc bandgap (E_g) values were acquired by plotting $(F(r)hv)^{1/2}$ vs hv and fitting a line to the linear portion of the graph in the band edge region. When E_g values were calculated, film thickness and substrate effects were not taken into account, thereby potentially introducing some error as the Kubelka-Munk function assumes a smooth and infinitely thick sample.[11]

FTIR was used to characterize the chemical environments of treated materials. For each sample, 3-6 films were treated, scraped off the substrate, and pressed into a ½ inch diameter pellet. FTIR spectra were collected using a Nicolet Magna 760 spectrometer with a 1 cm^{-1} resolution and an average of 32 scans.

2.4 Performance Characterization

The treated materials were also tested in photocatalytic experiments. After treatment and/or annealing, the P25 films were scraped off of the glass substrates and ~5 mg were used to decompose 50 ml of 4.0 mg/L RhB dye. A 1000 W mercury-xenon lamp set consistently at 814 ± 17 mW/cm2 intensity of UV and visible light illuminated the samples. Visible light experiments employed 400 nm cut off filters.

DSSCs were constructed by using mesoporous photoanode substrates were made from Solaronix Ti-Nanoxide T/SP paste. The films were coated with cis-bis(isothiocyanato) bis(2,2'-bipyridyl-4,4'-dicarboxylato) ruthenium(II) or N3 dye (donated and prepared by Mike Elliott) by allowing them to soak in saturated ethanol solutions for more than 8 hours. The electrolyte was compose of 10:1 LiI (Aldrich,

99.9%) and I_2 (Mallinckrodt, Lot 1008 KBEB) dissolved in γ- butyrolactone (Aldrich, ≥ 99%). The same cathode electrode of platinum coated glass was used for all cells. A Keithley 2400 SourceMeter operated by a Labview virtual instrument was connected to the cell in a two-electrode configuration. For current-voltage measurements, potential was swept from 700 mV to -100 mV at 50 mV s-1 as current was recorded. The cell was illuminated by a 150 W Oriel xenon arc lamp calibrated to 100 mW cm-2 ("one sun"). The light was passed through a 400 nm cutoff filter before illuminating the cell through a 0.385 cm2 orifice. The light passed through an Oriel 1/8M Cornerstone monochromator before the cutoff filter. White light emission was used for current-voltage measurements and voltage transients and the Labview virtual instrument controlled wavelength selection for collecting incident photon conversion efficiency (IPCE) measurements.

2.5 Optical Plasma Diagnostics

The IRIS apparatus is shown schematically in Figure 2.2 and it has been described previously.[12] Briefly, an inductively-coupled rf plasma is generated in a cylindrical glass reactor which is differentially pumped through an orifice where it is collimated by two rectangular slits (1.5-2.0 mm wide for NH and 2.0-3.0 mm wide for NH_2 experiments) to form an effusive molecular beam. A XeCl excimer laser is used to pump a tunable dye laser tuned to a specific rovibrational state of the molecule of interest. The laser intersects the molecular beam at a 45° angle, thereby inducing fluorescence of specific plasma species. A substrate aligned parallel to the laser beam is rotated in and out of the molecular beam to obtain surface reactivity data.

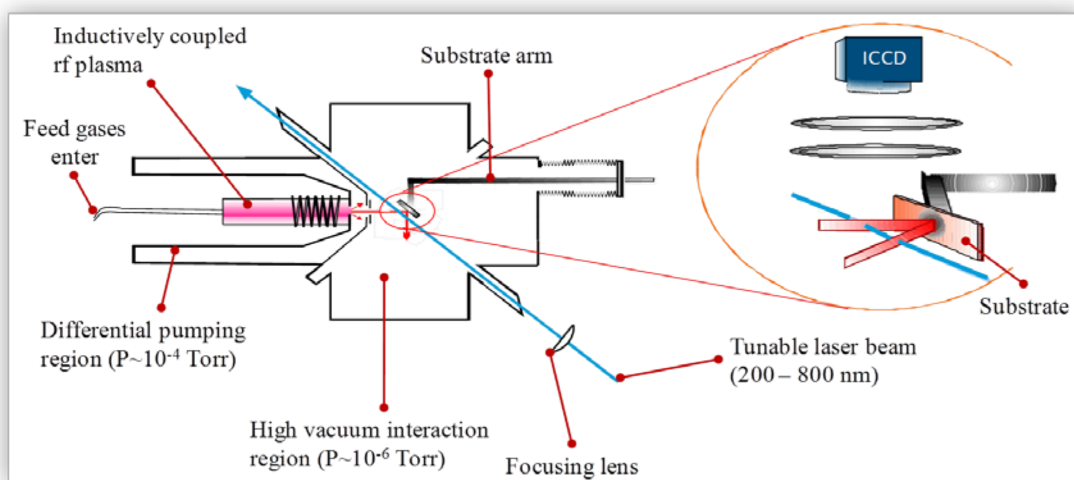

Figure 2.2. Schematic diagram of the IRIS apparatus with enlarged detail of the molecular beam interacting with a substrate.

An intensified charge coupled device (ICCD) camera is used to collect total fluorescence perpendicular to both the molecular beam and the laser. The gate delay, gate width, and gates per exposure of the ICCD can be varied to obtain information from spatially-resolved LIF images, including relative species densities and excitation spectra with and without a substrate in the path of the molecular beam.

Here, 100% NH_3 gas (Matheson Tri-Gas, product grade) was used as the source gas. The pressure (30 mTorr) was measured by a 1 Torr capacitance manometer. A 13.56 MHz rf power supply (Advanced Energy RF55) with a two capacitor matching network was used to sustain plasmas with P_p ranging from 20-400 W. The plasma power was pulsed with *d.c.* values ranging from 5-100 % by either holding t_{on} or t_{off} constant at 30 ms. For constant t_{off} conditions, a 10 % *d.c.* plasma has t_{on} = 3 ms for 30 pulses/s and a 90 % d.c. plasma has t_{on} = 270 ms, for 3.3 pulses/s. For constant t_{on} conditions, a 10 % *d.c.* plasma has 3.3 pulses/s with t_{off} = 270 ms; a 90 % *d.c.* plasma has 30 pulses/s with t_{off} = 3 ms.

The dye laser was tuned to 336.071 ± 0.002 nm for NH, and 596.722 ± 0.003 nm for NH_2. The gate delay and gate width of the ICCD camera were set at 1580-1650 ns and 500-3000 ns, respectively, regardless of the molecule under study. The laser and camera were pulsed at 350 gates per exposure and 10-30 exposures were combined to provide the resulting LIF images. LIF intensities were determined by averaging a 20 pixels wide cross-section of individual ICCD images. S values were determined from cross-sectional data, as described previously,[13, 14] by comparing to simulations of signal arising from the incident molecular beam (no substrate in the path of the molecular beam) and of LIF signal arising from molecules scattered off of the substrate surface (the

difference between images with and without a substrate in the path of the molecular beam). Briefly, the model used to determine *S* values is based on the experimental geometry, and assumes an adsorption-desorption scattering mechanism (cosine distribution about the surface normal) where the only adjustable parameter is the amount of scatter. Weighted averages of *S* values were obtained from multiple fits (i.e. $n \geq 3$) to multiple data sets (i.e. $n \geq 2$). The reported error is thus one standard deviation of the weighted average. Note that the surface scatter coefficients measured in IRIS experiments are effectively the ratio of the number of molecules under study (i.e. NH or NH_2) in the molecular beam to those being scattered off of the surface during plasma processing. As such, a scatter coefficient greater than unity ($S > 1$) signifies surface production of the species of interest, whereas $S < 1$ denotes radical consumption at the substrate surface.

A four channel AvaSpec-3648-USB2-RM spectrometer was used to determine trends in excited state species found in NH_3 plasmas by OES. Actinometry was performed by adding Ar (< 10% of total gas flow, by partial pressures) to the NH_3 gas flow. As discussed in detail previously,[15-17] actinometric OES data are effectively the ratio of the intensity of the emission peaks of the species of interest to the intensity of the Ar^* emission line at 750.3 nm. Each spectrum was integrated for 3 ms and averaged over 1000 scans. The reported error limits represent one standard deviation of 5 of these spectra taken under a given set of plasma conditions. Two different wavelengths were monitored for all species to assure signals were the result of emission from a single species and that different states displayed similar trends. The wavelengths with greater emission signals for a given species were used, Table 2.2.

Table 2.2. OES wavelengths

Species	λ(nm)	Species	λ(nm)
H_2^*	601.8	N_2^*	336.9
H_α^*	656.3	N_2^{+*}	391.2
H_β^*	486.1	NH^*	335.8
H_γ^*	434.1	NH_2^*	597.5
N^*	868.0	NHc^*	325.7
N^{+*}	648.2		

2.6 References

1. Bogart, K. H. A.; Dalleska, N. F.; Bogart, G. R.; Fisher, E. R., Plasma-enhanced chemical-vapor-deposition of SiO_2 using novel alkoxysilane precursors. *J. Vac. Sci. Technol., A* **1995,** *13* (2), 476-480.
2. Shearer, J. C.; Fisher, M. J.; Hoogeland, D.; Fisher, E. R., Composite SiO_2/TiO_2 and amine polymer/TiO_2 nanoparticles produced using plasma-enhanced chemical vapor deposition. *Applied Surface Science* **2010,** *256* (7), 2081-2091.
3. Mulder, M., *Basic Principles of Membrane Technology*. Kluwer Academic: 1996.
4. Joung, S. K.; Amemiya, T.; Murabayashi, M.; Itoh, K., Relation between photocatalytic activity and preparation conditions for nitrogen-doped visible light-driven TiO_2 photocatalysts. *Applied Catalysis A* **2006,** *312*, 20-26.
5. Nambu, A.; Graciani, J.; Rodriguez, J. A.; Wu, Q.; Fujita, E.; Sanz, J. F., N doping of TiO_2(110): Photoemission and density-functional studies. *Journal of Chemical Physics* **2006,** *125* (9).
6. Gao, B. F.; Ma, Y.; Cao, Y. A.; Zhao, J. C.; Yao, J. N., Effect of ultraviolet irradiation on crystallization behavior and surface microstructure of titania in the sol-gel process. *Journal of Solid State Chemistry* **2006,** *179* (1), 41-48.
7. McFeely, F. R.; Kowalczy.S; Ley, L.; Pollak, R. A.; Shirley, D. A., High-resolution X-ray photoemission spectra of PbS, PbSe, and PbTe valence bands. *Physical Review B* **1973,** *7* (12), 5228-5237.
8. Mangamma, G.; Ajikumar, P. K.; Nithya, R.; Sairam, T. N.; Mittal, V. K.; Kamruddin, M.; Dash, S.; Tyagi, A. K., Synthesis and gas phase nitridation of nanocrystalline TiO_2. *Journal of Physics D: Applied Physics* **2007,** *40* (15), 4597-4602.
9. Michalow, K. A.; Logvinovich, D.; Weidenkaff, A.; Amberg, M.; Fortunato, G.; Heel, A.; Graule, T.; Rekas, M., Synthesis, characterization and electronic structure of nitrogen-doped TiO_2 nanopowder. *Catal. Today* **2009,** *144* (1-2), 7-12.
10. Beranek, R.; Kisch, H., Tuning the optical and photoelectrochemical properties of surface-modified TiO_2. *Photochem. Photobiol. Sci.* **2008,** *7* (1), 40-48.
11. Murphy, A. B., Optical properties of an optically rough coating from inversion of diffuse reflectance measurements. *Appl. Opt.* **2007,** *46* (16), 3133-3143.
12. McCurdy, P. R.; Bogart, K. H. A.; Dalleska, N. F.; Fisher, E. R., A modified molecular beam instrument for the imaging of radicals interacting with surfaces during plasma processing. *Rev. Sci. Instrum.* **1997,** *68* (4), 1684-1693.
13. Butoi, C. I.; Steen, M. L.; Peers, J. R. D.; Fisher, E. R., Mechanisms and energy transfer for surface generation of NH_2 during NH_3 plasma processing of metal and polymer substrates. *J. Phys. Chem. B* **2001,** *105* (25), 5957-5967.
14. Bogart, K. H. A.; Cushing, J. P.; Fisher, E. R., Effects of plasma processing parameters on the surface reactivity of $OH(X^2\Pi)$ in tetraethoxysilane/O_2 plasmas during deposition of SiO_2. *J. Phys. Chem. B* **1997,** *101* (48), 10016-10023.
15. Labelle, C. B.; Gleason, K. K., Pulsed plasma deposition from 1,1,2,2-tetrafluoroethane by electron cyclotron resonance and conventional plasma enhanced chemical vapor deposition. *J. Appl. Polym. Sci.* **2001,** *80* (11), 2084-2092.

16. Fuller, N. C. M.; Malyshev, M. V.; Donnelly, V. M.; Herman, I. P., Characterization of transformer coupled oxygen plasmas by trace rare gases-optical emission spectroscopy and Langmuir probe analysis. *Plasma Sources Sci. Technol.* **2000,** *9* (2), 116-127.
17. Trevino, K. J.; Fisher, E. R., Detection limits and decomposition mechanisms for organic contaminants in water using optical emission spectroscopy. *Plasma Process. Polym.* **2009,** *6* (3), 180-189.

CHAPTER 3

O_2 PLASMA TREATMENT OF MESOPOROUS AND COMPACT TiO_2 PHOTOVOLTAIC FILMS: REVEALING AND ELIMINATING EFFECTS OF Si INCORPORATION

This chapter contains data from a full paper published in *Surface and Coatings Technology* and written by Daniel J. V. Pulsipher and Ellen R. Fisher. It highlights information gained from using oxygen plasmas to modify mesoporous and compact TiO_2 films. This research was initiated by undertaking the task of repeating a literature study of O_2 plasma modification of TiO_2 and expanding to additional modification systems. It explores the effects of substrate location in the plasma, and applied rf power. Beginning interest in pulsed plasmas was developed from this work.

3.1 Introduction

TiO_2 has been identified as a material with enormous potential for both photocatalytic and photovoltaic devices. In photovoltaic systems, TiO_2 has been used as a photoanode material which can be sensitized to visible radiation either by doping, dye adsorption, or semiconductor absorption.[1-4] One key limitation to the efficiency of TiO_2-based dye-sensitized solar cells (DSSCs) is the presence of surface electron trap states that limit the conductivity of the TiO_2 films. Literature data suggest these trap states are highly dependent on the surface chemistry, defect structure (i.e. bonding network), and

TiO_2 particle size.[5] In addition, these factors are all strongly dependent on preparation methods, including solvents used and sintering temperatures. Moreover, the electronic coupling of the dye with the semiconductor is intimately dependent on the TiO_2 surface chemistry, as are the kinetics of the various parasitic back electron transfer processes. Thus, a variety of surface modification techniques have been applied to TiO_2 electrodes, both before and after their synthesis in an effort to control surface trap states.

One surface modification technique that has been recently explored with TiO_2 materials is plasma surface modification. A variety of different systems have been used to alter the surface properties of TiO_2, including Ar, O_2, N_2, and air plasmas at both low (< 300 mTorr) and atmospheric pressures.[6-8] Ar plasmas have been shown to significantly decrease carbon incorporation in TiO_2 sol-gel films, thereby producing a concomitant increase in hydrophilicity.[6-8] The argon ion bombardment was also thought to increase the proportion of Ti^{3+} at the surface. Recently, N_2 plasmas were used to dope anatase TiO_2 nanoparticles with nitrogen, with some studies suggesting N_2 plasma treatment results in substantial increases in the photocurrent density (J_{sc}) as well as energy conversion efficiency.[9] N_2 plasma treatment also increases TiO_2 film hydrophilicity with contact angle values similar to those obtained with the Ar plasma.[8]

The use of O_2 plasmas for surface modification offers the potential for both decreasing surface trap states while also increasing surface hydrophilicity. This latter property is desirable for improved stability, sensitizer adsorption, and mechanical properties. Jung et al. used rf and microwave O_2 plasmas to create hydrophilic TiO_2 catalysts prepared by sol-gel methods.[10] In these studies, X-ray photoelectron spectroscopy (XPS) analysis of O_2 plasma treated films suggested that titanium was increasingly depleted in

the surface of the films as the applied power (50-200 W) was increased for both rf and microwave plasmas. High resolution spectra of the O 1s binding region displayed two binding environments for O atoms in the films, centered at 534.0 and 530 eV. These states were attributed to hydroxyl species on the surface of the film resulting from the interactions of oxygen atoms with the TiO_2, producing a nonstoichiometric material. Fourier transform infrared (FTIR) spectroscopy data also suggested the films contained OH groups. Notably, however, Jung et al. did not report atomic composition or the O/Ti ratio data from their XPS results, limiting the ability to interpret their XPS data. Jung et al. did examine surface hydrophilicity and found that contact angles for their TiO_2 films decreased from ~15° to ~5° upon O_2 plasma treatment. Similar results were obtained by Wang and coworkers,[8] who attributed this change in hydrophilicity to formation of oxygen defects on the surface. Lee and coworkers found the J_{sc} value and the efficiency of O_2 plasma treated TiO_2 films were higher than for untreated materials, which significantly improved their performance in DSSCs.[9]

In the present work, we used O_2 plasmas in an attempt to reproduce the work of Jung et al. with the goal of incorporating the modified materials into DSSCs and evaluating their photovoltaic properties relative to unmodified materials. We were also interested in more fully exploring the plasma parameter space as well as clarifying the underlying chemical modifications that were responsible for the observed surface changes reported in the literature. A primary concern with O_2 plasmas is that they are extremely efficient at etching a variety of materials, including the walls of reactors. Thus, there is often a delicate balance between achieving the desired surface modification and damaging or otherwise altering the substrate of interest. The plasma parameters explored here

include substrate position in the plasma reactor, applied rf power (*P*), and plasma mode (continuous wave (CW) or pulsed). Plasma-treated films were analyzed using XPS, contact angle measurements, and scanning electron microscopy (SEM) and were compared to untreated materials. The plasma was also characterized by Langmuir probe measurements.

3.2 Results and Discussion

As noted in Section 3.1, one of the primary goals of this research was to verify and expand upon the results found by Jung et al. for O_2 plasma modification of TiO_2 films using rf and microwave plasmas. The data of Jung et al. focused on a single plasma parameter, applied power (either rf or microwave).[10] One of the adjustable parameters we have that is not necessarily available in other reactors is relative position of the substrate in the reactor. Previous work in our laboratory[11-14] has demonstrated that the location of the substrate can significantly alter the plasma-substrate interactions in both film deposition and surface modification processes. Thus, we examined this parameter to determine if location in the reactor significantly changed the resulting film modification.

Figure 3.1 contains high resolution O 1s XPS spectra that summarize results for films placed either directly in the coil region of the plasma reactor or 5.5 cm downstream from the downstream end of the coil. The spectrum for untreated TiO_2 is also shown for comparison. Films treated further downstream (15.5 cm) have XPS spectra similar to the film treated at 5.5 cm. The two larger peaks in the spectrum represent TiO_2 lattice oxygen[15] (529.7 ± 0.2 eV) and bridging oxygen[16, 17] (530.6 ± 0.2 eV) moieties. Although these peaks are well established, the assignment of the peak at the highest binding energy,

532.3 ± 0.3 eV, has not been well characterized. Possible assignments include adsorbed oxygen or hydroxyl species,[2, 18-21] oxygen containing carbon species and/or organic contaminants.[6, 17, 20] Jung et al. specifically assigned this peak to surface hydroxyl species and used its presence to explain their observed increase in hydrophilicity upon plasma treatment. As discussed below, we do not believe this peak is attributable to hydroxyl species. Nonetheless, the data in Figure 3.1 clearly reveal that films treated in the coil region of the O_2 plasma are significantly different chemically from either the untreated films or films treated downstream from the plasma.

Evaluation of the chemical composition of the modified and unmodified films, specifically the O/Ti ratio, helps elucidate the differences between the spectra displayed in Figure 3.1. The O/Ti ratio for unmodified TiO_2 films, 2.41 ± 0.08, is greater than the stoichiometric value of 2.0. This likely arises because of the surface specificity of XPS and the tendency of oxides to terminate in oxygen and hydroxyl bonds.[22, 23] Another contributing factor to the high oxygen content is the affinity of TiO_2 for carbonyl and hydroxyl species, an important quality for photocatalysis.[3] Films placed 5.5 cm downstream from the plasma have O/Ti = 2.22 ± 0.05, suggesting the plasma may be cleaning the surface of the films. This is supported by the C/O ratio of unmodified TiO_2 films, 0.20 ± 0.06, relative to that of films modified downstream from the plasma, 0.08 ± 0.05. The remaining surface carbon is assigned to adventitious carbon. Films modified directly in the coil region have O/Ti = 8.19 ± 3.73, suggesting modification has resulted in significantly increased oxygen content in the films.

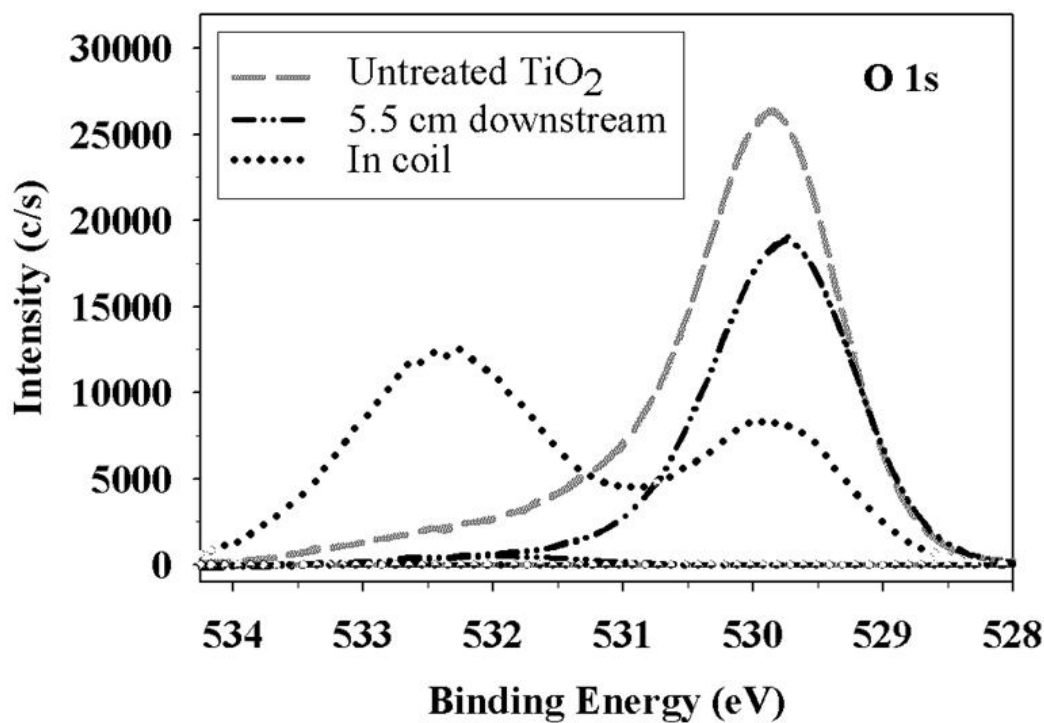

Figure 3.1. XPS O 1s high resolution spectra for untreated mesoporous TiO_2 films and for two mesoporous films that were treated for 30 min in a 220 W CW O_2 plasma at different positions in the reactor, directly in the coil and 5.5 cm downstream from the coil.

As noted above, the only parameter that Jung et al. examined was applied plasma power in both rf and microwave plasmas. Here, we varied the CW applied rf power from 75 - 220 W with substrates placed in the coil region of the plasma to further explore the surface modification process. Figure 3.2 displays high resolution XPS spectra that demonstrate the effects of *P* on the surface composition of mesoporous TiO_2 films. For the O 1s spectra, Figure 3.2a, the higher binding energy peak at 532.3 eV increases with increasing power similar to the data Jung et al. obtained using both rf and microwave O_2 plasmas to modify TiO_2 films. Likewise, the Ti 2p spectra shown in Figure 3.2b display a similar *P* dependence to that of Jung et al. These spectra demonstrate that the concentration of Ti atoms at the surface decreases with increasing *P*, as is clear from the atomic percentages listed in Table 3.1. The decrease in Ti at the surface could be the result of preferential etching of surface Ti atoms; substitution of Ti in the matrix by another atom; or deposition of a surface layer, thereby masking the Ti.

Further clarification can be achieved by examining the other elements present in the treated and untreated films, Table 3.1. For a few of our treated materials, we observe trace amounts of Sn and N. The Sn arises primarily from the underlying substrate and the nitrogen likely arises from post treatment reactions upon exposure to atmosphere. Even for the entries in Table 3.1 that contain these elements, not all samples included in those values contained Sn or N. In all cases, however, neither Sn nor N contribute significantly to the composition of the TiO_2 materials. In contrast, as can be seen from the compositional data listed in Table 3.1, depending on *P*, there are significant amounts of Si incorporated into the plasma treated films. Several sources of Si are available in our reactors, most notably the reactor itself as well as the substrates that are used for the TiO_2 films.

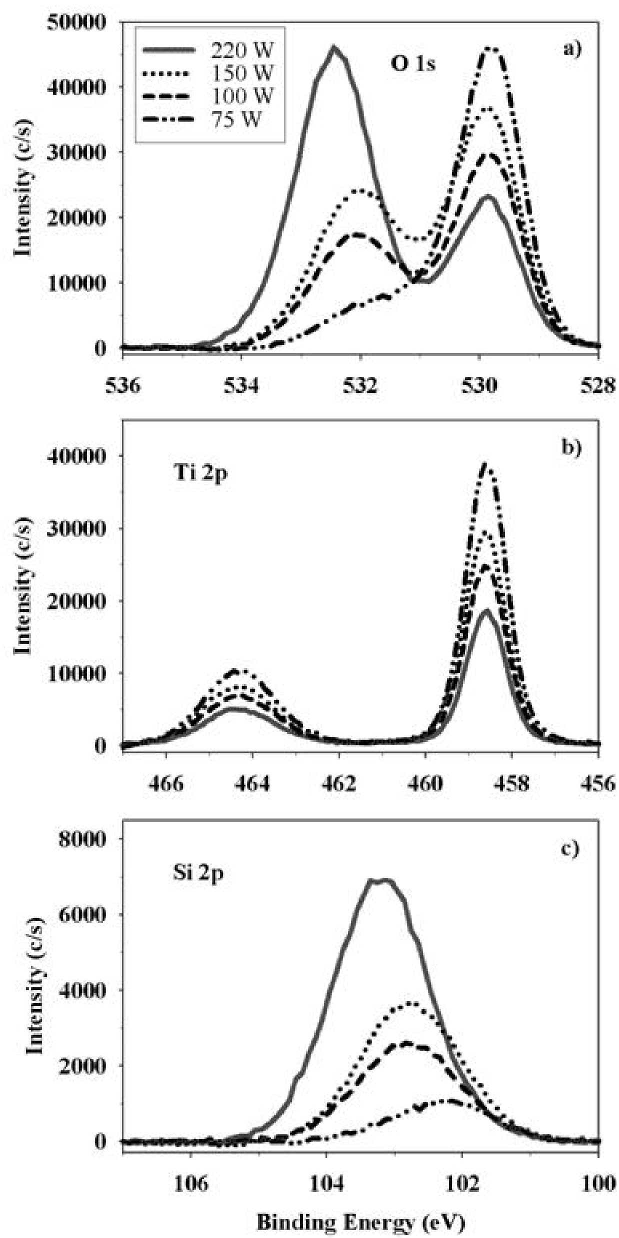

Figure 3.2. XPS high resolution spectra for mesoporous TiO_2 films treated in the coil region of CW O_2 plasmas with P = 75-220 W: (a) O 1s; (b) Ti 2p; and (c) Si 2p.

Table 3.1. XPS atomic composition for untreated and O_2 plasma-treated TiO_2 films.[a]

Power (W)[b]	% Ti	%O	%Si	%C	%Sn	%N
Mesoporous[c]	25.8 ± 0.9	62.2 ± 2.9	--	12.1 ± 3.4	--	--
Compact-heated[c]	23.5 ± 1.0	61.1 ± 1.5	3.1 ± 1.6	11.3 ± 1.3	--	--
Compact-unheated[c]	21.2 ± 4.8	55.9 ± 3.7	1.8 ± 3.0	20.0 ± 5.6	0.3 ± 0.6	0.9 ± 0.4
75	26.7 ± 0.5	67.9 ± 0.1	4.1 ± 0.8	1.3 ± 0.4	--	--
100	21.2 ± 3.2	68.9 ± 0.3	9.3 ± 3.0	0.6 ± 0.5	--	--
150	17.1 ± 0.8	68.9 ± 0.6	13.2 ± 0.8	0.8 ± 0.5	--	--
220	10.1 ± 4.9	67.2 ± 1.4	21.1 ± 5.4	1.5 ± 1.5	0.2 ± 0.3	--
5% d.c.	29.1 ± 0.9	62.7± 4.1	0.1 ± 0.2	8.1 ± 5.1	--	--
40% d.c.	31.1 ± 2.1	63.5 ± 2.2	0.7 ± 0.6	4.7 ± 2.2	--	--
70% d.c.	26.7 ± 3.0	65.5 ± 1.7	2.8 ± 2.2	4.5 ± 0.8	0.2 ± 0.4	1.0 ± 1.6

[a]All films were placed directly in the coil region of the plasma reactor.
[b]*P* listed for CW treatments; pulsed plasma treatments [indicated by % *d.c.* (*d.c.*)] were performed with P_p = 500 W.
[c]Untreated TiO_2 films.

It should be noted that we attempted to use both quartz and Al_2O_3 substrates in the plasma reactor rather than the FTO materials. In both cases, we found Si contamination in the films after treatment.

Figure 3.2c shows the high resolution Si 2p spectra for films treated at different plasma powers. As expected from the compositional data, the peak increases dramatically with *P*. It also shifts from being centered around 102 eV to the higher binding energy of ~103.5 eV, characteristic of silicon in a tetrahedral SiO_2 network.[24] The correlation of the Si 2p peak with increasing *P* suggests the loss of Ti atoms at the surface is the result of either Si atom substitution in the TiO_2 lattice or deposition of SiO_2 onto the surface of the TiO_2 films. Note the O/(Si+Ti) ratios average 2.16 ± 0.09 for the plasma treated films, implying the surface of our modified TiO_2 films has a $Ti_xSi_yO_{2x+2y}$ composition with the excess of oxygen assigned to terminating and bridging oxygen groups. Interestingly, Jung et al. did not report any elemental composition data for their materials, nor did they indicate they observed any Si incorporation as a result of plasma treatment.[10] They assigned the higher binding energy peak seen in the O 1s XPS spectra to OH surface species; thus, they credited this peak with the measured increase in surface hydrophilicity of their films as well as the increased photocatalytic performance. The improvement of photocatalysis using TiO_2-SiO_2 composites has been documented, along with an increased number of surface acid sites.[21] This is attributed to an increased oxidation potential as well as an increased number of surface hydroxyls on the mixed material,

The incorporation of Si into the TiO_2 films was explored through an angle resolved XPS (ARXPS) study, revealing only small changes in Si content throughout the top 100 nm of the films. O/Si ratios of 5.1, 5.7, and 5.8 and O/(Si+Ti) ratios of 1.9, 2.1,

and 2.3 were obtained at 0, 45, and 90° angles, respectively. This suggests silicon atoms are present throughout the TiO_2 particle mesoporous network and not just as a SiO_2 layer deposited on the outermost surface of the TiO_2 film. To demonstrate that plasma modification could penetrate the porous structure, mesoporous TiO_2 films were dyed overnight in a methylene blue solution (an organic dye which binds well to TiO_2) and then treated with an O_2 plasma at applied rf powers equivalent to or lower than those used to treat TiO_2 films. The dye was completely removed after a very short exposure to a CW O_2 plasma [< 2 min at high plasma powers (P = 220 W CW and P_p = 500 W, 40% *d.c.* (P_{eq} = 200 W)] or ~ 20 min in a pulsed plasma with P_{eq} = 69 W. This clearly indicates the plasma is capable of modifying the entire mesoporous structure. Similar results have been reported from our group in the plasma surface modification of microporous and ultrafiltration membranes.[25-27] The ability to modify the entire mesoporous structure bodes well for plasma treatments as a surface modification technique for DSSC materials.

Sputtering modified mesoporous and compact TiO_2 films with an Ar ion gun gives further insight into the composition of modified films. For these experiments, TiO_2 films were modified in the coil region of a CW plasma with P = 220 W. XPS atomic composition measurements yielded ~10% and ~5% surface Ti for the porous and compact films, respectively. The lower value for surface Ti may be a result of the smaller surface area of the film. During plasma treatment, reactive Si species are implanted in the film, resulting in a decrease in Ti atoms at the surface. If we assume a fixed number of Si atoms are available under any given set of plasma conditions, films with lower surface area will have a higher Si to surface area ratio.

Figure 3.3 shows the atomic percentages of oxygen, silicon, and titanium as a function of Ar^+ sputtering time for the two modified TiO_2 materials. We previously measured the sputtering rate for TiO_2 as ~7 Å/min [28] and the SiO_2 sputter rate is ~16 Å/min. The atomic concentration of Sn is also shown for the compact film, as these films are sufficiently thin that signal from the underlying F:SnO_2-coated glass substrate is observed as the sputtering proceeds. The interface layer for the mesoporous films is larger than that for the compact film, as evidenced by the rapid decrease in Si content. For both materials, the interface is significantly larger than the size of a single TiO_2 particle sintered to make the mesoporous films (~5 nm). The smaller interface for the compact film may be the result of the lower surface area of this material. Although signal from Si is observed for the compact films, at sputter times greater than ~100 sec, the values are extremely small and likely reflect signal from the underlying substrate. Assuming argon sputtering does not result in the silicon atoms descending further into the film, these data support the conclusion that silicon atoms are interspersed throughout the TiO_2 mesoporous films, but reside primarily at the surface of the compact film. The amount of oxygen in both sputtered materials decreases with time from O/(Ti+Si) ratios of 2.3 to 1.8 or lower because of preferential sputtering of oxygen in TiO_2 and SiO_2 structures.[29, 30]

Figure 3.4 shows the O 1s high resolution XPS spectra for mesoporous and compact TiO_2 films acquired after different sputtering times. Comparing data for mesoporous films, Figure 3.2a with Figure 3.4a, each spectrum has two peaks at ~532 eV and ~530 eV. In the sputtered films, initially the higher binding energy peak dominates the spectrum. As the films are sputtered, the 532 eV peak shifts to lower binding energy and the lower binding energy peak at ~530 eV increases in intensity at longer sputtering times.

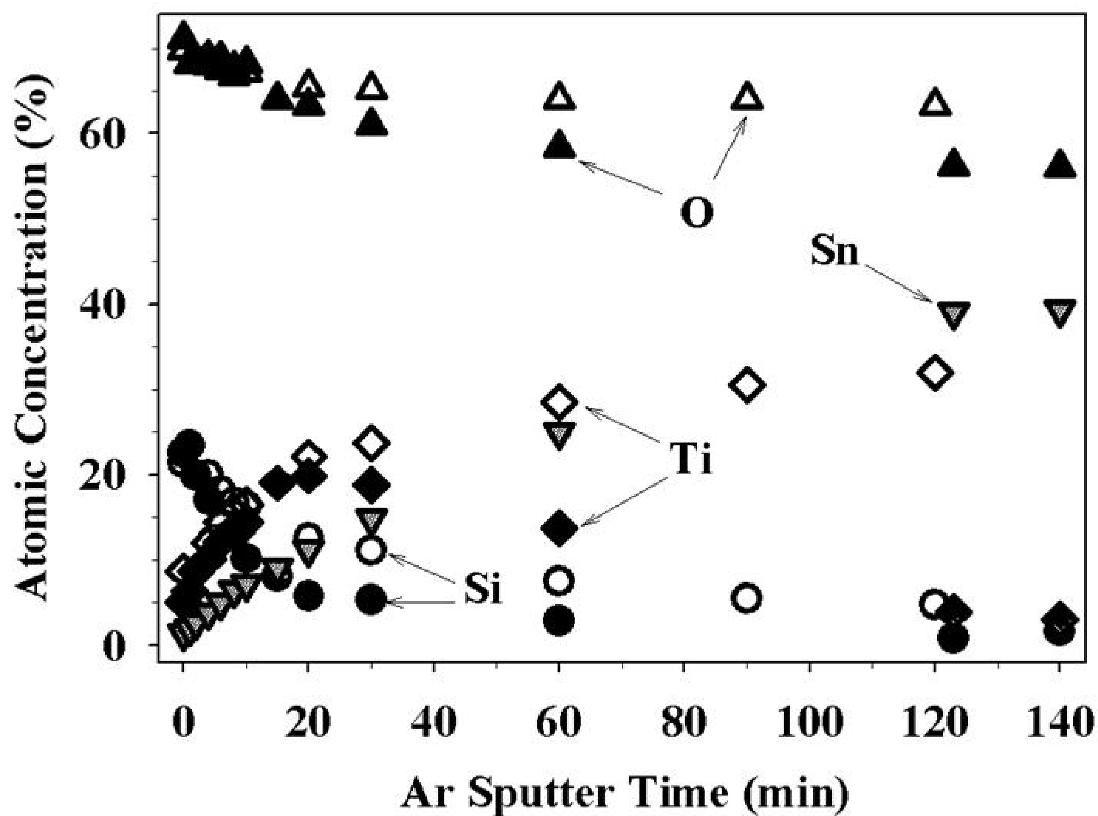

Figure 3.3. XPS atomic concentration data as a function of Ar^+ sputter time for mesoporous and dense TiO_2 films. The films were modified in the coil region of a 220 W CW O_2 plasma. Open symbols are data for mesoporous films and closed symbols are data for compact TiO_2 films.

This trend mimics the changes observed for the mesoporous films treated at different plasma powers, Figure 3.2a. The observed binding energy shift suggests the films have less SiO_2 character and more SiO_x character, where $x < 2$, as the mesoporous films are modified with lower plasma powers or the films treated with a 220 W CW plasma are sputtered for longer times. The similarities in these spectra are further evidence that lower levels of Si atoms are created at lower *P* and that penetration of the TiO_2 network occurs much more readily at higher *P*. Similar trends are observed for sputtering of compact TiO_2 films, Figure 3.4b, although the peak intensities change more dramatically and the peaks are less resolved than those for the mesoporous TiO_2 films. This could be the result of a sharper interface and a less well-defined SiO_2 environment in the compact TiO_2 films. Moreover, the thinner nature of these materials results in contributions from the F:SnO_2 substrate.

Suzer and coworkers implemented biasing of TiO_2 materials during XPS analysis to determine if SiO_2 domains existed in their films.[29] Application of ±10 V bias resulted in a positive binding energy shift in the XPS peaks with a positive bias and a negative shift with a negative bias. Although the relative positions of the peaks were unchanged, the shifting of the O 1s binding energy upon biasing indicates there are chemically distinct domains in their materials (i.e. SiO_2 and TiO_2 areas). We applied the same technique to our plasma-modified films and noted no change in the chemical environments of the sputtered compact and mesoporous TiO_2 films when a positive or negative 10 V bias is applied during XPS measurements. This suggests no distinct, chemically different domains exist in our films, further evidence of Si penetration and incorporation throughout the TiO_2 network.

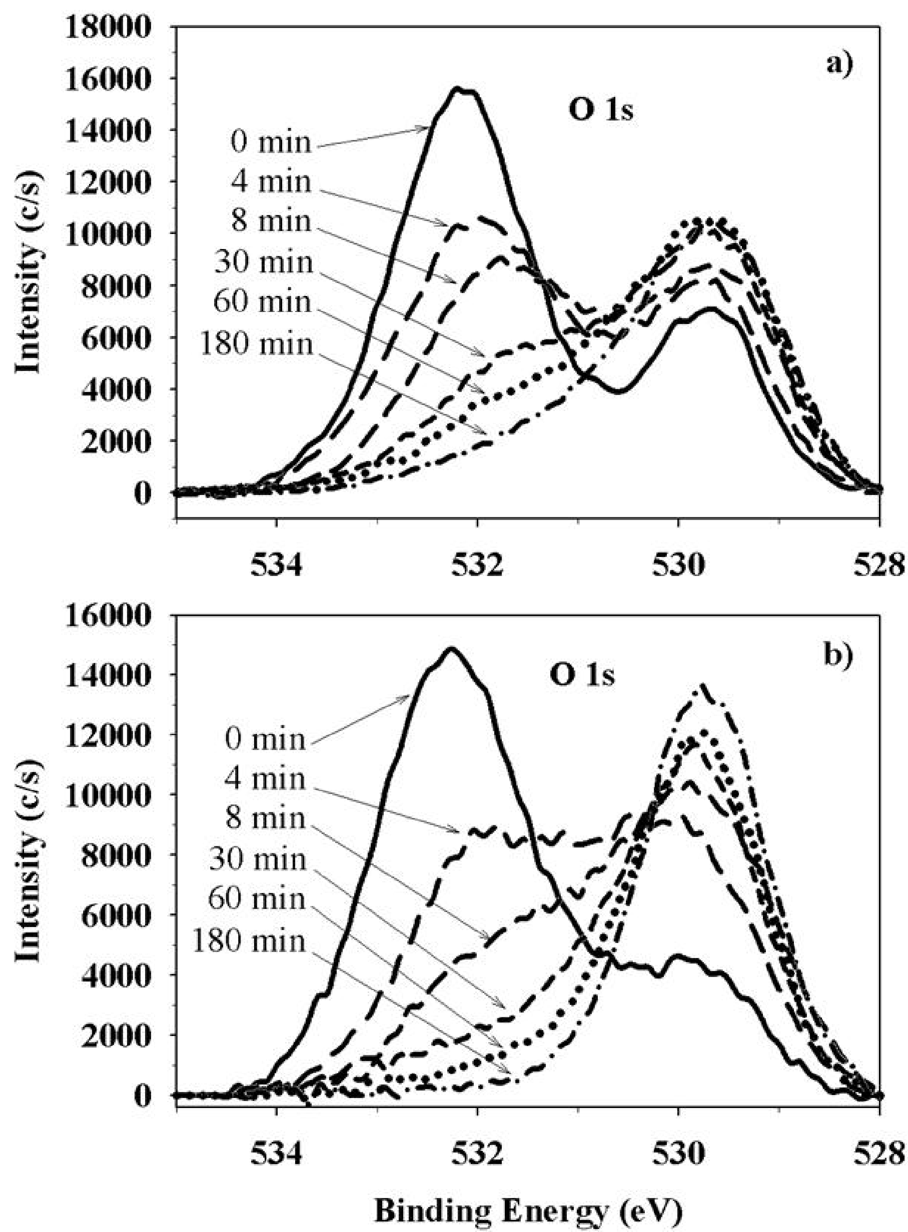

Figure 3.4. O 1s XPS high resolution spectra acquired during sputtering experiments with (a) mesoporous and (b) compact TiO_2 films modified in the coil region of a 220 W CW O_2 plasma.

All of our mesoporous TiO_2 films were hydrophilic; water drops placed on the surface disappeared instantaneously. In contrast, contact angles for compact TiO_2 films were dependent on film preparation conditions. Unsintered and sintered films yielded values of $48.9 \pm 3.6°$ and $4.5 \pm 2.3°$ respectively. The contact angle of the sintered film, however, increased significantly to $20.8 \pm 2.0°$ upon aging under ambient conditions for 2 days. The higher contact angle for unsintered compact films likely reflects the high carbon content of unsintered films arising from residual hexanes from the starting materials, Table 3.1. Wang and coworkers found a similar decrease in contact angle with heat treatment of their TiO_2 films formed via rf sputtering.[8] After films were plasma treated in a 220 W CW plasma, the water drop disappeared in < 1 second on the sintered film and in < 2 seconds on the unsintered film, as measured in movie mode of the contact angle goniometer. These results were reproducible even after 3 days under ambient laboratory conditions. Machida et al. examined contact angle as a function of silicon content in a TiO_2-SiO_2 composite system, and found a dramatic drop in contact angle for 10-30 mol% SiO_2.[31] Thus, the changes we observe in contact angles for treated films likely reflect the increased Si content and concomitant increased concentration of surface hydroxyls.

Figure 3.5 contains characteristic plasma parameters measured with a Langmuir probe as a function of applied rf power in the O_2 plasma. As expected, both the ion density (N_i) and the electron density (N_e) increase monotonically with P, Figure 3.5a, with N_i ~$2N_e$ at all powers. The difference in N_i and N_e is likely accounted for by negative ion density or possibly induced secondary electron emission.[32, 33] Unfortunately, negative ions are not normally accounted for in Langmuir probe measurements.[34, 35]

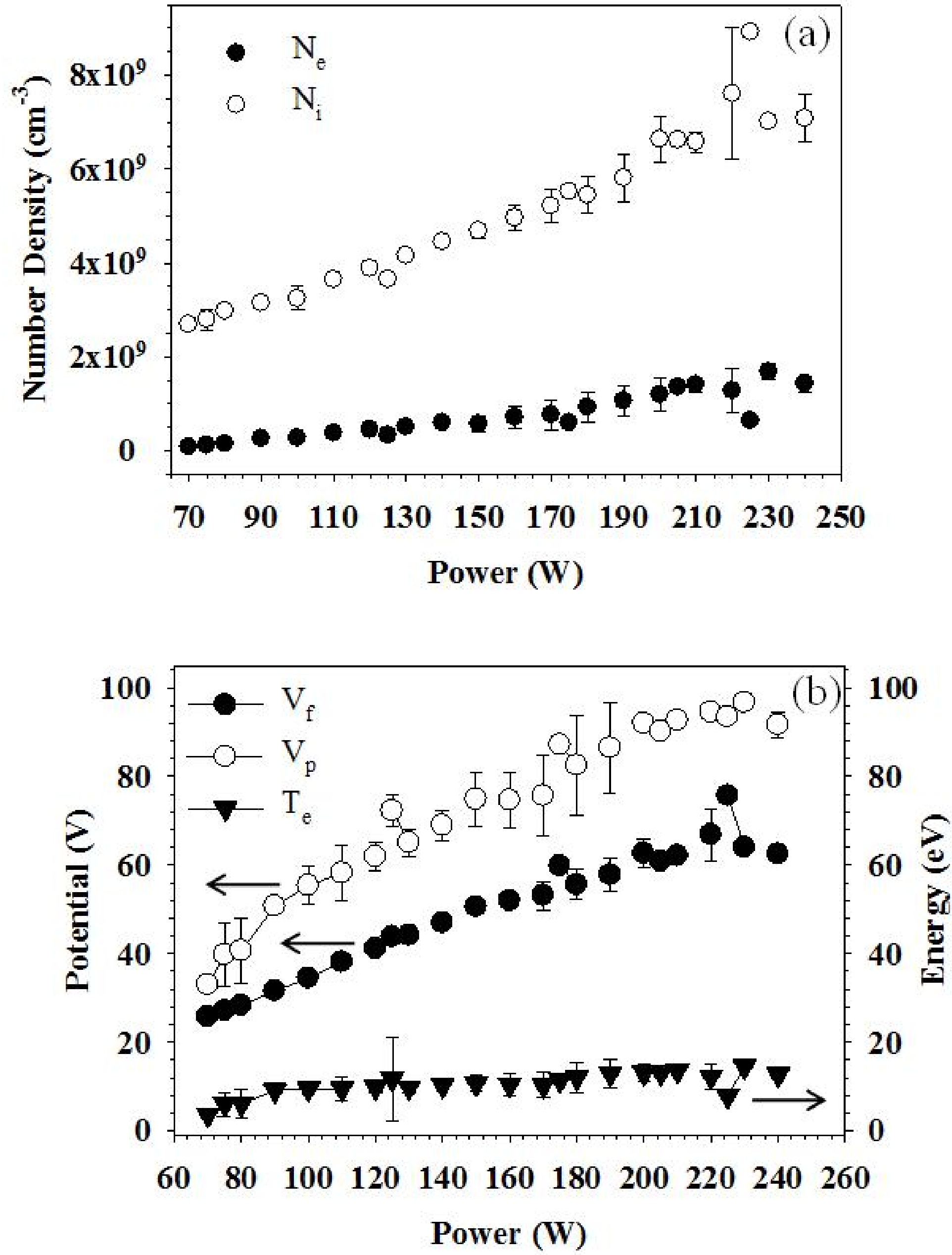

Figure 3.5. Langmuir probe data as a function of applied rf power: (a) ion density (N_i) and electron density (N_e); and (b) plasma potential (V_p), floating potential (V_f) and electron temperature (T_e).

The increase in silicon incorporation in our TiO_2 films can be understood from both the increase in N_i, Figure 3.5a, and the increase in plasma potential (V_p), Figure 3.5b. At the higher P, more ions are bombarding the walls of the reactor, resulting in increased sputtering. The potential through which positive ions will be accelerated is related to the difference between V_p and the floating potential (V_f)[33]. As our data in Figure 3.5b demonstrate, the 75 W and 220 W oxygen plasmas have positive ion accelerating potentials of ~13 and ~28 V, respectively. The physical sputtering threshold of SiO_2 in O_2 plasmas has been measured as ~25 V and model calculations confirm this result.[36, 37] Thus, our data are consistent with this value and suggest the ions in our high P plasmas have sufficient energy to sputter the reactor walls.

Although the presence of SiO_x in our TiO_2 materials may serve to improve the photocatalytic behavior of these films, one goal of our studies is to control the surface modification process. Thus, we explored several schemes for eliminating the implanted silicon. We attempted to limit the interaction of the plasma with glass surfaces using ceramic substrates and sleeves in the reactor. Although the amount of silicon incorporated decreased somewhat, this did not eliminate the inclusion of Si in the TiO_2 films. Alternatively, pulsed plasmas were utilized to reduce substrate temperatures, eliminate film damage resulting from ion and UV bombardment, lower the concentrations of trapped radicals in the treated materials, and increase plasma process uniformity.[12, 38, 39] Figure 3.6 displays the Si/O XPS ratios of the treated films as a function of the plasma *d.c.*. It is interesting to consider P_{eq} of the systems used in these experiments, as a 40% *d.c.* yields P_{eq} = 200 W, similar to P used for our CW treatments, 220 W.

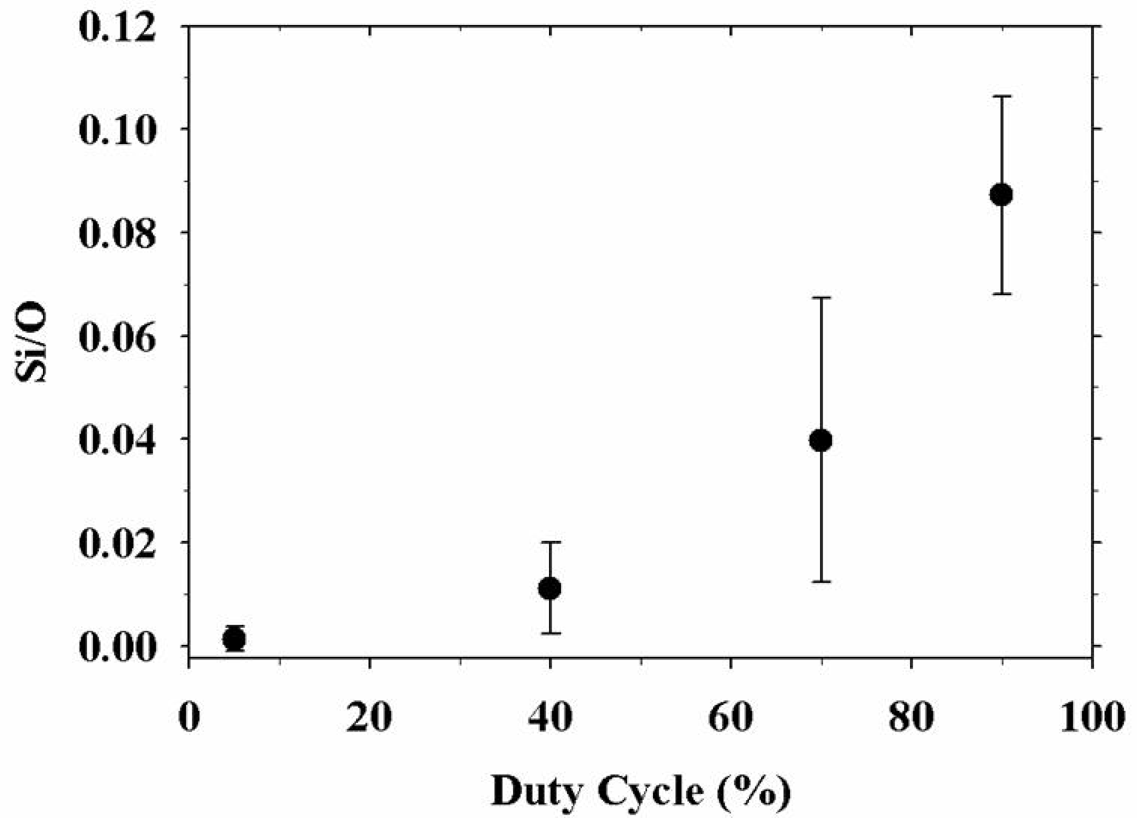

Figure 3.6. Si/O ratio as determined by XPS high resolution spectra for films modified in pulsed O_2 plasmas as a function of the plasma *d.c.*. Error bars represent one standard deviation of the mean for 9-12 measurements.

Under these conditions, the amount of silicon incorporated into the films is in the noise of the HRES Si 2p XPS spectra (0.7 ± 0.6%). A similar result is found at the lowest *d.c.* employed (5%), Table 3.1. Notably, at a 70% *d.c.* (P_{eq} = 350 W), the Si atomic concentration in the film is 2.8 ± 2.2%, within experimental error of the values found at the lowest CW power. The highest silicon incorporation measured using a pulsed O_2 plasma was 5.5 ± 1.1% (90% *d.c.* true). At P_{eq} = 450 W, the FTO coated glass substrates began to melt, and the substrates deformed; yet there was still very little silicon incorporation into the films from the walls of the glass reactor. Note that at 90% *d.c.* (P_p = 500 W), the temperature of the reactor walls reached 225 °C, conditions that would be likely to yield significant Si atoms.

In addition to chemical modification as a result of plasma exposure, physical modification (e.g. roughening or etching) can also occur during treatment. Figure 3.7 shows SEM images of untreated mesoporous TiO_2 films along with films treated in a 200 W CW plasma, and in 500 W pulsed plasmas using two different *d.c.* values, 5% and 70% (P_{eq} = 25 W and 350 W, respectively). Figure 3.7a shows the untreated TiO_2, revealing the films have a rough surface comprising globular particles with a diameter of 296 ± 125 nm. Interestingly, after treatment in the 220 W CW plasma, Figure 3.7b, the film morphology has not changed significantly, although it may be slightly rougher than the untreated film. Likewise, the morphology of the film treated with a 5% *d.c.* O_2 plasma (P_{eq} = 25 W), Figure 3.7c, does not appear to have been altered from the untreated film. After 30 minutes in the 70% *d.c.* (P_{eq} = 350 W) plasma, however, the surface of the film has changed somewhat, Figure 3.7d, with a small decrease in particle size.

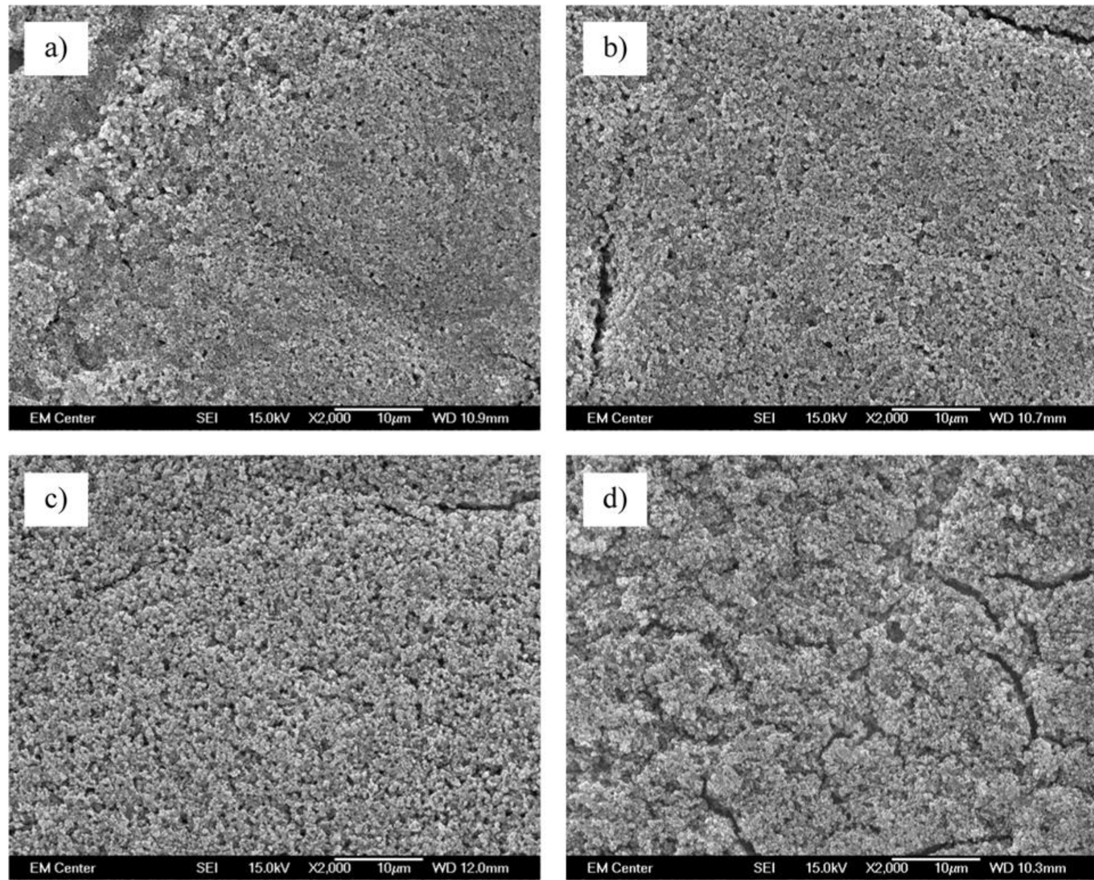

Figure 3.7. SEM images of mesoporous TiO_2 films: (a) untreated; (b) treated in a 220 W CW plasma; (c) treated in a 5% *d.c.* (P_{eq} = 25 W) plasma; and (d) treated in a 70% *d.c.* (P_{eq} = 350 W) plasma.

This suggests that an equivalent CW power of 350 W is sufficient to damage the TiO_2 film surface, despite the pulsed nature of the plasma. Interestingly, Jung et al. found that treatment in their reactors with even P = 50 W plasmas was capable of decreasing the grain size of their sol-gel formed TiO_2 films from ~40 nm to ~10 nm. Extended plasma treatments at high P (typically 200 W) resulted in smooth surfaces. These differences in morphology changes upon plasma treatment most likely reflect differences arising in the films as a result of the method of film formation and curing procedures, as well as the differences in the plasma configuration used for treatment.

3.3 Summary

An inductively coupled rf oxygen plasma was used to treat compact and mesoporous TiO_2 films. For the mesoporous films, the O_2 plasma results in significant incorporation of Si into the entire TiO_2 network, with more Si being incorporated into films placed directly in the coil region of the plasma, than in those placed downstream from the coil. XPS analysis reveals that the high binding energy peak observed in the O 1s XPS high resolution spectrum is attributable to the SiO_x formed in the process, and not to OH species being incorporated into the TiO_2 film as was previously reported by Jung et al. Changes in static contact angles measured on treated TiO_2 films can also be attributed to inclusion of SiO_x in the TiO_2 network. Notably, our data demonstrate that Si incorporation can be eliminated using pulsed O_2 plasma treatments even at high plasma powers. Further experiments employing both compact and porous titania films prepared from the same precursor such as titanium butoxide are underway to elucidate potential film differences resulting from different preparation methods and precursors. Furthermore, use of

low *d.c.* pulsed plasmas reduces damage caused by high plasma powers. Additional studies on the electrical properties of these materials as photoanodes in dye-sensitized solar cells are currently being explored in our laboratories along with alternate plasma surface modification chemistries.

3.4 References

1. Gan, W. Y.; Chiang, K.; Brungs, M.; Amal, R., Dense TiO_2 thin film: photoelectrochemical and photocatalytic properties. *Int. J. Nanotechnol.* **2007,** *4* (5), 574-587.
2. Ge, L.; Xu, M. X.; Fang, H. B., Fabrication, characterization and photocatalytic activities of TiO_2 thin films from autoclaved-sol. *Thin Solid Films* **2007,** *515* (7-8), 3414-3420.
3. Hashimoto, K.; Irie, H.; Fujishima, A., TiO_2 photocatalysis: A historical overview and future prospects. *Jpn. J. Appl. Phys. Part 1* **2005,** *44* (12), 8269-8285.
4. Ihara, T.; Miyoshi, M.; Ando, M.; Sugihara, S.; Iriyama, Y., Preparation of a visible-light-active TiO_2 photocatalyst by RF plasma treatment. *J. Mater. Sci.* **2001,** *36* (17), 4201-4207.
5. Nakade, S.; Saito, Y.; Kubo, W.; Kitamura, T.; Wada, Y.; Yanagida, S., Influence of TiO_2 nanoparticle size on electron diffusion and recombination in dye-sensitized TiO_2 solar cells. *J. Phys. Chem. B* **2003,** *107*, 8607-8611.
6. Jun, J.; Shin, J.-H.; Dhayal, M., Surface state of TiO_2 treated with low ion energy plasma. *Appl. Surf. Sci.* **2006,** *252*, 3871-3877.
7. Dhayal, M.; Cho, S.-I.; Moon, J. Y.; Cho, S.-J.; Zykova, A., S180 cell growth on low ion energy plasma treated TiO_2 thin films. *Appl. Surf. Sci.* **2008,** *254*, 3331-3338.
8. Han, J.-B.; Wang, X.; Wang, N.; Wei, Z.-H.; Yu, G.-P.; Zhou, Z.-G.; Wang, Q.-Q., Effect of plasma treatment on hydrophilic properties of TiO_2 thin films. *Surf. Coat. Technol.* **2006,** *200*, 4876-4878.
9. Kim, Y.; Yoon, C.-H.; Kim, K.-J.; Lee, Y., Surface modification of porous nanocrystalline TiO_2 films for dye-sensitized solar cell application by various gas plasma. *J. Vac. Sci. Technol. A* **2007,** *25* (4), 1219-1225.
10. Jung, C.-K.; Bae, L.-S.; Song, Y.-H.; Boo, J.-H., Plasma surface modification of TiO_2 photocatalysts for improvement of catalytic efficiency. *Surf. Coat. Technol.* **2005,** *200*, 1320-1324.
11. Butoi, C. I.; Mackie, N. M.; Gamble, L. J.; Castner, D. G.; Barnd, J.; Miller, A. M.; Fisher, E. R., Deposition of highly ordered CF_2-rich films using continuous wave and pulsed hexafluoropropylene oxide plasmas. *Chem. Mater.* **2000,** *12* (7), 2014-2024.
12. Martin, I. T.; Malkov, G. S.; Butoi, C. I.; Fisher, E. R., Comparison of pulsed and downstream deposition of fluorocarbon materials from C_3F_8 and c-C_4F_8 plasmas. *J. Vac. Sci. Technol. A* **2004,** *22* (2), 227-235.
13. McCurdy, P. R.; Truitt, J. M.; Fisher, E. R., Comparison of oxidation rates for a-$Si_{1-x}C_x$:H films deposited from pulsed and continuous wave RF plasmas. *J. Electrochem. Soc.* **1998,** *145* (9), 3271-3277.
14. Kull, K. R.; Steen, M. L.; Fisher, E. R., Surface modification with nitrogen-containing plasmas to produce hydrophilic, low-fouling membranes. *J. Membr. Sci.* **2005,** *246*, 203-215.
15. Chen, C.; Bai, H.; Chang, C., Effect of plasma processing gas composition on the nitrogen-doping status and visible light photocatalysis of TiO_2. *J. Phys. Chem. C* **2007,** *111*, 15228-15235.

16. Bullock, E. L.; Patthey, L.; Steinemann, S. G., Clean and hydroxylated rutile TiO_2(110) surfaces studied by X-ray photoelectron spectroscopy. . *Surf. Sci.* **1996,** *352-354*, 504-510.
17. Cao, Y. A.; Yang, W. S.; Chen, Y. M.; Du, H.; Yue, P., Effect of chemisorbed surface species on the photocatalytic activity of TiO_2 nanoparticulate films. *Appl. Surf. Sci.* **2004,** *236*, 223-230.
18. Jing, L.; Xin, B.; Yuan, F.; Xue, L.; Wang, B.; Fu, H., Effects of surface oxygen vacancies on photophysical and photochemical processes of Zn-doped TiO_2 nanoparticles and their relationships. *J. Phys. Chem. B* **2006,** *110* (36), 17860-17865.
19. Chusuei, C. C.; Goodman, D. W.; Van Stipdonk, M. J.; Justes, D. R.; Loh, K. H.; Schweikert, E. A., Solid-liquid adsorption of calcium phosphate on TiO_2. *Langmuir* **1999,** *15* (21), 7355-7360.
20. Wang, L.-Q.; Baer, D. R.; Engelhard, M. H.; Shultz, A. N., The adsorption of liquid and vapor water on TiO_2 (110) surfaces: the role of defects. *Surf. Sci.* **1995,** *344* (3), 237-250.
21. Gao, X. T.; Wachs, I. E., Titania-silica as catalysts: molecular structural characteristics and phsyico-chemical properties. *Catal. Today* **1999,** *51*, 233-254.
22. McCafferty, E.; Wightman, J. P., Determination of the acid-base properties of metal oxide films and of polymers by contact angle measurements. In *Apparent and Microscopic Contact Angles*, Drelich, J.; Laskowski, J. S.; Mittal, K. L., Eds. VSP: Utrect, The Netherlands, 2000; pp 149-170.
23. McCafferty, E., Acid-base effects in polymer adhesion at metal surfaces. *J. Adhesion Sci. Technol.* **2002,** *16* (3), 239-255.
24. Zhang, J.; Wavhal, D. S.; Fisher, E. R., Mechanims of SiO_2 film deposition from tetramethylcyclotetrasiloxane, demiethyldimethoxysilane, and trimethylsilane plasmas. *J. Vac. Sci. Technol. A* **2004,** *22* (1), 201-213.
25. Steen, M. L.; Flory, W. C.; Capps, N. E.; Fisher, E. R., Plasma modification of porous structures for formation of composite materials. *Chem. Mater.* **2001,** *13* (9), 2749-2752.
26. Steen, M. L.; Hymas, L.; Havey, E. D.; Capps, N. E.; Castner, D. G.; Fisher, E. R., Low temperature plasma treatment of asymmetric polysulfone membranes for permanent hydrophilic surface modification. *J. Membr. Sci.* **2001,** *188*, 97-114.
27. Steen, M. L.; Jordan, A. C.; Fisher, E. R., Hydrophilic modification of polymeric membranes by low temperature water plasma treatment. *J. Membr. Sci.* **2002,** *204* (1-2), 341-357.
28. McCurdy, P. R.; Sturgess, L. J.; Kohli, S.; Fisher, E. R., Investigation of the PECVD TiO_2-Si(100) interface. *Appl. Surf. Sci.* **2004,** *233* (1-4), 69-79.
29. Suzer, S.; Dana, A.; Ertas, G., Differentiation of domains in composite surface structures by charge-contrast X-ray photoelectron spectroscopy. *Anal. Chem.* **2007,** *79*, 183-186.
30. Mizutani, T., Compositional and structural modifications of amorphous SiO_2 by low-energy ion and neutral beam irradiation. *J. Non-Cryst. Solids* **1995,** *181*, 123-134.

31. Machida, M.; Norimoto, K.; Watanabe, T.; Hashimoto, K.; Fujishima, A., The effect of SiO_2 addition in super-hydrophilic property of TiO_2 photocatalyst. *J. Mater. Sci.* **1999**, 2569-2574.
32. Zhou, J.; Martin, I. T.; Ayers, R.; Adams, E.; Liu, D. P.; Fisher, E. R., Investigation of inductively coupled Ar and CH_4/Ar plasmas and the effect of ion energy on DLC film properties. . *Plasma Sources Sci. Technol.* **2006,** *15* (4), 714-726.
33. Kim, J. S.; Rao, M.; Cappelli, M. A.; Sharma, S. P.; Meyyappan, M., Mass spectrometric and Langmuir probe measurements in inductively coupled plasmas in Ar, CHF_3/Ar and CHF_3/Ar/O_2 mixtures. *Plasma Sources Sci. Technol.* **2001,** *10* (2), 191-204.
34. Katsch, H. M.; Manthey, C.; Wagner, J. A.; Dobele, H. F., Negative ions in argon-oxygen discharges. *Surf. Coat. Technol.* **2005,** *200* (1-4), 831-834.
35. Chung, T. H.; Shin, Y. M.; Seo, D. C., Comparison of two methods of interpretation of Langmuir probe data for an inductively coupled oxygen plasma. *Contrib. Plasma Phys.* **2006,** *46* (5-6), 348-353.
36. Lee, Y. H., Surface damage threshold of Si and SiO_2 in electron-cyclotron-resonance plasmas. *J. Vac. Sci. Technol. A* **1992,** *10* (4), 1318-1324.
37. Meeks, E.; Larson, R. S.; Ho, P.; Apblett, C.; Han, S. M.; Edelberg, E.; Aydil, E. S., Modeling of SiO_2 deposition in high density plasma reactors and comparisons of model predictions with experimental measurements. *J. Vac. Sci. Technol. A* **1998,** *16* (2), 544-563.
38. Subramonium, P.; Kushner, M. J., Pulsed plasmas as a method to improve uniformity during materials processing. . *J. Appl. Phys.* **2004,** *96*, 82-93.
39. Joung, S. K.; Amemiya, T.; Murabayashi, M.; Itoh, K., Relation between photocatalytic activity and preparation conditions for nitrogen-doped visible light-driven TiO_2 photocatalysts. . *Appl. Catal. A* **2006,** *312*, 20-26.

CHAPTER 4

CONTROLLED NITROGEN DOPING AND FILM COLORIMETRICS IN POROUS TiO_2 MATERIALS USING PLASMA PROCESSING

This chapter contains data from a full paper published in *ACS Applied Materials & Interfaces.* The manuscript was written by Daniel J. V. Pulsipher and Ellen R. Fisher, and it was edited by Ina T. Martin who was working at the National Center for Photovoltaics at the National Renewable Energy Laboratory. This chapter examines the control over compositional and optical changes in creating nitrogen doped TiO_2 porous films and it makes assignments for both the nitrogen binding environments produced and the cause of various film colors observed.

4.1 Introduction

Although TiO_2 is widely used in photodevices, its wide bandgap absorbs only a small fraction of the solar spectrum, severely limiting its utility in both photovoltaics and photocatalytic devices. To circumvent this and improve its absorption efficiency, TiO_2 is often modified or sensitized, either directly or indirectly.[1] Indirect sensitization can be achieved through the use of dyes or inorganic quantum dots that more efficiently absorb solar radiation, such as in dye sensitized solar cells. Alternatively, TiO_2 can be more directly sensitized through the modification of its bulk or surface properties, often through

the introduction of dopants, a method that is commonly used to improve photocatalytic materials.

A variety of cationic and anionic dopants, including V, Cr, C, F, S, and N have been used to increase the visible light sensitivity of TiO_2.[2, 3] In the past 25 years,[4, 5] the photocatalytic functions of nitrogen doped TiO_2 (N:TiO_2) have been widely studied along with its potential use in photovoltaic devices.[6-8] Although N:TiO_2 can absorb lower energy solar radiation, the underlying cause of this change remains unclear. One hypothesis, based on the nitrogen chemical environment suggests the visible light sensitivity of N:TiO_2 is the result of N atoms doped into one of two different doping environments, referred to as substitutionally- and interstitially-doped N. These two moieties have XPS N 1s binding energies of 396 and 400 eV, respectively.[9, 10] Assignment of XPS N 1s spectral peaks to specific binding environments is often ambiguous and the inclusion of collective analyses of N 1s, Ti 2p, and O 1s binding regions, Fourier transform IR (FTIR) spectroscopy data, and literature peak assignment comparisons increase the reliability of peak assignments. Moreover, this type of comprehensive materials analysis can provide stronger correlations between N:TiO_2 dopant profiles and their respective photosensitivities.

In addition to ambiguities regarding N 1s XPS assignments and the origin of increased visible light sensitivity in N:TiO_2, disagreement also exists over whether introduction of nitrogen changes the material's bandgap. There are several mechanisms that have been proposed to explain this phenomenon. First, some researchers argue that the sensitivity to lower-energy photons is a result of localized states within the bandgap and not to a smaller bandgap.[11-13] Serpone and coworkers suggest the amount of dopant re-

quired to actually lower the bandgap of $N:TiO_2$ materials is much greater than commonly reported dopant levels of $\leq 8\%$.[1, 14, 15] One theoretical study found the bandgap of $N:TiO_2$ was lowered to 1.80 eV in films with >16.7% N-content is, with higher concentrations of N lowering the bandgap even further.[16] In contrast, other calculations report significantly lower $N:TiO_2$ bandgaps with as low as 2.8% nitrogen.[17] Nevertheless, photocatalytic devices tend to have better performances at low nitrogen doping values, specifically <1% nitrogen[5, 18]. An additional consideration is the point at which the material no longer behaves as doped TiO_2, but rather exhibits its own unique properties.

A second explanation for increased visible-light sensitivity of $N:TiO_2$ is that it arises from defect states, often described as color centers, oxygen vacancies (O_{vac}), or F-type centers, introduced by the doping process or the dopants themselves.[11, 19, 20] Here, F-type centers is used to describe three types of defects found in TiO_2: (a) F-centers, lattice sites where an anion has been replaced by two electrons; (b) F^+-centers, O_{vac} replaced by one electron, and (c) F^{++}-centers, which are equivalent to O_{vac}. Electrons trapped at F-type centers can be excited by photons, yielding various photoadsorption bands and concomitant color changes. Many nitrogen doping processes involve reducing agents, which favor formation of F-type centers. Indeed, the majority of anionic dopants produce a yellowing effect in TiO_2 materials.[9, 21] Additionally, $N:TiO_2$ reportedly has a lower activation energy for creating O_{vac} than TiO_2,[13, 17] suggesting nitrogen dopants stabilize or allow formation of F-type centers.[22]

A third possible explanation for the increased visible response of $N:TiO_2$ is plasmonic excitations. Plasmons give rise to intense colors in metallic nanoparticles, but are

also found in other conductive materials.[23] Bulk plasmons can absorb energy according to Equation 1,

$$\omega_p = (\frac{Ne^2}{m^* \varepsilon_0})^{1/2} \tag{4.1}$$

where ω_p is the plasmon frequency, N is the density of electrons in the valence band, e is the charge of an electron, m^* is the effective mass of the electrons, and ε_0 is the permittivity of free space.[24] In addition to bulk plasmons, surface plasmons also absorb photons with their frequency being a fraction of the bulk plasmon frequency. The three mechanisms for increased visible response in N:TiO_2 are, however, difficult to distinguish and may be substantially interrelated.

Here, we characterized the composition and optical properties of TiO_2 films treated in plasma discharges of different N-containing gases, giving rise to N:TiO_2 films with N-content of 6-34%. The photoelectric properties of N:TiO_2 are highly dependent on preparation conditions; thus we employed different plasma precursors, parameters, and post-plasma treatments to modify our TiO_2 films, resulting in materials with an array of binding environments, as measured with XPS. We have previously used nitrogen-based plasmas to modify the surface of a variety of materials.[25-27] Thus, the primary goals of this work were to (1) demonstrate the viability and controllability of plasma processing in creating N:TiO_2 materials and (2) explore potential origins for the resulting electronic properties. The ability to understand and control nitrogen incorporation will ultimately lead to improvements in photocatalytic and photovoltaic devices.

4.2 Results

XPS Compositional Analysis. XPS elemental composition data for TiO_2 films treated with different plasmas are listed in Table 4.1. An array of compositions was obtained, with average %N values ranging from 6.6 to 31.5%. The highest N-content is achieved using reductive plasma environments, suggesting NH_3 is more effective than N_2 or urea at promoting N-incorporation. Longer treatment times in NH_3 plasmas also resulted in higher N-content, regardless of the post plasma treatment. The films treated using NH_3(30)/NH_3, NH_3/NH_3, H_2,N_2/N_2, and H_2/NH_3 treatment schemes were all analyzed the same day as the plasma treatment in an attempt to limit the aging/oxidation upon exposure to atmosphere. Over time, the NH_3/NH_3 treated films gain O-content as a result of oxidation of less-stable nitrogen or titanium environment and eventually resemble the NH_3/O_2-treated films in atomic composition, Table 4.1. As anticipated, films exposed to an O_2 environment after plasma treatment contain more oxygen than those cooled under NH_3. The incorporation of nitrogen in H_2 plasma treated films that were cooled under NH_3 and N_2 demonstrate the reactivity of plasma reduced TiO_2 films. N_2/N_2 and H_2/N_2 treated films are very similar in % N-content. Higher N-content in N_2 plasma systems is achieved by first plasma reducing the films and then treating the films in a N_2 plasma, as in H_2,N_2/N_2 treated films. Films treated in urea plasmas for 2 and 10 min had similar amounts of nitrogen (data not shown), suggesting that the films saturate quickly.

The thermodynamic stability of TiO_2 over the N-TiO_2 materials studied here is manifested compositionally in post-treatment annealing. NH_3/NH_3 treated samples contain $21.0 \pm 2.1\%$ nitrogen, whereas an identical plasma treatment followed by a 30 min anneal results in a dramatic decrease in N-content to $6.6 \pm 1.0\%$.

Table 4.1. XPS Atomic Concentrations

Film Label	% N	% Ti	% O	% C	(O+N)/Ti	N/Ti
NH_3(30)/NH_3	31.5 ± 2.1	36.4 ± 0.9	31.3 ± 3.0	0.7 ± 0.6	1.73 ± 0.10	0.86 ± 0.04
NH_3/NH_3	21.0 ± 5.2	32.9 ± 2.7	40.9 ± 3.5	5.2 ± 5.2	1.88 ± 0.19	0.64 ± 0.15
NH_3(30)/O_2	23.9 ± 1.5	34.4 ± 0.2	40.5 ± 1.7	1.2 ± 1.1	1.87 ± 0.07	0.70 ± 0.04
NH_3/O_2	15.9 ± 0.4	31.6 ± 2.1	47.3 ± 0.4	5.1 ± 2.5	2.00 ± 0.02	0.51 ± 0.03
H_2,N_2/N_2	18.1 ± 1.9	32.9 ± 0.6	45.6 ± 2.7	3.5 ± 1.0	1.94 ± 0.10	0.55 ± 0.05
H_2/N_2	9.8 ± 3.2	31.9 ± 0.7	54.6 ± 6.2	3.8 ± 3.3	2.02 ± 0.22	0.31 ± 0.1
H_2/N_2 aged	7.3 ± 3.1	29.7 ± 0.5	58.5 ± 1.9	4.5 ± 1.7	2.22 ± 0.12	0.24 ± 0.10
H_2/NH_3	15.1 ± 2.8	33.3 ± 1.2	46.7 ± 0.6	3.81 ± 2.1	1.86 ± 0.09	0.45 ± 0.08
N_2/N_2	9.2 ± 1.1	31.4 ± 0.3	55.9 ± 1.4	3.5 ± 0.8	2.07 ± 0.06	0.29 ± 0.03
Annealed	6.6 ± 1.0	28.9 ± 0.9	62.0 ± 0.4	2.6 ± 0.6	2.37 ± 0.04	0.23 ± 0.04
Urea/NH_3	10.0 ± 1.4	23.6 ± 1.2	58.3 ± 3.2	7.3 ± 2.5	2.89 ± 0.15	0.43 ± 0.06
Untreated TiO_2	--	25.8 ± 0.8	62.9 ± 2.9	11.3 ± 3.7	2.44 ± 0.11	--

This trend also holds for longer annealing times (data not shown), although the N-content decreases more slowly with additional annealing time; specifically, after annealing for 120 min ~3% N-content remains. In contrast, oxygen incorporation increases from 40.9 ± 3.5% to 62.0 ± 0.4% upon annealing for 30 min.

Table 4.1 also lists N/Ti ratios for comparison to literature values and (O+N)/Ti ratios, which provide further insight into the Ti coordination in our materials. Specifically, an (O+N)/Ti ratio of 2 corresponds to TiO_2-like coordination of Ti when N and O are treated interchangeably. Similarly, an (O+N)/Ti ratio of 1 more closely resembles the Ti coordination in titanium nitride materials.[28] High (O+N)/Ti ratios are indicative of O terminated surfaces as discussed previously.[29] Based on these criteria, the (O+N)/Ti ratios suggest our films are more similar to titania or titanium oxynitride than to titanium nitride.

Given the high N-content in some of our materials, particularly NH_3(30)/NH_3 and NH_3(30)/O_2 treated films, we explored the retention of the characteristic crystal structure of anatase TiO_2 using XRD. Figure 4.1 shows XRD results from a TiO_2 sample subjected to the NH_3(30)/NH_3 treatment. All major peaks were assigned to either anatase TiO_2 or the FTO substrate. The film contains no rutile phases, and the absence of any TiN_x or $Ti_{3-\delta}O_4N$ peaks in these data, despite similarities in color, suggests that NH_3 plasma treatment does not cause the formation of additional crystalline polymorphs.[30] XRD data from annealed, NH_3/O_2, and NH_3(30)/O_2 treated films parallel those from the NH_3(30)/NH_3 treated sample with film peaks corresponding to the anatase structure.

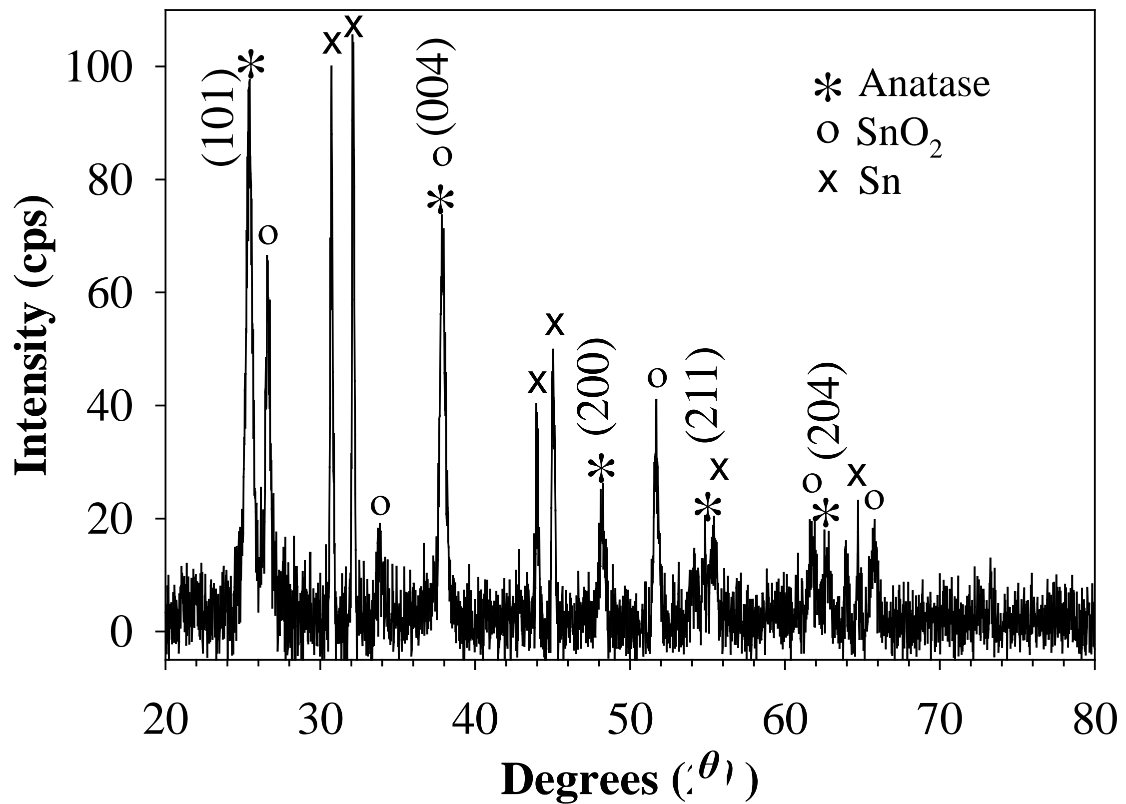

Figure 4.1. XRD of a NH_3(30)/NH_3 film where peaks with index labels correspond to peaks due to the film. The SnO_2 (110), (101), (200), (211), (310), and (301) peaks and the Sn (200), (101), (220), (211), (301), and (321) peaks arise from the conducting FTO substrate.

High resolution N 1s XPS spectra shown in Figure 4.2 illustrate the effect of processing parameters on films structure. Deconstruction of the spectra yields five distinguishable binding environments, designated as peaks 1-5, with respective binding energies of 396.3 ± 0.2, 397.2 ± 0.2, 398.4 ± 0.2, 399.9 ± 0.3, and 402.4 ± 0.2 eV. Several observations can be made from the spectra in Figure 4.2. Comparison of Figures 4.2a and 2b shows that for NH_3 plasma-treated materials, changing the post-treatment cooling environment from O_2 to NH_3 results in a decrease in the contribution of peak 1 and an increase in the contributions of peaks 2 and 3. These changes are more pronounced with increased plasma treatment time, Figure 4.2c. The urea plasma-treated sample, Figure 4.2d, displays a significantly different N 1s spectrum, with the dominant contribution coming from peak 4, along with a small contribution from peak 3. Comparison of Figures 4.2b and 4.2e show that annealing of the NH_3/NH_3 treated sample yields a dramatic increase in the contribution of peak 5. Figure 4.2e is representative of spectra for all annealed N-TiO_2 films wherein the incorporated nitrogen is found primarily in the peak 5 binding environment, regardless of its binding environment prior to annealing. Peak 5 does not change upon soaking in water, suggesting it is not a physisorbed species. After ~3 months of aging, the XPS spectrum for annealed films changes somewhat, with peak 5 remaining and peak 4 appearing along with a small N/Ti ratio change from 0.26 to 0.30. When annealed films are subjected to sputtering by 2 kV Ar^+, peak 5 decreases and peaks 1-4 appear, with peak 1 being the most intense after five or more minutes of sputtering. Other plasma treatments, Table 2.1, result in films with spectra that are comparable to those displayed in Figure 4.2.

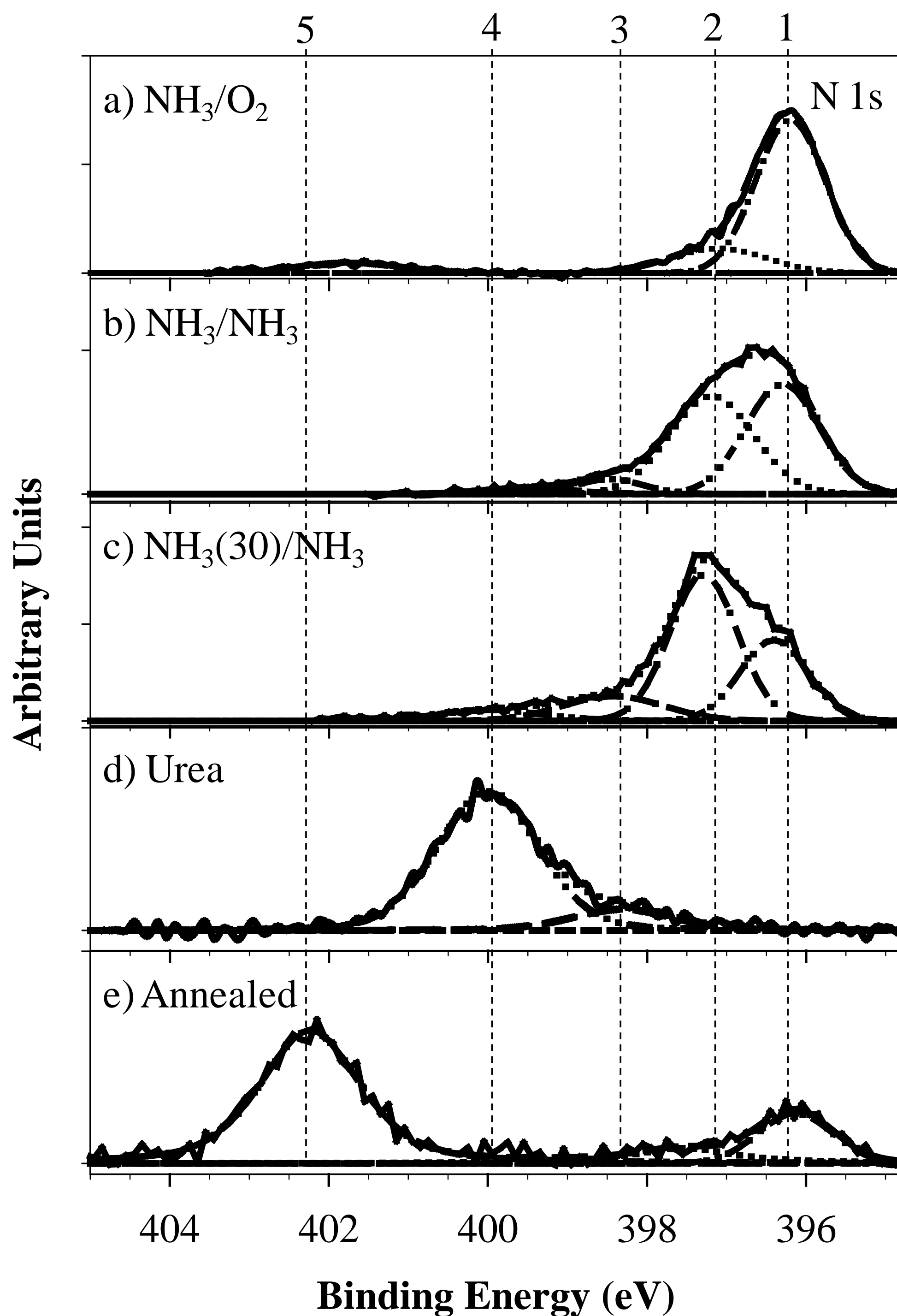

Figure 4.2. High resolution XPS N 1s spectra with deconstructed fits to the individual components. The vertical dashed lines represent peaks 1-5 located at 396.3 ± 0.2, 397.2 ± 0.2, 398.4 ± 0.2, 399.9 ± 0.3, and 402.4 ± 0.2 eV respectively.

Specifically, the spectrum in Figure 4.2a is representative of those found for N_2/N_2, $NH_3(30)/O_2$, and $H_2,N_2/N_2$ materials, and the spectrum in Figure 4.2b is representative of those for H_2/N_2 and H_2/NH_3 treated TiO_2.

Additional insight regarding the nitrogen binding in these films can be gained from the Ti 2p binding environments. The Ti $2p_{3/2}$ high resolution XPS spectra of the N:TiO_2 films are deconvoluted into five peaks, designated as peaks 1-5 with binding energies at 458.55 ± 0.07, 457.38 ± 0.14, 456.19 ± 0.08, 455.24 ± 0.06, and 454.23 ± 0.06 eV, respectively. The relative contributions of these peaks are listed in Table 4.2 as a function of the different treatments. The air unstable state (peak 5) only appears in films sputtered for > 5 min. XPS high resolution Ti 2p spectra are displayed in Figures 4.3a-e, with peaks 1-4 appearing as doublets ($2p_{3/2}$ and $2p_{1/2}$) from spin-orbit coupling. Untreated TiO_2 films, urea plasma-treated films, and annealed films have Ti 2p spectra dominated by peak 1, wherein > 90% of the titanium is in the $Ti(-O)_6$ binding environment corresponding to stoichiometric TiO_2. The appearance of peaks 2-4 in Figures 4.3a-c is, therefore, a reflection of the extent to which treatment affects the chemical environment of the titanium. More specifically, we associate lower-binding energy peaks with reduced titanium. From the data, it is clear that this effect is most pronounced in the case of the $NH_3(30)/NH_3$ treated films, Figure 4.3c. Additional data found in Table 4.2 show, for example, H_2/N_2 and H_2/N_2 aged films have spectra resembling that portrayed in Figure 4.3b. Common literature assignments and our most probable assignments for each Ti 2p binding environment are also listed in Table 4.2, and discussed further below.

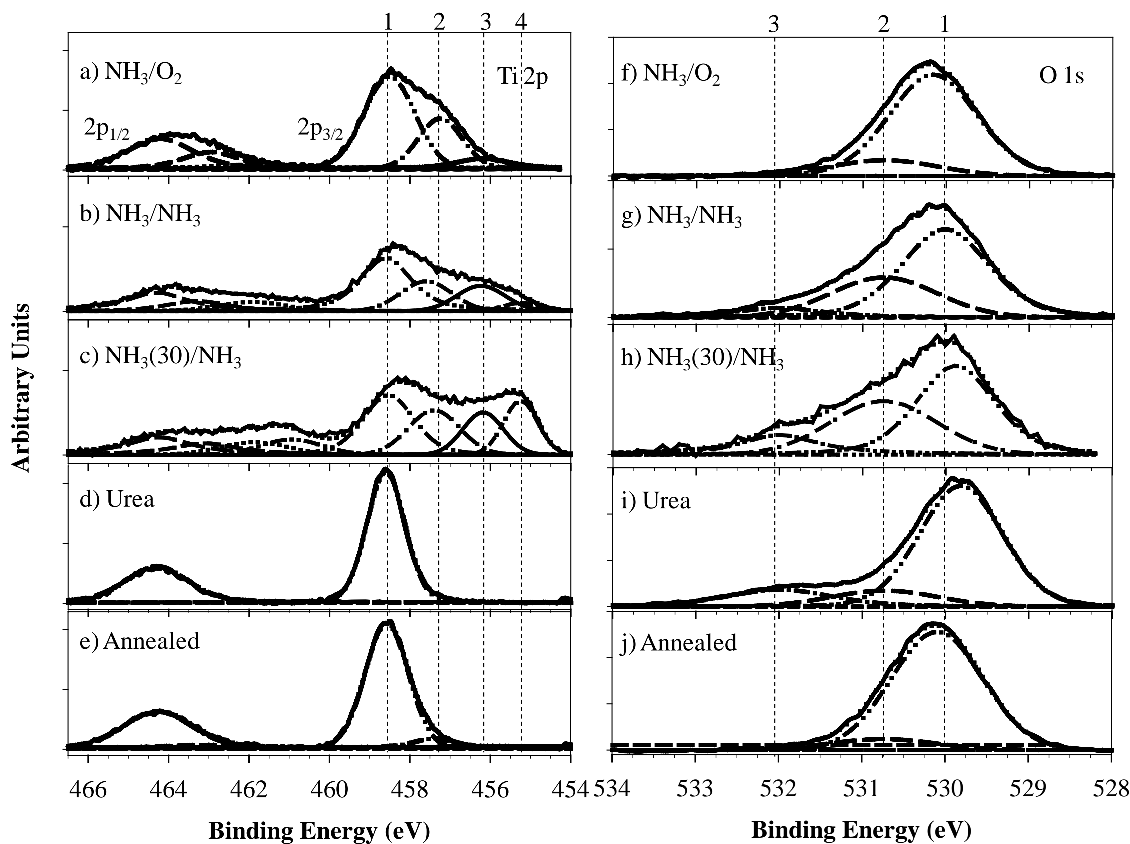

Figure 4.3. High resolution XPS spectra with deconstructed fits to the individual components for Ti $2p_{1/2}$ and Ti $2p_{3/2}$ peaks (left) with Ti $2p_{3/2}$ peaks 1-4 located at 458.55 ± 0.07, 457.38 ± 0.14, 456.19 ± 0.08, and 455.24 ± 0.06 eV, respectively; and O 1s peaks (right), with peaks 1-3 located at 530.0 ± 0.1, 530.7 ± 0.1, and 532.0 ± 0.1 eV, respectively.

Table 4.2. Percent relative peak area for decomposed XPS Ti $2p_{3/2}$ peaks[a]

Film Label	Peak 1 (%)	Peak 2 (%)	Peak 3 (%)	Peak 4 (%)	Peak 5 (%)	Color[b]
Sputtered (15 min)	34 ± 6	20 ± <1	16 ± 2	14 ± 3	17 ± 4	Black
NH_3(30)/NH_3	35 ± 4	24 ± 2	21 ± 4	19 ± 2	--	Black
NH_3/NH_3	50 ± 4	25 ± 1	18 ± 1	7 ± 5	<1	Dark Green
NH_3(30)/O_2	52 ± 3	29 ± 2	15 ± 1	3 ± 2	--	Dark Brown
NH_3/O_2	62 ± 3	33 ± 4	4 ± 1	<1	--	Gold
H_2,N_2/N_2	53 ± 6	33 ± 3	11 ± 3	2 ± 3	--	Yellow/Gold
H_2/N_2	60 ± 24	21 ± 8	12 ± 9	7 ± 8	<1	Dark Blue
H_2/N_2 aged	78 ± 6	14 ± 3	6 ± 2	1 ± 1	<1	Grey
N_2/N_2	78 ± 1	16 ± 1	5 ± 1	1 ± 1	--	Slightly Yellow
Annealed	93 ± 2	7 ± 2	<1	--	--	Slightly Yellow
Urea/NH_3	96 ± 2	4 ± 2	--	--	--	White
Untreated TiO_2	98 ± <1	2 ± <1	--	--	--	White
Literature Assignment	TiO_2	TiO_xN_y	TiO_xN_y	TiN_x	Ti^0, TiN_x	
Our Assignment	Ti(-O)$_6$	Ti(-O)$_5$ (-N)$_1$	Ti^{3+}(-O)$_5$ (-N)$_1$	Ti^{3+}(-O)$_4$ (-N)$_1$(-F^+)$_1$	Ti^{3+}(-N)$_3$, Ti^0, Ti^{3+}-F	

[a]Peaks 1-5 are located at 458.55 ± 0.07, 457.38 ± 0.14, 456.19 ± 0.08, 455.24 ± 0.06, and 454.23 ± 0.06 eV respectively. [b]Indicates color film appears upon removal from reactor or upon aging.

Table 4.3 explores the relationship between nitrogen and titanium binding environments. Specifically, the %N in peak 1 of the N 1s binding environment corresponds to the %Ti in peak 2 of the Ti 2p binding environment. Similarly, the %N found in peak 2 of the N 1s spectra parallels the amount of Ti found by combining peaks 3 and 4 of the Ti 2p spectra. Ti 2p peaks 3 and 4 can be grouped together due to their association with Ti^{3+} binding environments. In most N:TiO_2 films, the amount of N found in the N 1s peak 1 binding environment is roughly equivalent to the amount of Ti found in the Ti 2p peak 2 binding environment. The exceptions are the NH_3(30)/O_2, NH_3/O_2 , H_2,N_2/N_2 and N_2/N_2 films. The greater peak 1 %N found in these films is explained by a binding environment where multiple nitrogen atoms are in close proximity to a single titanium atom. A tetrahedral titanium atom bonded to electronegative oxygen atoms is capable of isolating two nitrogen atoms from each other to the extent that their binding environments are not distinguishable from that of one nitrogen atom. This leads to double counting of some of the N 1s peak 1 binding environments that represent the same Ti 2p peak 2 binding environment.

Similar to the high resolution O 1s spectra discussed in Chapter 3,[29] the O 1s spectra here were decomposed into peaks designated 1-3, Figures 4.3f-j, with binding energies of 530.0 ± 0.1, 530.7 ± 0.1, and 532.0 ± 0.1 eV, respectively. Peak 1, associated with the Ti(-O)$_6$ binding environment, dominates the spectrum of an untreated TiO_2 film, and as with the Ti 2p spectra, the presence of additional peaks indicates modification of the TiO_2 structure. Spectra for NH_3(30)/NH_3, NH_3/NH_3, and urea-plasma-modified films show an increase in the O 1s peaks 2 and 3 when compared to annealed and NH_3/O_2 modified films.

Table 4.3. Comparison of N 1s and Ti 2p XPS atomic percentages from each environment

Film Label	N atomic %		Ti atomic %		(N^*/Ti^*)[a]	Color
	Peak 1	**Peak 2**	**Peak 2**	**Peak 3+4**		
NH_3(30)/NH_3	8.8 ± 0.7	16.4 ± 1.4	9.1 ± 1.1	15.7 ± 1.1	1.0 ± 0.1	Black
NH_3/NH_3	10.9 ± 3	8.2 ± 2.2	8.9 ± 0.8	8.6 ± 1.5	1.2 ± 0.3	Dark Green
NH_3(30)/O_2	17.7 ± 1.3	6.2 ± 0.8	10.0 ± 0.7	6.2 ± 0.8	1.8 ± 0.1	Dark Brown
NH_3/O_2	14.5 ± 0.5	1.3 ± 0.3	10.4 ± 1.4	1.6 ± 0.3	1.4 ± 0	Gold
H_2,N_2/N_2	13.6 ± 1.5	4.5 ± 0.7	10.9 ± 1	4.3 ± 1.4	1.3 ±0.1	Yellow/Gold
H_2/N_2	5.2 ± 1.8	3.6 ± 1.4	6.7 ± 2.6	6.1 ± 3.8	0.8 ± 0.3	Dark Blue
H_2/N_2 aged	4.2 ± 1.8	1.4 ± 0.7	4.2 ± 0.9	2.1 ± 0.7	1.0 ± 0.4	Grey
N_2/N_2	7.6 ± 1	1.6 ± 0.3	5.0 ± 0.3	1.9 ± 0.4	1.5 ± 0.2	Slightly Yellow
Annealed	1.3 ± 0.2	0.2 ± 0	2.0 ± 0.6	--	0.7 ± 0.3	Slightly Yellow
Urea/NH_3	0.3 ± 0	--	0.9 ± 0.5	--	0.3 ± 0.5	White
Untreated TiO_2	--	--	0.5 ± 0.3	--	--	White

[a]N* is defined as the N atomic % represented by peak 1 and Ti* is defined as the Ti atomic % represented by peak 2.

Although not shown in Figure 4.3, O 1s spectra of NH_3(30)/O_2 and NH_3/O_2 treated films appear experimentally equivalent. O 1s peak assignments are discussed below.

The XPS N 1s spectrum of a 100% urea sample is similar to the N 1s spectrum of our urea plasma-treated films with the majority of the nitrogen existing in peak 4. During a urea plasma treatment, crystalline deposits build up on the reactor walls near the coil region, yet no wall depositions occur in the coil region. This is likely the result of a wall temperature difference. The N-content of our urea plasma-treated films decreases when placed in deionized water for several hours, indicating that the nitrogen in this binding environment is relatively water-soluble. To verify that the urea is not simply sputtered onto the TiO_2 films, the films were heated to 150 °C and pumped to 10 mTorr for 60 min, allowing any solid urea to sublime. Subsequent XPS analysis indicates the component at 399.9 eV still dominates the N 1s spectrum, but the total % N decreases significantly. Under these conditions, a 0.2 g urea pellet sublimes in minutes; therefore, solid urea is not redeposited onto the surface of these films.

Further insight into the nitrogen binding environments was pursued through FTIR spectroscopy, Figure 4.4. Broad peaks at ~3600-3000 cm^{-1}, attributed to the -OH stretch in water absorbed by TiO_2 limit our ability to separate $-OH_x$ from $-NH_x$ absorption peaks. In comparing FTIR spectra of urea and urea-plasma-modified films (Figures 4.4a and 4.4b), however, the FTIR absorbance peaks labeled 1-3 are more distinguishable in the spectrum of the urea pellet. These three absorbance bands (at ~3450, 3350 and 3200 cm^{-1}) are assigned to NH_2, NH, and -NH(C=O) stretching, respectively.

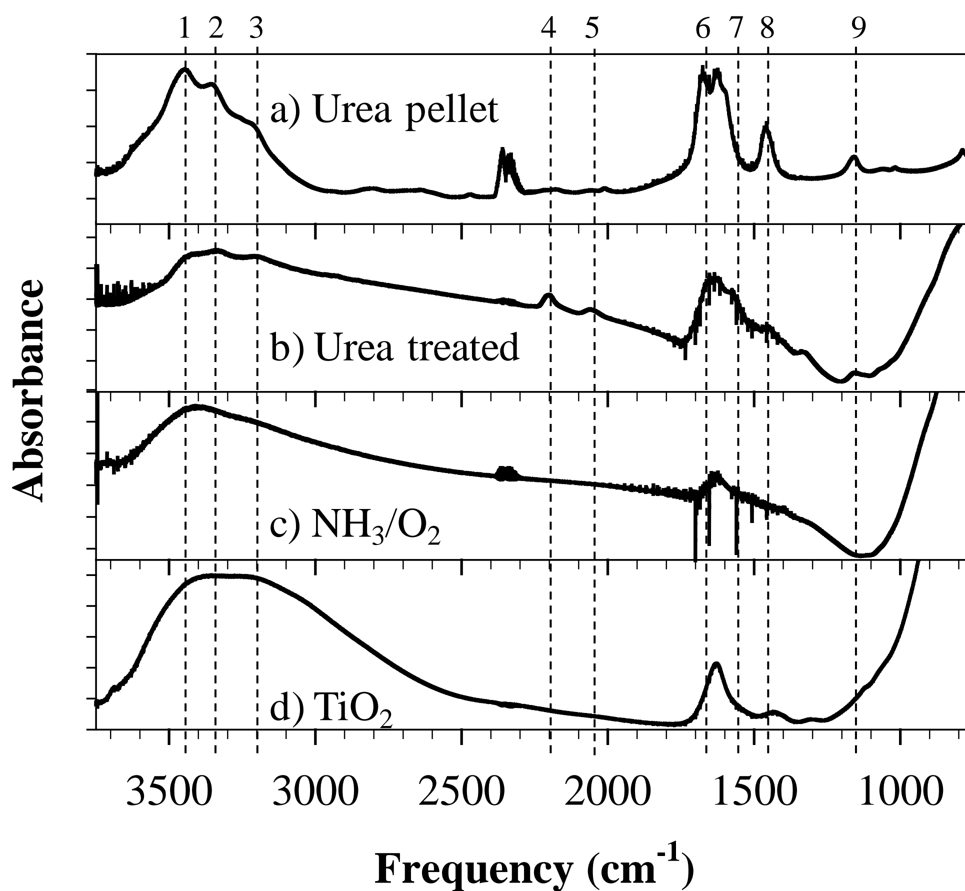

Figure 4.4. FTIR spectra of (a) urea mixed with KBr and (b-c) treated TiO_2 films scraped off of substrates and mixed with KBr. Vertical dashed lines represent peaks 1-9 located at 3450, 3350, 3200, 2100, 1675, 1625, 1575, 1450, and 1150 cm^{-1}, respectively.

The urea plasma-treated TiO_2 films give rise to more intense peaks at 2200, 2050, and 1575 cm^{-1} (absorption bands 4, 5, and 7 in Figure 4.4), and a much weaker absorption at 1450 cm^{-1} (peak 8). Absorption band 4 (~2200 cm^{-1}) is assigned to N=C=O stretching,[31] or -N=C=N functionality; band 5 (~2050 cm^{-1}) is assigned to C≡C or C≡N functionality; band 7 (~1575 cm^{-1}) arises from NH bending, again indicating no residual urea precursor in the urea plasma-treated sample; and band 8 (~1450 cm^{-1}) most likely arises from $-CH_2$, or -C-N species. Absorption bands 6 and 9 in spectra for both the urea pellet and the urea plasma-treated TiO_2, Figures 4.4a and 4.4b, were assigned to C=C, C=N, or -N-C=O species and NH_2 rocking or C-O stretching species, respectively. Differences in spectra shown in Figures 4.4a and 4.4b demonstrate urea is not simply being deposited onto the films. The spectra of the NH_3/NH_3 and $NH_3(30)/NH_3$ films are very similar to the spectrum shown in Figure 4.4c for the NH_3/O_2 film.

Optical Investigation. A striking aspect of our treated TiO_2 films is the wide range of color changes that occur as the white, untreated samples become shades of yellow, green, brown, blue, and black as a function of both the plasma and the post plasma treatment conditions, Figure 4.5. Notably, some of the samples change colors as they age, whereas others retain their colors permanently, Table 4.4. Although a description of these colorimetric changes is somewhat subjective, it does provide additional perspective on the structure and absorption properties of the materials.

After a 2 min NH_3 plasma exposure, the films turn a dark blue color. Depending on the post plasma treatment, the films turn colors ranging from a dark green to gold.

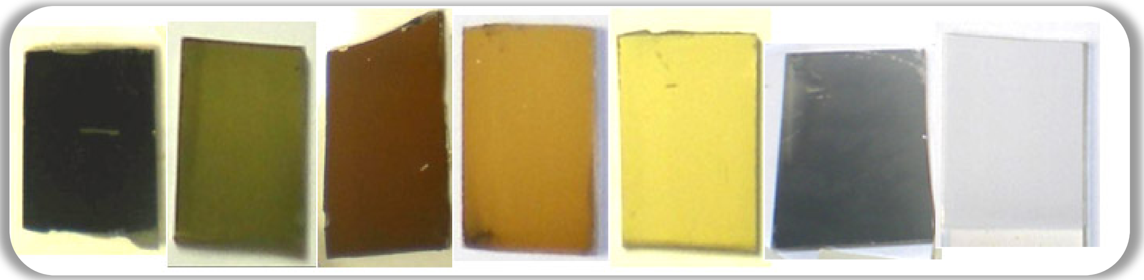

Figure 4.5. Photograph of films depicting the range of colors achieved via different film processing conditions, namely (left to right) NH_3/(30)NH_3, NH_3/NH_3, NH_3/(30)O_2, NH_3/O_2, H_2,N_2/N_2, H_2/N_2 aged, and urea/NH_3 treated films, respectively.

Table 4.4. Tauc bandgaps for modified films

Film Label	E_g(eV)[a]	Color
NH_3(30)/NH_3	--	Black
NH_3/NH_3	--	Dark Green
NH_3(30)/O_2	1.52 ± 0.01	Dark Brown
NH_3/O_2	2.05 ± 0.09	Gold
H_2,N_2/N_2	2.07 ± 0.16	Gold/Yellow
H_2/N_2	--	Dark Blue
H_2/N_2 aged	--	Grey
N_2/N_2	3.10 ± 0.09	Slightly Yellow
Annealed	2.93 ± 0.11	Slightly Yellow
Urea/NH_3	3.33 ± 0.01	White
Untreated TiO_2	3.34 ±0.07	White

[a]Values derived from UV-Vis spectra as described in the text.

Films allowed to rest under vacuum, argon, nitrogen, or an ammonia flow (NH_3/NH_3) displayed a dark green color and films resting under an oxygen atmosphere (NH_3/O_2) immediately appeared gold. NH_3/NH_3 modified films age considerably upon exposure to atmosphere, reverting to the gold color of the freshly-treated NH_3/O_2 films over a period of about one month. $NH_3(30)/NH_3$ and $NH_3(30)/O_2$ films become black and brown after treatment. Gold, black, and brown films do not appear to age for a period of at least five months. N_2 plasma treatments turn the TiO_2 films a faint yellow color and urea-plasma-modified films (with or without an ammonia carrier gas) appear yellow while still in the reactor under vacuum, but become white again after being removed from the reactor and exposed to atmosphere.

H_2 plasmas were used to create reactive sites on the TiO_2 surface, which were then allowed to react with a cooling gas, thereby indirectly introducing nitrogen to the film. After 2 min of H_2 plasma exposure, the films appear dark blue; subsequent exposure to NH_3, N_2, O_2, and NO_2 gas flows resulted in additional color changes. Films exposed to NH_3 range from dark blue to dark green colored films which become light green in a few days and ultimately turn gold after a few months. Films cooled under N_2 are dark blue and then age to a grey color. Films exposed to O_2 after a H_2 plasma treatment immediately turned a dull yellow color, and those exposed to N_2 become yellowish-gold in color. XPS spectra of H_2/NH_3 and H_2/N_2 treated films are indistinguishable from those of NH_3/NH_3 treated films, and we assume that the electrical properties of the latter are representative of all of these materials.

To quantify film color changes, we measured absorption spectra using diffuse reflectance UV-vis spectroscopy, Figure 4.6.

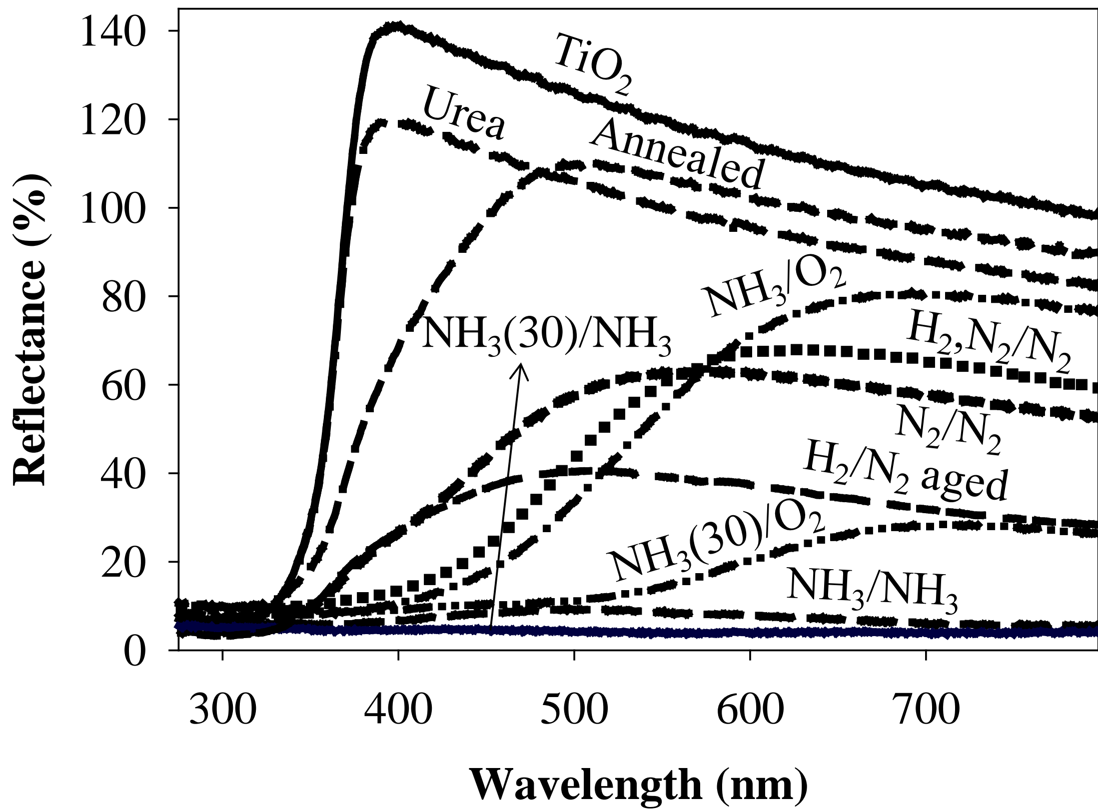

Figure 4.6. Diffuse reflectance UV-Vis spectra of TiO_2 films treated with different plasma treatments as labeled

The relative intensities of the spectra loosely correlate with the darkness of the films, with the highest and lowest intensities corresponding to white and black films, respectively. Urea plasma-treated films differ from the untreated films only in the slightly lower intensity of the signal. The progressively deeper shades of yellow seen in moving from annealed, to N_2/N_2, and to $H_2,N_2/N_2$ treated films are more discernible from their diffuse reflectance spectra, Figure 4.6. Aged H_2/N_2 treated films have a broad and diminished reflectance and $NH_3(30)/O_2$ treated films have a lower intensity corresponding to their dark brown color. As expected from their dark color, the NH_3/NH_3 and $NH_3(30)/NH_3$ modified films are extremely low in reflectance.

Tauc bandgaps are determined from the diffuse reflectance spectra by use of the Kubelka-Munk function.[32] E_g values, ranging from 1.52 to 3.33 eV, are calculated by fitting data in the linear portion of the absorption band edge of the Tauc plots, Table 4.4. The indirect bandgap for anatase TiO_2 is ~3.2 eV,[33] although higher experimental bandgaps (3.3 - 3.5 eV) have been reported.[34, 35] The $NH_3(30)/O_2$ treated films display the lowest accurately determinable E_g. Upon aging, the E_g values for NH_3/NH_3 treated films approach those of NH_3/O_2 treated films (~2 eV). Poor reflectance signal and/or non-linearity of the band edge precluded calculation of E_g values for H_2/N_2 aged, NH_3/NH_3, and $NH_3(30)/NH_3$ films. To explicitly connect the electrical properties of these films with the compositional analysis achieved from XPS, Figure 4.7 demonstrates the correlation between E_g and %N in the N 1s peak 1 environment, and Figure 4.8 shows E_g values as a function of the N*/Ti* ratios, Table 4.3. The connection between these data and the underlying mechanisms for nitrogen incorporation are discussed in more detail below.

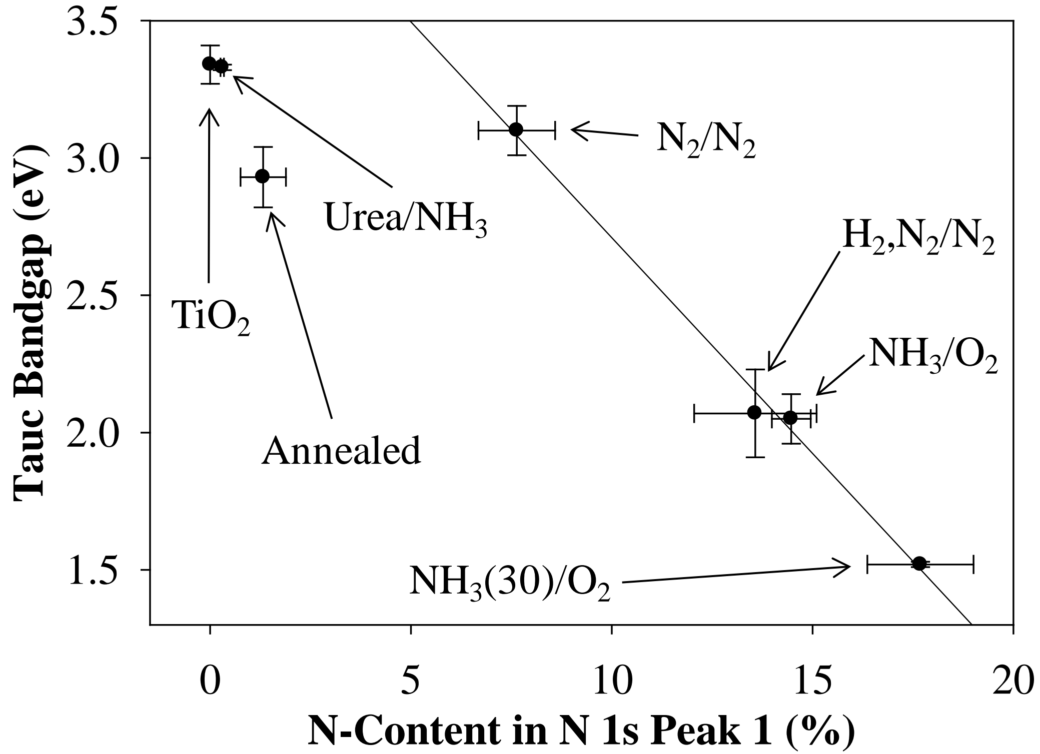

Figure 4.7. The correlation between calculated E_g and amount of nitrogen in the N 1s peak 1 environment for plasma-nitrided films. These data support a localized-nitrogen-dopant light-absorption mechanism.

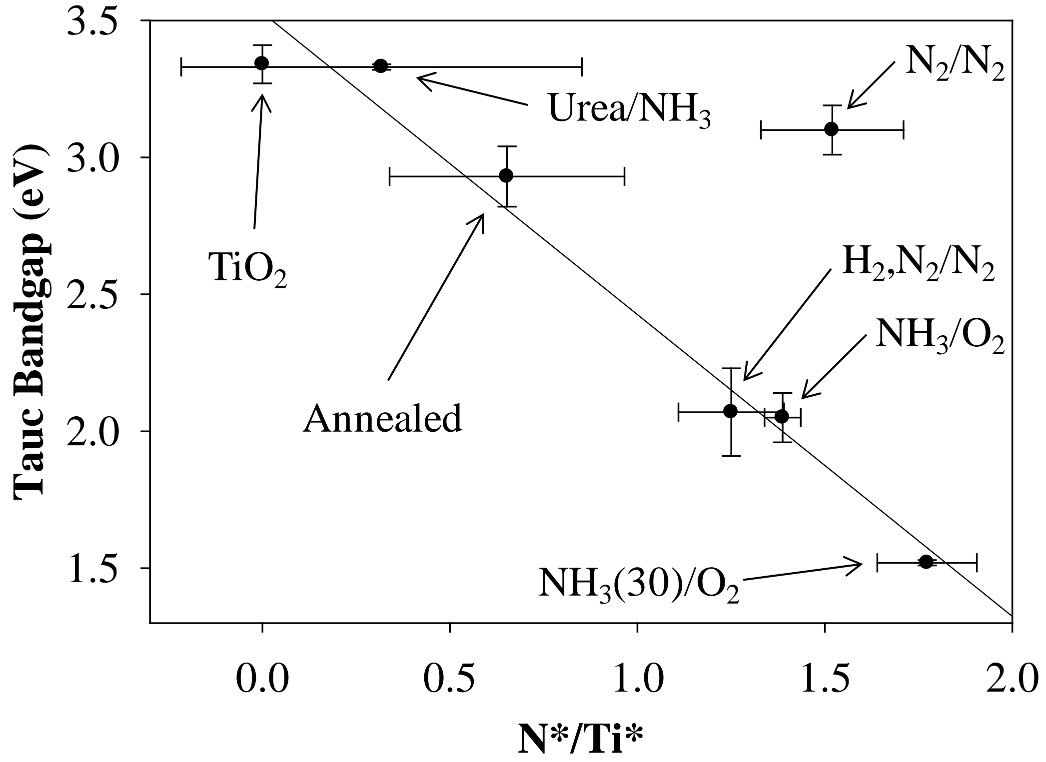

Figure 4.8. Correlations between calculated E_g and N*/Ti* ratios calculated in Table 4.3. These data support a plasmonic light absorption mechanism.

4.3 Discussion

As noted in the Introduction, the primary goals of this work were to explore the use of nitrogen-containing plasmas to controllably produce N:TiO_2 and to examine the underlying mechanisms for doping resulting in increased sensitivity to visible light. Thus, this work has focused on the characterization of our plasma-modified materials utilizing primarily XPS, FTIR, and diffuse reflectance UV-vis spectroscopy to analyze the resulting film properties.

Production and Control of N Doping. N:TiO_2 films produced here contain only anatase domains with the highest N/Ti ratios reported to date of up to 0.90. No evidence of TiN or cubic phased oxynitride[36] crystallinity in either NH_3(30)/NH_3 or NH_3(30)/O_2 treated films is observed. For crystalline phases other than anatase TiO_2 to form, higher film temperatures would be required than those reached in our plasma treatments. Because XRD completely penetrates the films, anatase phased TiO_2 could be anywhere in the nanoparticle films and the films with high N-content could have amorphous titanium nitride regions. Treatment of TiO_2 in a reducing plasma environment (i.e. in the presence of NH_3 or H_2), yields higher nitrogen loading over a short time. In the literature, N/Ti ratios range from 0.02 to 0.36, with the most common ratio being ~0.1, corresponding to N:TiO_2 with ~5% nitrogen.[37-43] The highest nitrogen doping for amorphous TiO_2 films is ~28%.[44] Similarly, ≤23% nitrogen was reported in rutile films heated to 800 °C and 49% in TiO_2 nitrided to mostly crystalline TiN at 1100 °C for 5 hrs.[45] Notably, high surface oxidation of our porous films is evident by high surface concentrations of oxygen and by the majority Ti(-O)$_6$ binding environments found in all treated films, Table 4.2. Additionally, the (O+N)/Ti ratios in Table 4.1 reflect a titania or titanium oxynitride material.

A major tool used to describe the nitrogen in N:TiO_2 films is high resolution N 1s XPS spectra as these provide substantial information on the chemical environment (although not specific chemical bonds) of the nitrogen atoms in the film. Peaks 1 and 2 in N 1s spectra for N:TiO_2, Figure 4.2, are sometimes combined in the literature. Studies of the controlled oxidation of titanium nitride materials suggest, however, that these are two distinct binding environments.[46-48] Recently Zhang and coworkers recognized this distinction in high temperature nitridation of TiO_2 and argued that peak 1 was a titanium oxynitride.[45] This peak is more often assigned to Ti-N or β-N bonding species which are found in TiN_x materials.[49] To clarify the analysis of N 1s data in the present work, we examined the O 1s and Ti 2p spectra of our NH_3/O_2 films, Figure 4.3. The O 1s spectrum has no features at 532 eV, the region that would be consistent with N-O or oxynitride species.[45] By comparison, literature assignments indicate peak 2 in the Ti 2p spectrum, observed in our films, is an oxynitride.[49, 50] Given that our XRD data indicate the prevalence of the anatase structure, we have designated peak 2 in the Ti 2p spectrum to a $Ti(-OTi_2)_5(-NTi_2)_1$ or $Ti(-OTi_2)_4(-NTi_2)_2$ environment. Thus, our assignment of peak 1 in the N 1s region to an $N(-TiO_5)_3$ or $N(-TiO_5)_2(-TiO_4N)_1$ binding environment is consistent with the Ti 2p spectrum and with Ti atoms in the Ti^{4+} oxidation state. These Ti 2p (peak 2) and N 1s (peak 1) environments arise from substitutional nitrogen doping where oxygen atoms are replaced with nitrogen atoms. The titanium is in a more reduced environment, yet not enough to formally represent a Ti^{3+} oxidation state.

The N 1s peak 2 has previously been assigned to TiN_x with a binding energy range of 397.1-397.5 eV, depending on the N/Ti ratio.[51, 52] Peak 2 constitutes the majority of the N 1s region in spectra of NH_3/NH_3 and NH_3(30)/NH_3 films. The significant dif-

ference in binding energy for peak 2 in spectra of these two films, Figure 4.2, results from the change in TiN_x content. The Ti 2p and O 1s XPS spectra for these materials support this N 1s peak assignment. Peak 3 in the Ti 2p spectra has been assigned to an alternative oxynitride species and to Ti^{3+} species in Ti_2O_3 and TiN type materials.[50, 53, 54] Additionally the darker color observed has been attributed to the creation of O_{vac},[55, 56] and to the Ti^{3+} to Ti^{4+} optically allowed transition.[57] Based on literature assignments, the number of deconstructed Ti 2p peaks, and the stability of the binding environments, peak 3 (Ti 2p) is assigned to $Ti^{3+}(-OTi_2)_5(-NTi_2)_1$. Peak 4 (Ti 2p) is assigned to a similar environment wherein the Ti^{3+} is bonded to more nitrogen atoms or some of the connecting oxygen atoms are replaced by F-type centers. The increased intensity of the O 1s peaks 2 and 3 in spectra of $NH_3(30)/NH_3$ films relative to NH_3/NH_3 films could indicate fewer lattice oxygen atoms and more Ti^{3+} states onto which hydroxyl and carboxyl species have absorbed.[58, 59] Thus, peak 2 in the N 1s spectrum originates from a titanium nitride-type environment with the titanium in a Ti^{3+} state. Notably, the N-Ti^{3+}-O species appears at a higher N 1s binding energy than N-Ti^{4+}-O as the Ti oxidation state strongly influences binding energy. The chemical structure of this environment probably resembles $N(-Ti^{3+}O_5)_1(-Ti^{4+}O_5)_2$ or a hydrogenated titanium nitride species where the titanium has been reduced to Ti^{3+}.

We also explored the origin of the N 1s signal at 399.9 ± 0.2 eV (peak 4), which appears only in the spectrum of urea plasma-treated films. Peak 4 has been assigned to interstitially doped nitrogen,[9, 60] Ti-O-N,[14] Ti-N-O,[10] Ti-O-N-O,[61] NH_x species,[62, 63] chemisorbed N_2 species,[64] and molecularly absorbed γ-N_2 species.[65, 66] The common peak assignment of absorbed γ-N species can be traced to Shinn and coworkers from ni-

tridation of Cr/W where they assigned the 400 and 405 eV peaks to well and poorly screened vertically absorbed N_2 molecules.[67] Here, the nitrogen binding environment in H_2/N_2 films were similar to NH_3/NH_3 films where the 399.9 eV peak constituted only a small percentage of the N 1s region (10 ± 1%). Additional C-content and higher binding energy peaks in the C 1s XPS spectra of urea plasma-treated films suggest surface oxide or amide type carbon species. Higher binding energy peaks in the corresponding O 1s spectra indicate carbonyl or NO oxygen species. From the XPS data alone, we cannot discern the origin of the N 1s peak 4. Differences in FTIR spectra obtained from a urea pellet and urea plasma-treated films, Figure 4.4, permit a more specific assignment of the N 1s peak 4. Using the FTIR assignments given above and the solubility of this environment, peak 4 (399.9 eV) likely arises from weakly bound adsorbates with functional groups that promote water solubility (e.g. -NH-CH=O, -N=C=O, -N=C=N-, and -NH-COH=NH).

Also of interest is the shift toward higher binding energies that accompanies annealing of N:TiO_2 films, yielding a peak at 402.4 ± 0.2 eV (peak 5). Signal in this region has been attributed to interstitially doped nitrogen, NO π* character, γ-N, molecular N_2, and oxynitride species.[14,65, 68] Upon annealing, the lower binding energy nitrogen environments represented by peaks 1-4 migrate to this higher binding energy environment. Shinn and coworkers observe the opposite phenomenon when their films are annealed in vacuum from 80-1350 K, with nitrogen in the higher N 1s binding energy environment supplying the nitrogen that migrates to a more reduced state. Our data suggest the 402.4 eV binding environment refers to a chemisorbed or trapped species as it does not dissolve in water. The Ti 2p spectra of annealed films show peak 2 accounting for 7 ± 2% of the

Ti 2p region, assigned to an intermediate oxynitride species. Given the lack of a N-O signal in the O 1s spectrum, however, it seems more likely that the N 1s signal at 402.4 eV arises from interstitial nitrogen dopants such as trapped N_2, or -N=N- species which are more influenced by Ti^{4+} sites than O^{2-} sites. These species form during the annealing process and then substitutionally order themselves during Ar^+ sputtering.

Possible Optical Mechanisms. Visual changes in TiO_2 that accompany nitrogen doping are closely related to the simultaneous enhancement of the material's photosensitivity. The origin of these color changes remains unclear, with possible mechanisms including lowered bandgaps, intra-bandgap localized dopant states, intra-bandgap F-type centers, or plasmonic excitations. The first two are supported by the idea that specific XPS N 1s binding environments cause the visible light sensitivity of N:TiO_2 materials. Lower E_g values could, however, result from any of the above mentioned phenomena. In practice, these explanations are all closely related. Lowered bandgaps can be caused by high concentrations of inter-bandgap localized dopants or F-type centers; plasmonic energies can be altered by trapping charges at various sites. Although this makes distinguishing between mechanisms difficult, photocatalytic and photovoltaic properties of these materials depend heavily on photoabsorption mechanisms.

When TiO_2 is progressively doped with nitrogen, the nitrogen could initially form localized states within the bandgap of the material. Upon further doping, these states could begin to broaden and overlap, causing absorption of progressively lower energy photons. This phenomena is observed in nitrogen doped diamond where yellow through black diamonds are produced at high nitrogen doping.[69] In this case, the amount of a specific nitrogen environment in the films would cause the color changes. Our E_g values

for annealed and N_2/N_2 treated films deviate from this argument as two different N 1s binding environment display similar colors. Their E_g values overlap, yet the majority of the incorporated nitrogen is chemically different. This idea cannot be ruled out, however, because the grey, yellow, gold, and brown colors of other films appear to change with the amount of nitrogen in the N 1s peak 1 environment, Table 4.3 and Figure 4.7. In fitting the Figure 4.7 data, both the annealed and urea treated films were not included in the linear regression analysis because both have significant contributions from other binding environments besides the N 1s peak 1 environment. Thus, the linear trend begins with N_2/N_2 treated films which have the least amount of nitrogen in the N 1s peak 1 environment and, therefore, the least amount of localized nitrogen band broadening.

F-type centers could also cause the optical absorption differences in our $N:TiO_2$ materials. If defect states such as Ti^{4+}-F^{++},Ti^{4+}-F^{+}, Ti^{4+}-F, and Ti^{3+}-F^{+} environments were detectable in the XPS spectra, their concentration would have to be >1000 ppm and F-type centers in concentrations of <1000 ppm can be sufficient to cause color changes. From the Ti 2p peak assignments and relative contribution data, Tables 4.2 and 4.3, we infer peak 4 in the Ti 2p spectrum is associated with F-type centers and nitrogen in the N1s peak 2 environment. The dark films resulting from NH_3(30)/NH_3, NH_3/NH_3, H_2/N_2, and NH_3(30)/O_2 treatments all contain >3% Ti in the Ti 2p peak 4 environment. If the concentration of F-type centers is high enough, a shallow conduction band could develop; thus, these films could be dark because of high densities of Ti^{3+} sites or F-type centers which are highly interrelated.[70] The behavior of NH_3/NH_3 and H_2/NH_3 films over time provides strong indicators for F-type centers. Specifically, peaks 3 and 4 in the Ti 2p spectra decrease in intensity over time, accompanied by color changes from dark green to

light green and then to gold with no loss of nitrogen, but a gain in oxygen. All of these data support the conclusion that peak 4 is clearly associated with F-centers, although electron paramagnetic resonance data are needed to definitively detect F^+-centers.

Interestingly, the plasmon frequency of TiN_x films produces similarly colored films depending on the N/Ti ratio. They can appear grey (N/Ti < 1), yellow or gold (N/Ti ≈ 1), and brown (N/Ti > 1).[71-74] These colors are similar to those observed for our N:TiO_2 films with the same trend in nitrogen composition. As more nitrogen is added, fewer valance band electrons are available and lower energy plasmons can be created according to equation (1). Available valance electrons could be trapped by localized nitrogen dopants, F-type centers, or other defects. Bendavid and coworkers found that plasmons are not excited at N/Ti ratios as low as 0.34 in films with TiN_x containing < 3% oxygen.[71] A similar cutoff value of N/Ti could apply to these N:TiO_2 materials. Plasmon energies (ω_p) are known to shift linearly from 3.2 to 2.4 eV for TiN_x materials;[71, 74] therefore, the concept of smaller E_g values resulting from plasmonic adsorption is probable. Table 4.3 N*/Ti* ratios are comparable to N/Ti ratios for TiN_x materials and correlate with E_g values, Figure 4.8. The N_2/N_2 treated films are an obvious outlier in Figure 4.8, which likely arises from the influence of hydrogen in these systems. Notably, the slightly yellow color of the annealed films does not initially fit the plasmon explanation as these films should have a grey color given the small amount of nitrogen in peak 1 (N 1s) and the concomitantly low N*/Ti* ratio. The majority of the nitrogen in annealed films appears in higher binding environments and likely contributes somewhat to reducing valance band electrons. Thus, the films appear yellow instead of grey. The E_g for urea plasma-treated films is not significantly different than untreated TiO_2, most likely be-

cause the nitrogen (largely peak 4) does not significantly affect ω_p. The grey H_2/N_2 aged films also fit this plasmonic absorption mechanism even though E_g was not determined. Although plasmons are a reasonable explanation for the color of these films, further experimentation is needed to confirm the existence of plasmonic excitations.

4.4 Summary

Nitrogen doping of mesoporous TiO_2 with a range of N-content (6-34%) has been achieved via plasma modification, resulting in low E_g anatase phased N:TiO_2. The nitrogen environments are controlled by different nitrogen containing precursors as well as post plasma processing. Overall, assignments of the observed XPS N 1s binding environments were elucidated as: peak 1(396.3 ± 0.2 eV) is substitutional doped N(-TiO_5)$_3$ or N(-TiO_5)$_2$(-TiO_4N)$_1$ species; peak 2 (397.2 ± 0.2 eV) is attributed to N(-$Ti^{3+}O_5$)$_1$(-$Ti^{4+}O_5$)$_2$ or a hydrogenated hybrid of this species; peak 3 (398.4 ± 0.2 eV) was not assigned as it was not well isolated; peak 4 (399.8 ± 0.2 eV) correlates to absorbed -NH-CH=O, -N=C=O, N=C=N, and/or NH-COH=NH type species; and peak 5 (402.4 ± 0.2 eV), found in annealed films, corresponds to trapped N_2, or -N=N- type species. The N:TiO_2 films were grey, yellow, gold, brown, dark green, dark blue and black. The colors of oxidized films (grey-brown) could be explained both by localized nitrogen dopants and by plasmonic excitations, whereas darker colored films are a result of Ti^{3+} sites and F-type centers. Ultimately, the performance of these materials in solar cell devices and/or in photocatalytic processes is of significant interest. Additional studies utilizing our N:TiO_2 materials in photovoltaic and photocatalytic devices is reported in Chapter 5.

4.5 References

1. Emeline, A. V.; Kuznetsov, V. N.; Rybchuk, V. K.; Serpone, N., Visible-light-active titania photocatalysts: The case of N-doped TiO(2)s-properties and some fundamental issues. *International Journal of Photoenergy* **2008**.
2. Cui, Y.; Du, H.; Wen, L. S., Doped-TiO_2 photocatalysts and synthesis methods to prepare TiO_2 films. *J. Mater. Sci. Technol.* **2008,** *24* (5), 675-689.
3. Du, H.; Wen, L. S., Doped-TiO_2 photocatalysts and synthesis methods to prepare TiO_2 films. *J. Mater. Sci. Technol.* **2008,** *24* (5), 675-689.
4. Sato, S., Photocatalytic activity of NO_x-doped TiO_2 in the visible-light region. *Chem. Phys. Lett.* **1986,** *123* (1-2), 126-128.
5. Asahi, R.; Morikawa, T.; Ohwaki, T.; Aoki, K.; Taga, Y., Visible-light photocatalysis in nitrogen-doped titanium oxides. *Science* **2001,** *293* (5528), 269-271.
6. Ma, T. L.; Akiyama, M.; Abe, E.; Imai, I., High-efficiency dye-sensitized solar cell based on a nitrogen-doped nanostructured titania electrode. *Nano Letters* **2005,** *5* (12), 2543-2547.
7. Chambers, S. A.; Cheung, S. H.; Shutthanandan, V.; Thevuthasan, S.; Bowman, M. K.; Joly, A. G., Properties of structurally excellent N-doped TiO_2 rutile. *Chem. Phys.* **2007,** *339* (1-3), 27-35.
8. Cheung, S. H.; Nachimuthu, P.; Joly, A. G.; Engelhard, M. H.; Bowman, M. K.; Chambers, S. A., N incorporation and electronic structure in N-doped TiO_2(110) rutile. *Surf. Sci.* **2007,** *601* (7), 1754-1762.
9. Fujishima, A.; Zhang, X. T.; Tryk, D. A., TiO_2 photocatalysis and related surface phenomena. *Surf. Sci. Rep.* **2008,** *63* (12), 515-582.
10. Romero-Gomez, P.; Rico, V.; Borras, A.; Barranco, A.; Espinos, J. P.; Cotrino, J.; Gonzalez-Elipe, A. R., Chemical state of nitrogen and visible surface and schottky barrier driven photoactivities of N-doped TiO_2 thin films. *J. Phys. Chem. C* **2009,** *113* (30), 13341-13351.
11. Serpone, N., Is the band gap of pristine TiO_2 narrowed by anion- and cation-doping of titanium dioxide in second-generation photocatalysts? *J. Phys. Chem. B* **2006,** *110* (48), 24287-24293.
12. Kuznetsov, V. N.; Serpone, N., On the origin of the spectral bands in the visible absorption spectra of visible-light-active TiO_2 specimens analysis and assignments. *J. Phys. Chem. C* **2009,** *113* (34), 15110-15123.
13. Finazzi, E.; Di Valentin, C.; Selloni, A.; Pacchioni, G., First principles study of nitrogen doping at the anatase TiO_2(101) surface. *J. Phys. Chem. C* **2007,** *111* (26), 9275-9282.
14. Dong, F.; Zhao, W. R.; Wu, Z. B.; Guo, S., Band structure and visible light photocatalytic activity of multi-type nitrogen doped TiO_2 nanoparticles prepared by thermal decomposition. *J. Hazard. Mater.* **2009,** *162* (2-3), 763-770.
15. Wang, Y. Q.; Yu, X. J.; Sun, D. Z., Synthesis, characterization, and photocatalytic activity of $TiO_{2-x}N_x$ nanocatalyst. *J. Hazard. Mater.* **2007,** *144* (1-2), 328-333.
16. Xue, J. B.; Li, Q.; Liang, W.; Shang, J. K., Electronic band structures of TiO_2 with heavy nitrogen doping. *Journal of Wuhan University of Technology-Materials Science Edition* **2008,** *23* (6), 799-803.

17. Chen, Q. L.; Tang, C. Q.; Zheng, G., First-principles study of TiO_2 anatase (101) surfaces doped with N. *Physica B* **2009,** *404* (8-11), 1074-1078.
18. Braun, A.; Akurati, K. K.; Fortunato, G.; Reifler, F. A.; Ritter, A.; Harvey, A. S.; Vital, A.; Graule, T., Nitrogen doping of TiO_2 photocatalyst forms a second e(g) state in the oxygen 1s NEXAFS pre-edge. *J. Phys. Chem. C* **2010,** *114* (1), 516-519.
19. Giannakopoulou, T.; Todorova, N.; Osiceanu, P.; Lagoyannis, A.; Vaimakis, T.; Trapalis, C., Description of TiO2 thin films treated in NH_3 atmosphere by optical dispersion models. *Thin Solid Films* **2009,** *517* (24), 6694-6699.
20. Tessier, F.; Zollfrank, C.; Travitzky, N.; Windsheimer, H.; Merdrignac-Conanec, O.; Rocherulle, J.; Greil, P., Nitrogen-substituted TiO_2: investigation on the photocatalytic activity in the visible light range. *Journal of Materials Science* **2009,** *44* (22), 6110-6116.
21. Shankar, K.; Basham, J. I.; Allam, N. K.; Varghese, O. K.; Mor, G. K.; Feng, X. J.; Paulose, M.; Seabold, J. A.; Choi, K. S.; Grimes, C. A., Recent advances in the use of TiO_2 nanotube and nanowire arrays for oxidative Photoelectrochemistry. *J. Phys. Chem. C* **2009,** *113* (16), 6327-6359.
22. Oropeza, F. E.; Harmer, J.; Egdell, R. G.; Palgrave, R. G., A critical evaluation of the mode of incorporation of nitrogen in doped anatase photocatalysts. *Phys. Chem. Chem. Phys.* **2010,** *12*, 960-969.
23. Rhodes, C.; Franzen, S.; Maria, J. P.; Losego, M.; Leonard, D. N.; Laughlin, B.; Duscher, G.; Weibel, S., Surface plasmon resonance in conducting metal oxides. *J. Appl. Phys.* **2006,** *100* (5).
24. Maier, S. A., *Plasmonics: Fundamentals and Applications*. Springer: New York, 2007.
25. Butoi, C. I.; Steen, M. L.; Peers, J. R. D.; Fisher, E. R., Mechanisms and energy transfer for surface generation of NH_2 during NH_3 plasma processing of metal and polymer substrates. *J. Phys. Chem. B* **2001,** *105* (25), 5957-5967.
26. Kull, K. R.; Steen, M. L.; Fisher, E. R., Surface modification with nitrogen-containing plasmas to produce hydrophilic, low-fouling membranes. *J. Membr. Sci.* **2005,** *246*, 203-215.
27. Steen, M. L.; Kull, K. R.; Fisher, E. R., Comparison of surface interactions for NH and NH_2 radicals on polymer and metal substrates during NH_3 plasma processing. *J. Appl. Phys.* **2002,** *92*, 55-63.
28. Trenczek-Zajac, A.; Kowalski, K.; Zakrzewska, K.; Radecka, M., Nitrogen-doped titanium dioxide-Characterization of structural and optical properties. *Mater. Res. Bull.* **2009,** *44* (7), 1547-1552.
29. Pulsipher, D. J. V.; Fisher, E. R., O_2 plasma treatment of mesoporous and compact TiO_2 photovoltaic films: Revealing and eliminating effects of Si incorporation. *Surf. Coat. Technol.* **2009,** *203* (16), 2236-2242.
30. Hyett, G.; Green, M. A.; Parkin, I. P., The use of combinatorial chemical vapor deposition in the synthesis of Ti_3-delta O_4N with 0.06 < delta < 0.25: A titanium oxynitride phase lsostructural to anosovite. *J. Am. Chem. Soc.* **2007,** *129* (50), 15541-15548.

31. Liao, L. F.; Lien, C. F.; Shieh, D. L.; Chen, F. C.; Lin, J. L., FTIR study of adsorption and photochemistry of amide on powdered TiO_2: Comparison of benzamide with acetamide. *PCCP* **2002,** *4* (18), 4584-4589.
32. Beranek, R.; Kisch, H., Tuning the optical and photoelectrochemical properties of surface-modified TiO2. *Photochem. Photobiol. Sci.* **2008,** *7* (1), 40-48.
33. Tang, H.; Berger, H.; Schmid, P. E.; Levy, F.; Burri, G., Photoluminescence in TiO_2 Anatase Single-Crystals. *Solid State Commun.* **1993,** *87* (9), 847-850.
34. Sheng, Y. G.; Liang, L. P.; Xu, Y.; Wu, D.; Sun, Y. H., Low-temperature deposition of the high-performance anatase-titania optical films via a modified sol-gel route. *Opt. Mater.* **2008,** *30* (8), 1310-1315.
35. Mahalingam, S.; Edirisinghe, M. J., Characteristics of electrohydrodynamically prepared titanium dioxide films. *Appl. Phys. A* **2007,** *89* (4), 987-993.
36. Drygas, M.; Czosnek, C.; Paine, R. T.; Janik, J. F., Two-stage aerosol synthesis of titanium nitride TiN and titanium oxynitride TiO_xN_y nanopowders of spherical particle morphology. *Chem. Mater.* **2006,** *18* (13), 3122-3129.
37. Dong, F.; Zhao, W. R.; Wu, Z. B.; Guo, S., Band structure and visible light photocatalytic activity of multi-type nitrogen doped TiO_2 nanoparticles prepared by thermal decomposition. *J. Hazard. Mater.* **2009,** *162* (2-3), 763-770.
38. Jagadale, T. C.; Takale, S. P.; Sonawane, R. S.; Joshi, H. M.; Patil, S. I.; Kale, B. B.; Ogale, S. B., N-doped TiO_2 nanoparticle based visible light photocatalyst by modified peroxide sol-gel method. *J. Phys. Chem. C* **2008,** *112* (37), 14595-14602.
39. Qin, H. L.; Gu, G. B.; Liu, S., Preparation of nitrogen-doped titania with visible-light activity and its application. *C.R. Chim.* **2008,** *11* (1-2), 95-100.
40. Kitano, M.; Funatsu, K.; Matsuoka, M.; Ueshima, M.; Anpo, M., Preparation of nitrogen-substituted TiO_2 thin film photocatalysts by the radio frequency magnetron sputtering deposition method and their photocatalytic reactivity under visible light irradiation. *J. Phys. Chem. B* **2006,** *110* (50), 25266-25272.
41. Parida, K. M.; Naik, B., Synthesis of mesoporous $TiO_{2-x}N_x$ spheres by template free homogeneous co-precipitation method and their photo-catalytic activity under visible light illumination. *J. Coll. Interface Sci.* **2009,** *333* (1), 269-276.
42. Miyauchi, M.; Ikezawa, A.; Tobimatsu, H.; Irie, H.; Hashimoto, K., Zeta potential and photocatalytic activity of nitrogen doped TiO_2 thin films. *Physical Chemistry Chemical Physics* **2004,** *6* (4), 865-870.
43. Irie, H.; Watanabe, Y.; Hashimoto, K., Nitrogen-concentration dependence on photocatalytic activity of $TiO_{2-x}N_x$ powders. *J. Phys. Chem. B* **2003,** *107* (23), 5483-5486.
44. Song, X. M.; Gopireddy, D.; Takoudis, C. G., Characterization of titanium oxynitride films deposited by low pressure chemical vapor deposition using amide Ti precursor. *Thin Solid Films* **2008,** *516* (18), 6330-6335.
45. Zhang, Z.; Goodall, J. B. M.; Morgan, D. J.; Brown, S.; Clark, R. J. H.; Knowles, J. C.; Mordan, N. J.; Evans, J. R. G.; Carley, A. F.; Bowker, M.; Darr, J. A., Photocatalytic activities of N-doped nano-titanias and titanium nitride. *J. Eur. Ceram. Soc.* **2009,** *29* (11), 2343-2353.
46. Saha, N. C.; Tompkins, H. G., Titanium nitride oxidation chemistry - an X-ray photoelectron-spectroscopy study. *J. Appl. Phys.* **1992,** *72* (7), 3072-3079.

47. Glaser, A.; Surnev, S.; Netzer, F. P.; Fateh, N.; Fontalvo, G. A.; Mitterer, C., Oxidation of vanadium nitride and titanium nitride coatings. *Surf. Sci.* **2007,** *601* (4), 1153-1159.
48. Jung, M. J.; Nam, K. H.; Chung, Y. M.; Boo, J. H.; Han, J. G., The physiochemical properties of TiOxNy films with controlled oxygen partial pressure. *Surf. Coat. Technol.* **2003,** *171* (1-3), 71-74.
49. Chen, C.; Bai, H.; Chang, C., Effect of plasma processing gas composition on the nitrogen-doping status and visible light photocatalysis of TiO_2. *J. Phys. Chem. C* **2007,** *111* (42), 15228-15235.
50. Zorn, G.; Adadi, R.; Brener, R.; Yakoviev, V. A.; Gotman, I.; Gutmanas, E. Y.; Sukenik, C. N., Tailoring the surface of NiTi alloy using pirac nitriding followed by anodization and phosphonate monolayer deposition. *Chem. Mater.* **2008,** *20* (16), 5368-5374.
51. Burrow, B. J.; Morgan, A. E.; Ellwanger, R. C., A correlation of auger-electron spectroscopy, X-ray photoelectron-spectroscopy, and rutherford backscattering spectrometry measurements on sputter-deposited titanium nitride thin-films. *J. Vac. Sci. Technol., A* **1986,** *4* (6), 2463-2469.
52. Kuznetsov, M. V.; Zhuravlev, M. V.; Shalayeva, E. V.; Gubanov, V. A., Influence of the deposition parameters on the composition, structure and X-Ray photoelectron-spectroscopy spectra of Ti-N films. *Thin Solid Films* **1992,** *215* (1), 1-7.
53. Kim, Y.; Yoo, B. J.; Vittal, R.; Lee, Y.; Park, N. G.; Kim, K. J., Low-temperature oxygen plasma treatment of TiO_2 film for enhanced performance of dye-sensitized solar cells. *J. Power Sources* **2008,** *175* (2), 914-919.
54. Takahashi, I.; Payne, D. J.; Palgrave, R. G.; Egdell, R. G., High resolution X-ray photoemission study of nitrogen doped TiO_2 rutile single crystals. *Chem. Phys. Lett.* **2008,** *454* (4-6), 314-317.
55. Chae, Y. K.; Mori, S.; Suzuki, M., Visible-light photocatalytic activity of anatase TiO_2 treated with argon plasma. *Thin Solid Films* **2009,** *517*, 4260-4263.
56. Liu, H.; Ma, H. T.; Li, X. Z.; Li, W. Z.; Wu, M.; Bao, X. H., The enhancement of TiO_2 photocatalytic activity by hydrogen thermal treatment. *Chemosphere* **2003,** *50* (1), 39-46.
57. Miyaoka, H.; Mizutani, G.; Sano, H.; Omote, M.; Nakatsuji, K.; Komori, F., Anomalous electro-migration of oxygen vacancies in reduced TiO_2. *Solid State Commun.* **2002,** *123* (9), 399-404.
58. Bullock, E. L.; Patthey, L.; Steinemann, S. G., Clean and hydroxylated rutile TiO_2(110) surfaces studied by X-ray photoelectron spectroscopy. *Surf. Sci.* **1996,** *352*, 504-510.
59. Cao, Y.; Yang, W. S.; Chen, Y. M.; Du, H.; Yue, P., Effect of chemisorbed surface species on the photocatalytic activity of TiO_2 nanoparticulate films. *Appl. Surf. Sci.* **2004,** *236* (1-4), 223-230.
60. Napoli, F.; Chiesa, M.; Livraghi, S.; Giamello, E.; Agnoli, S.; Granozzi, G.; Pacchioni, G.; Di Valentin, C., The nitrogen photoactive centre in N-doped titanium dioxide formed via interaction of N atoms with the solid. Nature and energy level of the species. *Chem. Phys. Lett.* **2009,** *477* (1-3), 135-138.

61. Peng, F.; Cai, L. F.; Huang, L.; Yu, H.; Wang, H. J., Preparation of nitrogen-doped titanium dioxide with visible-light photocatalytic activity using a facile hydrothermal method. *J. Phys. Chem. Solids* **2008,** *69* (7), 1657-1664.
62. Diwald, O.; Thompson, T. L.; Zubkov, T.; Goralski, E. G.; Walck, S. D.; Yates, J. T., Photochemical activity of nitrogen-doped rutile $TiO_2(111)$ in visible light. *J. Phys. Chem. B* **2004,** *108* (19), 6004-6008.
63. Livraghi, S.; Chierotti, M. R.; Giamello, E.; Magnacca, G.; Paganini, M. C.; Cappelletti, G.; Bianchi, C. L., Nitrogen-doped titanium dioxide active in photocatalytic reactions with visible light: A multi-technique characterization of differently prepared materials. *J. Phys. Chem. C* **2008,** *112* (44), 17244-17252.
64. Chen, D. M.; Jiang, Z. Y.; Geng, J. Q.; Wang, Q.; Yang, D., Carbon and nitrogen co-doped TiO_2 with enhanced visible-light photocatalytic activity. *Ind. Eng. Chem. Res.* **2007,** *46* (9), 2741-2746.
65. Chen, C. C.; Bai, H. L.; Chang, S. M.; Chang, C. L.; Den, W., Preparation of N-doped TiO_2 photocatalyst by atmospheric pressure plasma process for VOCs decomposition under UV and visible light sources. *J. Nanopart. Res.* **2007,** *9* (3), 365-375.
66. Parida, K. M.; Naik, B., Synthesis of mesoporous $TiO_{2-x}N_x$ spheres by template free homogeneous co-precipitation method and their photo-catalytic activity under visible light illumination. *J. Colloid Interface Sci.* **2009,** *333* (1), 269-276.
67. Shinn, N. D.; Tsang, K. L., Strain-induced surface reactivity - low-temperature Cr/W(110) nitridation. *J. Vac. Sci. Technol., A* **1991,** *9* (3), 1558-1562.
68. Milosev, I.; Strehblow, H. H.; Navinsek, B.; Metikoshukovic, M., Electrochemical and thermal-oxidation of tin coatings studied by XPS. *Surf. Interface Anal.* **1995,** *23* (7-8), 529-539.
69. Nassau, K., *The Physics and Chemistry of Color: The Fifteen Causes of Color*. John Wiley & Sons, Inc.: New York, 2001; p 173-176.
70. Li, M.; Hebenstreit, W.; Diebold, U.; Tyryshkin, A. M.; Bowman, M. K.; Dunham, G. G.; Henderson, M. A., The influence of the bulk reduction state on the surface structure and morphology of rutile $TiO_2(110)$ single crystals. *J. Phys. Chem. B* **2000,** *104* (20), 4944-4950.
71. Bendavid, A.; Martin, P. J.; Netterfield, R. P.; Kinder, T. J., Characterization of the optical properties and composition of TiN_x thin films by spectroscopic ellipsometry and X-ray photoelectron spectroscopy. *Surf. Interface Anal.* **1996,** *24* (9), 627-633.
72. Zhou, Q. G.; Bai, X. D.; Xue, X. Y.; Ling, Y. H.; Chen, X. W.; Xu, J.; Wang, D. R., Colorimetric properties of TiN coating implanted by aluminum. *J. Alloys Compd.* **2005,** *391* (1-2), 141-145.
73. Logothetidis, S.; Alexandrou, I.; Papadopoulos, A., In-situ spectroscopic ellipsometry to monitor the process of TiN_x thin-films deposited by reactive sputtering. *J. Appl. Phys.* **1995,** *77* (3), 1043-1047.
74. Roquiny, P.; Bodart, F.; Terwagne, G., Colour control of titanium nitride coatings produced by reactive magnetron sputtering at temperature less than 100 degrees C. *Surf. Coat. Technol.* **1999,** *116*, 278-283.

CHAPTER 5

EXAMINING PRELIMINARY PHOTOCATALYTIC AND PHOTOVOTAIC DEVICES OF PLASM TREATED TiO_2

This chapter illustrates unpublished work in examine the effects of plasma treated TiO_2 materials for both photocatalytic and photovoltaic devices. This work was initiated to more fully understand the changes induced in the TiO_2 materials by the plasma treatments, including performance in their intended uses. Changes in device performance are explained by changes in surface chemistry and surface states. Some of the data presented in this Chapter were collected by fellow graduate student Ms. Erin Stuckert and Mr. William Richardson, an undergraduate researcher.

5.1 Introduction

TiO_2 behaves as a robust photocatalyst in degrading organic pollutants and dyes that adhere to it. Many studies have focused on making TiO_2 a better photocatalyst by sensitizing it to visible light via doping, surface attachment of a lower bandgap dye or material, or addition of cocatalysts.[1, 2] All of these studies have demonstrated positive results, to varying degrees. With doping, nitrogen-doped TiO_2 ($N:TiO_2$) materials have shown promise in using visible light to decompose organic compounds.[3-9] Notably, nitrogen can exist in multiple binding environments within the TiO_2 matrix and it is still unclear which N environments are responsible for the improvement in performance.

Moreover, many reports on visible light photocatalytic activity of N:TiO_2 materials fail to compare changes in ultraviolet (UV) photocatalytic activity.[1, 2] The photocatalytic response of plasma treated TiO_2 materials under both UV and visible light will aid both the creation of a better photocatalyst and the characterization of plasma processed TiO_2 materials.

TiO_2 is also an important component in dye sensitized solar cells (DSSCs) wherein it is a wide bandgap electron acceptor. An absorbed dye or sensitizer can inject electrons into the TiO_2 to quickly separate electron hole pairs (ehps) before they can recombine. One drawback to DSSCs is the slow electron transport over the mesoporous TiO_2 network.[10] The long and random network of sintered TiO_2 nanoparticles found in the most efficient DSSCs requires milliseconds of electron travel time to reach the back contact.[11] One way to address this problem is to plasma treat TiO_2 to alter the type and amount of surface trap states. These trap states are a source of ongoing controversy as there is debate over their relative importance in electron transport through the nanoparticle network.[12, 13] The effects of nitrogen plasma treatments on TiO_2 photoanodes in complete DSSCs can be examined by analyzing efficiency (η), short-circuit current (I_{sc}), open-circuit voltage (V_{oc}), fill factor (FF), and incident photo to current conversion efficiencies ($IPCE$) values that come from the following equations:[14]

$$\eta = \frac{P_{\max}}{P_{in}} = \frac{V_{oc} I_{sc} FF}{P_{in}} \quad (5.1)$$

$$FF = \frac{V_{MP} I_{MP}}{V_{oc} I_{sc}} \quad (5.2)$$

$$IPCE = \frac{1240 \cdot I_{sc}}{\lambda_{nm} P_{in}} \quad (5.3)$$

where P_{max} is the maximum output power, P_{in} is the total input power, V_{MP} and I_{MP} are the voltage and current at the maximum power, respectively, and λ_{nm} is the wavelength of incident light in nanometers.

Here, we examine the photocatalytic and photovoltaic activity of a range of plasma treated TiO_2 materials. We have chosen to measure photocatalytic activity via rhodamine B (RhB) dye decomposition on prepared nitrogen doped and silicon implanted P25 TiO_2 photocatalysts in water. Solaronix mesoporous TiO_2 photoanodes are modified with ammonia, nitrogen, and urea plasma treatments and tested in complete DSSCs.

5.2 Results

Photocatalytic results. Figure 5.1 denotes the change in the measured UV-Vis spectrum of RhB as a function of light irradiation time for unmodified P25 powder at 30ºC. The main peak at552 nm diminishes at a rate corresponding to a pseudo first order reaction. Note that for all powders tested, the wavelength at the maximum signal (λ_{max}) of the peak shifts slightly toward the shoulder peak as the dye decomposes. This contributes to the larger error observed for data taken at longer time intervals. Data are shown for as received P25 powder and an NH_3/NH_3 treated powder to compare relative shoulder peak intensities.

The data in Figure 5.2 depict the activity of P25 powder decomposing RhB dye at different solution temperatures. Rate constants of $1.8 \pm 0.2 \times 10^{-3} \pm 0.2 \times 10^{-3}$, $3.0 \pm 0.1 \times 10^{-3}$, and $3.5 \pm 0.5 \times 10^{-3}$ were determined from the first four points in Figure 5.2 with solution temperatures of 5, 20, 30, and 40 ºC, respectively.

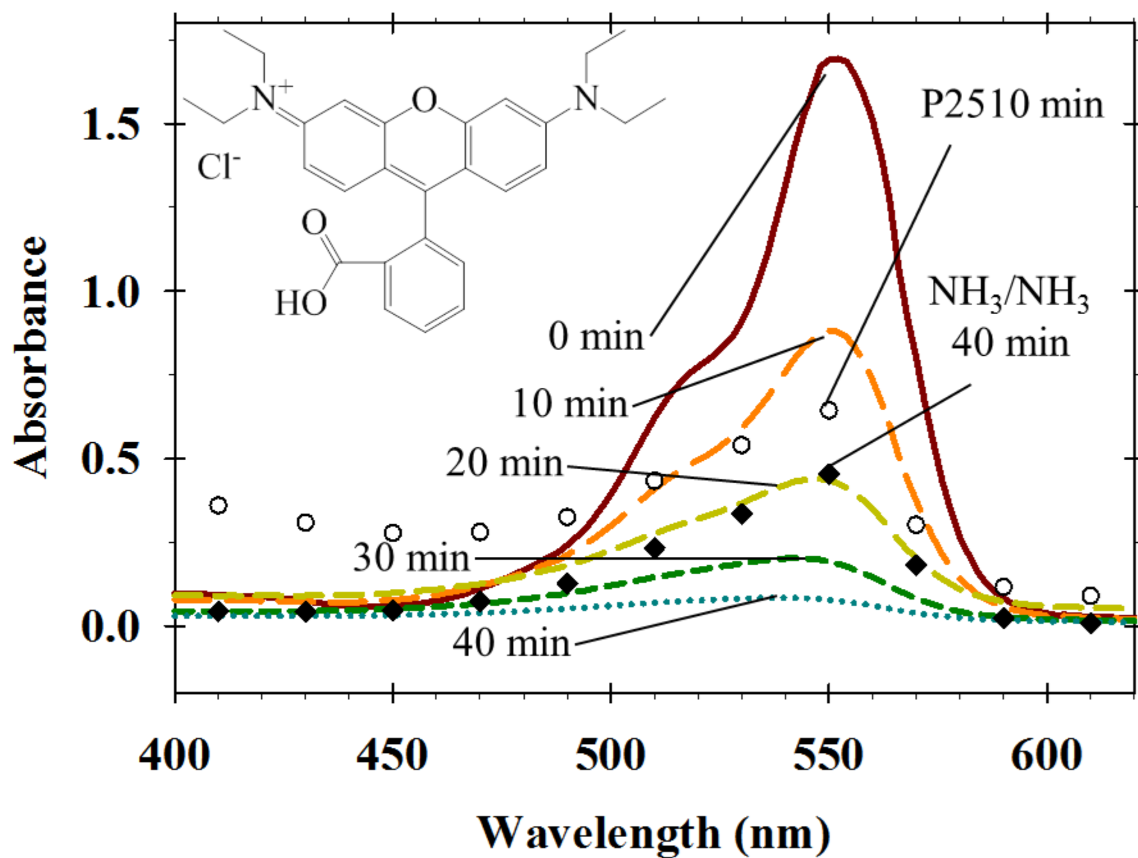

Figure 5.1. UV-vis absorbance spectra for the decomposition of RhB at different irradiation times using P25s (lines), as received P25 (open circles), and NH_3/NH_3 treated powders (diamonds).

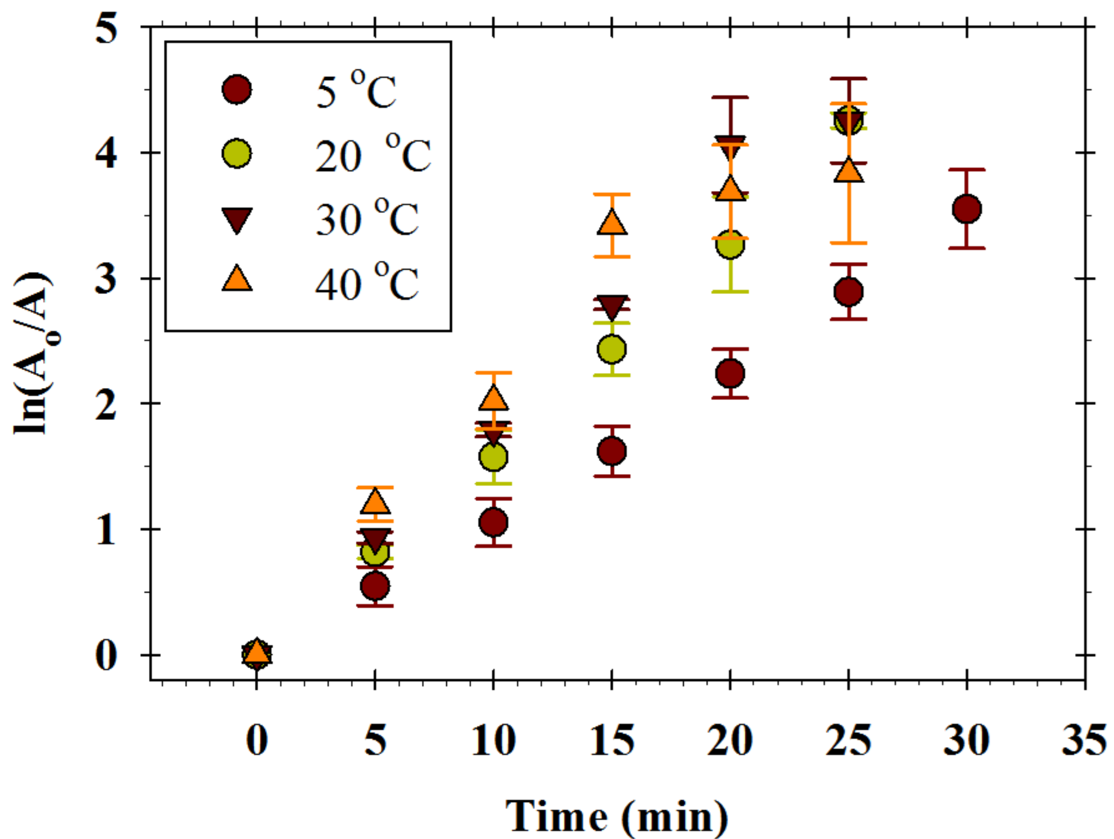

Figure 5.2. Comparison of the photocatalytic behavior of as received P25 using different solution temperatures.

Slight differences are observed in the four measured temperatures, with points overlapping at both low and high times because of data normalization and the dye approaching complete decomposition, respectively. The data show an apparent temperature dependence for RhB decomposition, yielding an activation energy of 14 ± 2 kJ/mole.

To compare plasma modified P25 with unmodified P25, particles were cast into mesoporous films that could be easily plasma modified. With mesoporous films, the amount and depth of the plasma modification were more controllable. SEM micrographs for both the P25 and P25s samples, Figure 5.3 show particles with 36 ± 13 nm and 38 ± 9 nm diameters, respectively. Although there was no observable difference in particle size, sintering the P25 powder into films decreases photocatalytic performance as demonstrated by the difference between bare P25 and P25s samples shown in Figures 5.2 and 5.4, respectively. The particles clump together and the variation in particle agglomeration can be seen in comparing Figures 5.3a and 5.3b. From the SEM micrographs, it is unclear if the particles are sintered together or simply electrostatically attracted, but the size of the agglomerates have changed whereas the size of the individual particles were not affected. Notably, this could cause the diminished photocatalytic activity in sintered P25 powders. Thus, we focus here on understanding results of the plasma treatment as opposed to achieving maximum photocatalytic performance.

The majority of the results found for the photocatalytic activity of P25 films treated with a range of nitrogen-containing plasma are summarized in Figure 5.4. For comparison, XPS elemental analysis data are shown in Table 5.1.

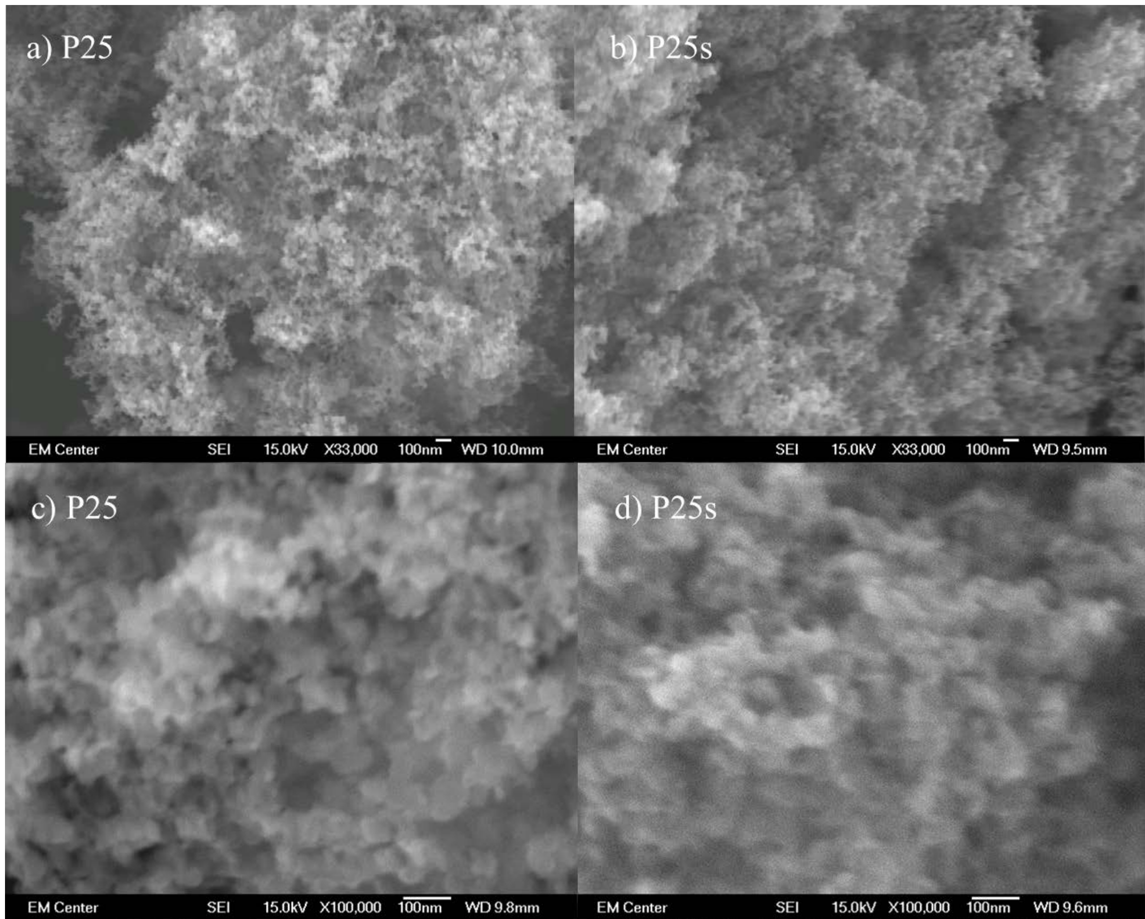

Figure 5.3. SEM micrographs of as received P25 powders and P25s powders at 33,000 and 100,000 magnification.

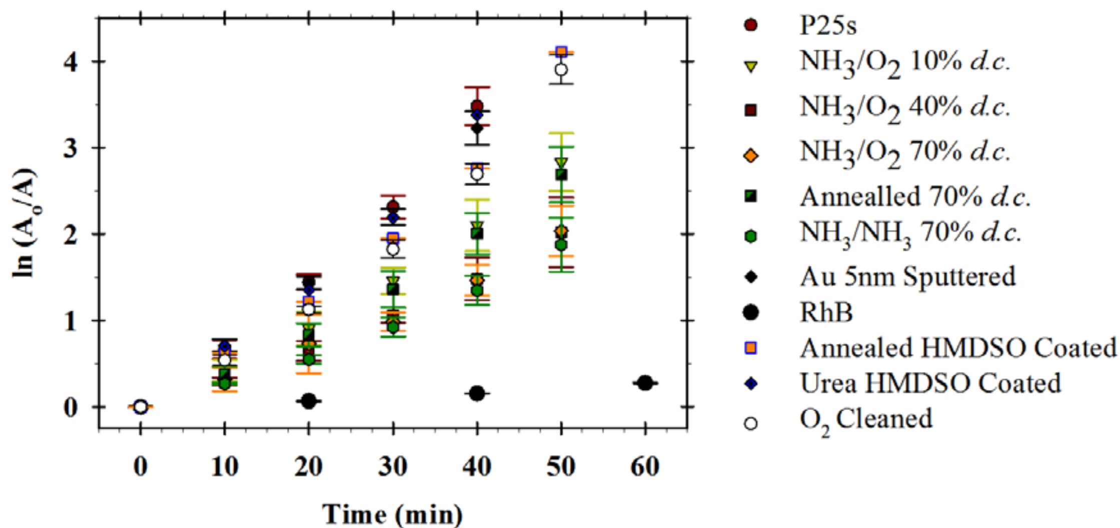

Figure 5.4. Comparison of the photocatalytic behavior of TiO_2 powders deposited into films and treated using different nitrogen-implanting plasma treatments. All films were subjected to an O_2 plasma "cleaning" step prior to treatment. Data from O_2 cleaned films are shown along with untreated P25s, and pure RhB decomposition data for reference.

Table 5.1. XPS composition of NH_3 plasma treated samples.

Sample Treatment	C	O	Ti	N	N/Ti
P25s	25.5 ± 1.8	53.2 ± 1.8	19.8 ± 0.3	0.8 ± 0.9	--
NH_3/O_2 10% *d.c.*	5.5 ± 1.8	60.3 ± 1.7	29.7 ± 0.5	4.4 ± 0.7	0.13 ± 0.02
NH_3/O_2 40% *d.c.*	8.3 ± 2.5	48.8 ± 1.1	30.7 ± 1.4	12.2 ± 0.5	0.39 ± 0.02
NH_3/O_2 70% *d.c.*	13.1 ± 1.7	45.5 ± 1.0	27.2 ± 2.6	13.2 ± 1.4	0.46 ± 0.04
$NH_3/NH_3$70% *d.c.*	7.2 ± 1.7	40.3 ± 1.6	31.9 ± 0.9	20.7 ± 1.7	0.64 ± 0.07
NH_3/NH_3 Annealed	2.6 ± 0.6	62.0 ± 0.4	28.9 ± 0.9	6.6 ± 1.0	0.23 ± 0.04
O_2 Cleaned	4.5 ± 0.8	65.5 ± 1.7	26.7 ± 3.0	--	--

The primary XPS N 1s binding environment in the NH_3/O_2 films at 396.3 ± 0.2 eV is assigned to substitutional nitrogen, $N(-TiO_5)_3$, or $N(-TiO_5)_2(-TiO_4N)_1$ species.[15] As the *d.c.* decreases, the amount of incorporated substitutional nitrogen increases to a maximum according to an exponential rise equation, yielding an R^2 value of 0.97, Figure 5.5a. Films modified with NH_3/O_2 treatments employing either 70% or 40% *d.c.* NH_3 plasmas had similar photocatalytic activity. Using a 10% *d.c.* plasma, however, resulted in better photocatalytic activity. NH_3/NH_3 treated powders contain more defects and an additional XPS N 1s binding environment (397.2 ± 0.2 eV), displayed the same photocatalytic activity as the NH_3/O_2 70% *d.c.* modified powders. After annealing NH_3/NH_3 films at 450 ºC for 45 min, most of the nitrogen shifts to the 402.4 ± 0.2 eV binding environment and the photocatalytic activity of the powder resulting from these films is comparable to NH_3/O_2 10% *d.c.* modified powders. Because of the solubility of the functionalization imposed by urea plasma treatments, they were coated with SiO_2 using a 90:10 O_2:HMDSO plasma. The resulting powder had unaltered photocatalytic performance.[15] All nitrogen doped films were first pretreated with an oxygen plasma, ostensibly to “clean” the materials prior to NH_3 plasma treatment.[16] The photocatalytic activity of powders cleaned in this manner clearly indicates that oxygen cleaning alone decreases the photocatalytic performance of the TiO_2 powders. Other schemes for improving relative photocatalytic activity (e.g. sputtering 2-5 nm of Au onto the TiO_2 surface) were explored, but notably did not alter the performance of the powders in UV or UV filtered experiments, even though the films appearance changed slightly (appearing slightly purple).

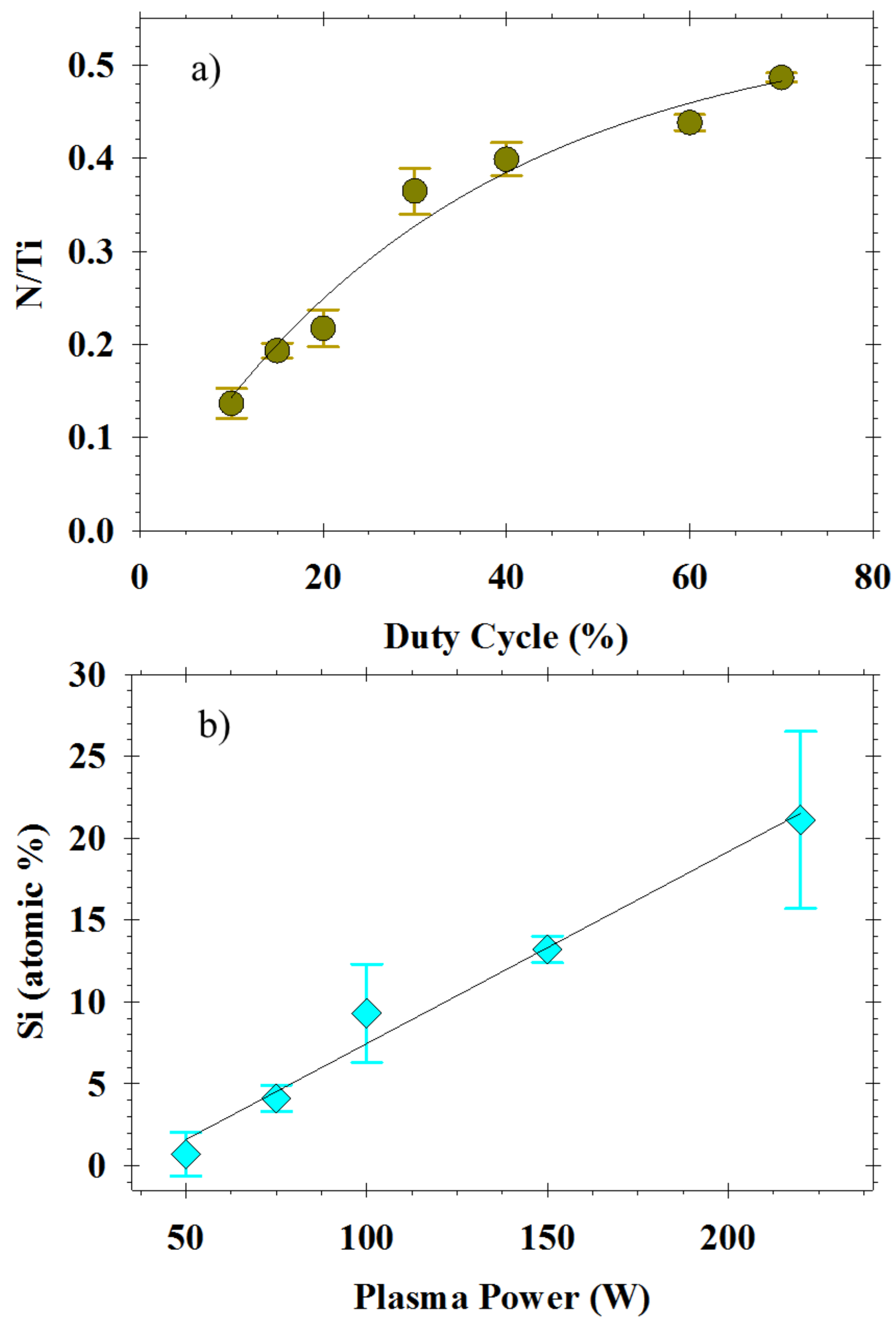

Figure 5.5. Relationship between a) N/Ti ratio and plasma *d.c.* and b) atomic percent Si and *P*.

We used two different plasma-based methods to incorporate silicon into TiO_2 films: (1) O_2 plasma sputter deposited SiO_2 etched from the glass reactor, and (2) HMDSO:O_2 (10:90) plasma deposited SiO_2 coatings. In the first method, as the CW power of the O_2 plasma increases, the silicon content of the treated TiO_2 films also increase as shown in Table 5.2 and Figure 5.5b. Figure 5.6 shows photocatalytic activity results obtained from these materials. The films with $0.7 \pm 1.3\%$ silicon content had lower photocatalytic performance, whereas films with $4.1 \pm 0.8\%$ and $21.1 \pm 5.4\%$ silicon content had similar photocatalytic activity. Likewise, films treated in the HMDSO plasmas resulted in photocatalytic activity equivalent to unmodified P25. When the HMDSO plasma treatment was used to coat the “annealed” films, the performance of the annealed films improved.

Results from visible light experiments were closely clustered, Figure 5.7. The performance of P25s powders resulted in better photocatalytic activity than all treatments, with the exception of powders with high sputter-deposited silicon content. The photocatalytic activity of the HMDSO treated powders is less than the control experiment of RhB irradiated with visible light.

Photovoltaic results. Figure 5.8 shows results from preliminary photovoltaic data collected while using nitrogen doped photoanodes. Error bars represent one standard deviation of the maximum values for at least three separate DSSCs. Many of the error bars overlap due to the variability in measurements from cell to cell, but the maximum values can be used to qualitatively compare photoanode treatments, assuming that the variability in a particular plasma treatment is small compared to the other variables that change from cell to cell.

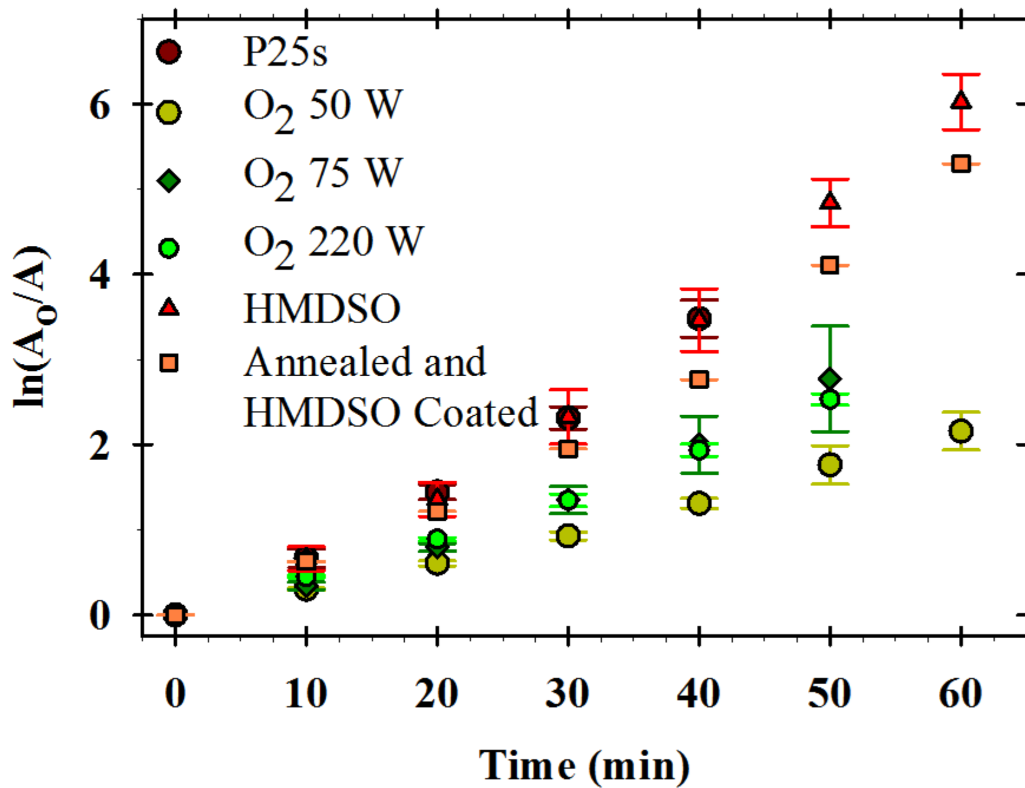

Figure 5.6. Comparison of the photocatalytic behavior of TiO_2 films with SiO_2 incorporated using O_2 plasmas at three different rf powers, an O_2:HMDSO (90:10) plasma, and annealed films that were sequentially treated with HMDSO. P25s films are displayed for comparison.

Table 5.2. XPS composition of O_2 and HMDSO plasma treated samples.

Sample Treatment	C	O	Ti	Si	Si/Ti
50 W CW O_2	12.8 ± 1.0	59.5 ± 3.0	27.0 ± 4.0	0.7 ± 1.3	--
75 W CW O_2	1.3 ± 0.4	67.9 ± 0.1	26.7 ± 0.5	4.1 ± 0.8	0.15 ± 0.03
100 W CW O_2	0.6 ± 0.5	68.9 ± 0.3	21.2 ± 3.2	9.3 ± 3.0	0.44 ± 0.21
150 W CW O_2	0.8 ± 0.5	68.9 ± 0.6	17.1 ± 0.8	13.2 ± 0.8	0.77 ± 0.08
220 W CW O_2	1.5 ± 1.5	67.2 ± 1.4	10.1 ± 4.9	21.1 ± 5.4	2.09 ± 0.65
HMDSO:O_2	3.25 2.18	68.4 ± 2.3	19.1 ± 6.3	10.2 ± 6.0	0.62 ± 0.56

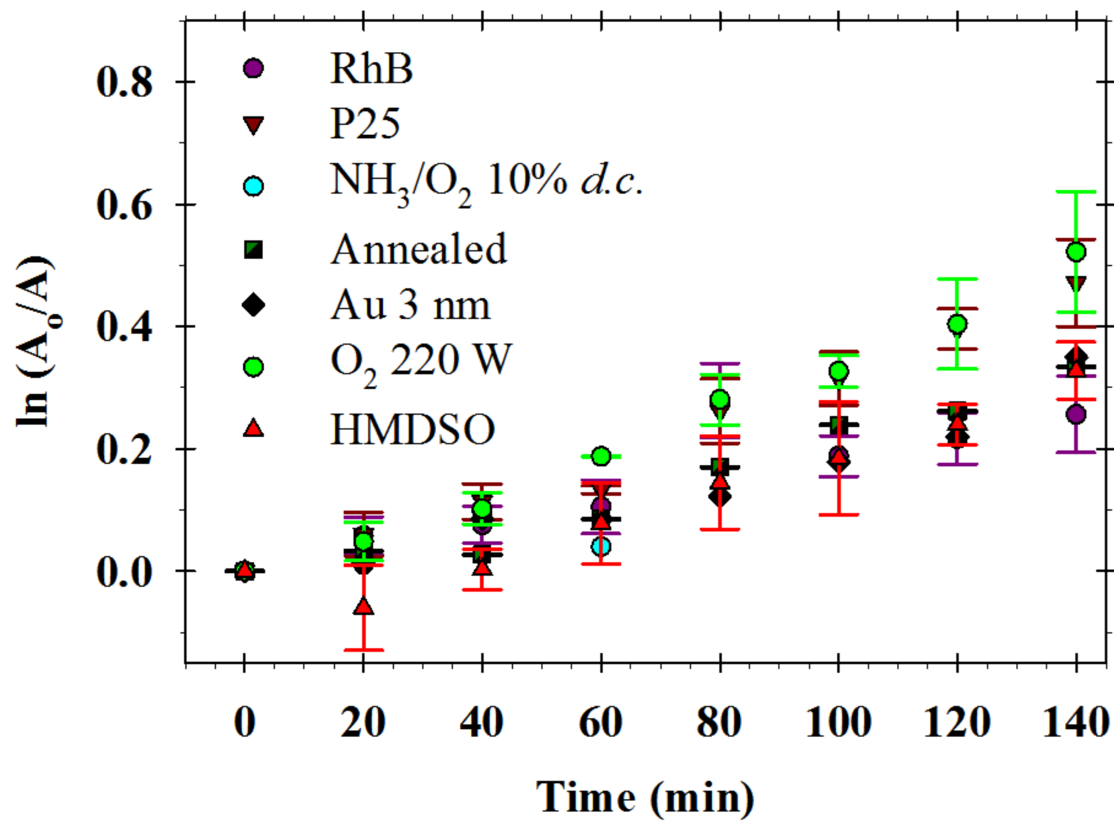

Figure 5.7. Comparison of the photocatalytic behavior of TiO_2 films under visible light irradiation. P25 and RhB data are given for reference.

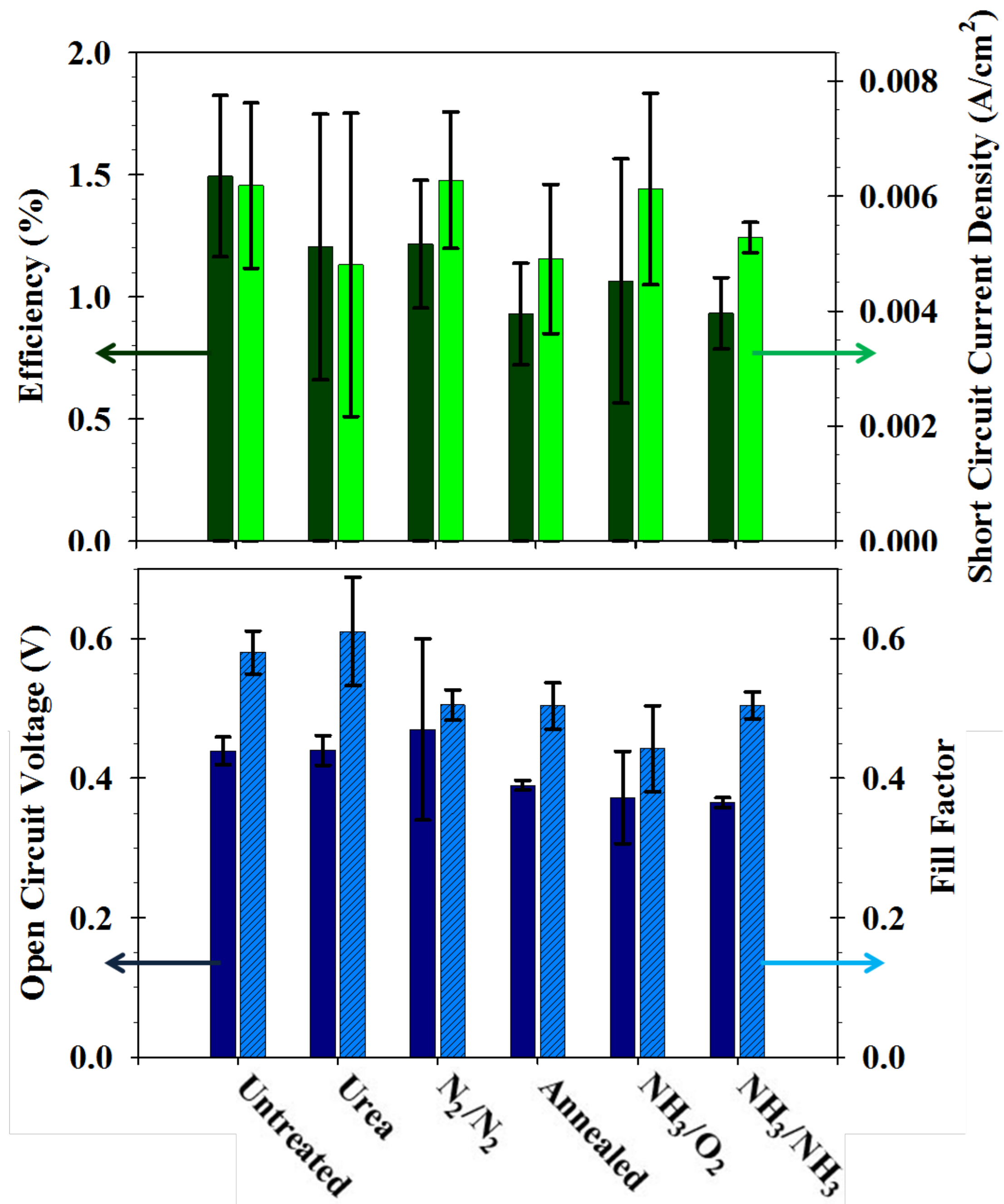

Figure 5.8. a) η_{eff} and J_{sc} values and b) V_{oc} and FF values collected from completed DSSCs using photoanodes modified by the plasma treatments listed.

The maximum efficiency measured was for untreated Solaronix films followed closely by urea treated films, Figure 5.8a. The maximum current density was for the NH_3/O_2 treated cell. From Figure 5.8b, the maximum V_{oc} and FF values were obtained by N_2/N_2 and urea treated films, respectively. Figure 5.9 contains *IPCE* data for the different plasma photoanode treatments and both annealed and NH_3/O_2 treated films convert significantly more light to current at wavelengths longer than ~600 nm. Figure 5.10 shows voltage transients of films after being exposed to 1s of white light. The decay time in potential gives insights into the amount of charge that is trapped in these cells. Note that NH_3/O_2 treated cells have the largest decay time.

5.3 Discussion

One overarching goal of this work was to ascertain the effects of various plasma treatments on the photocatalytic behavior of P25and the photovoltaic behavior of Solaronix TiO_2 films. These experiments are not yet completed, but a summary of the work done to date and some possible explanations are given for the behavior of the devices tested thus far.

Photocatalytic activity. A shift in λ_{max} that occurs in RhB photocatalytic degradation reactions is a result of a multistep decomposition. Initially, a deethylation process occurs and this accounts for faster initial decomposition of the 552 nm peak.

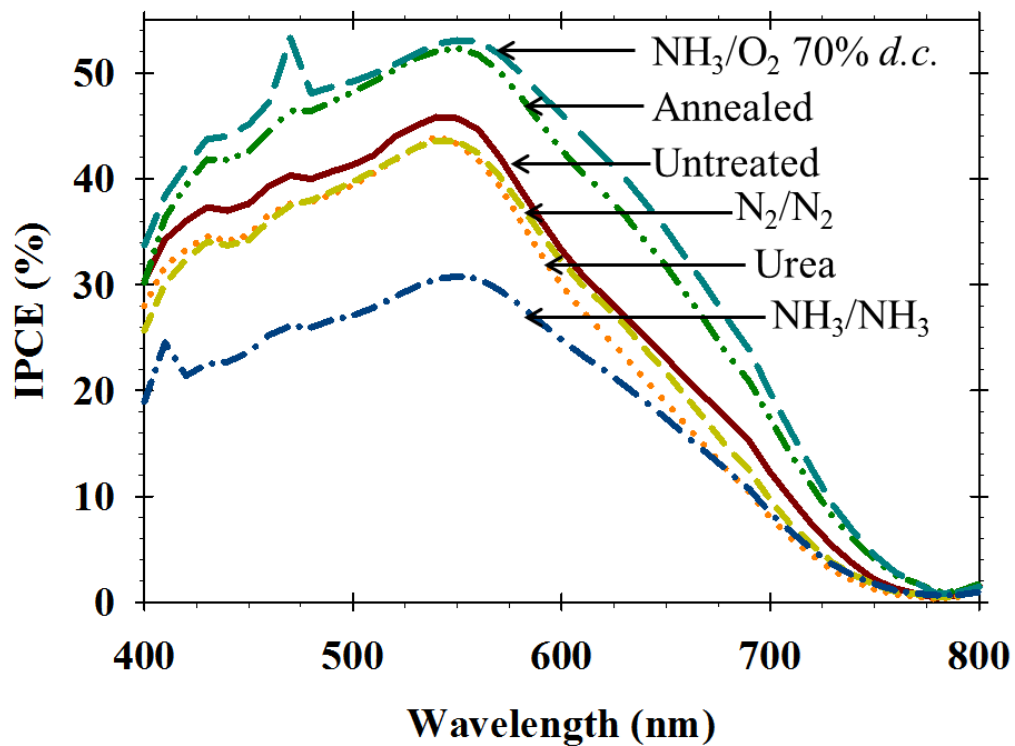

Figure 5.9. *IPCE* curves collected as a function of wavelength from completed DSSCs using photoanodes modified by the plasma treatments listed.

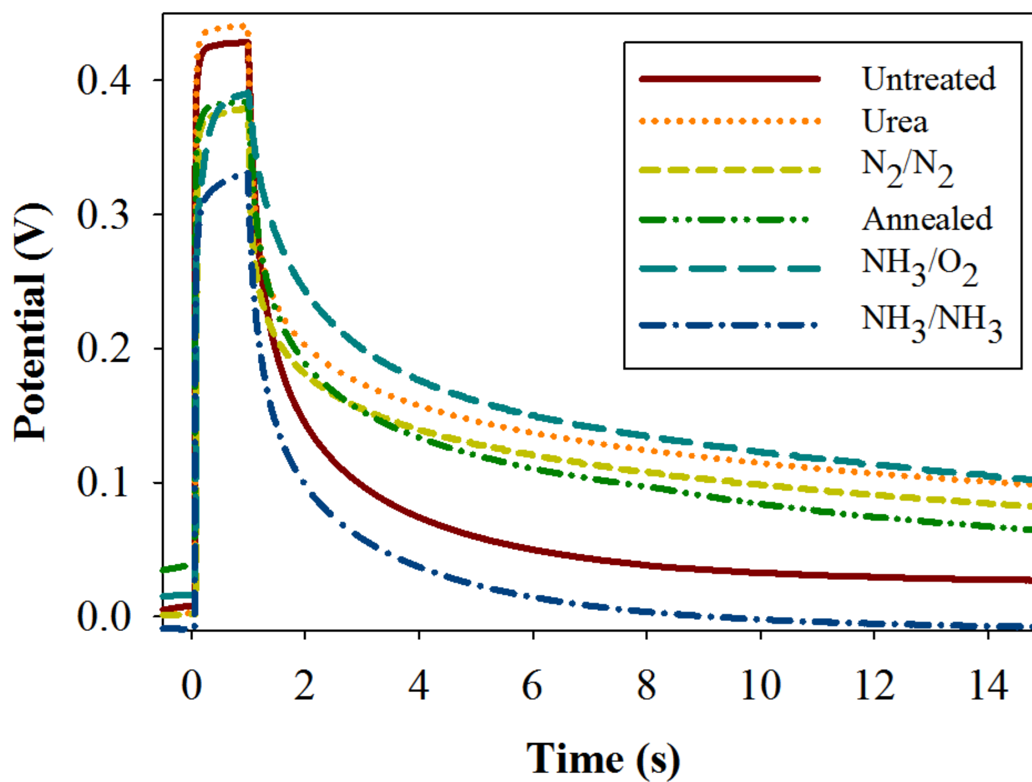

Figure 5.10. Voltage transient curves collected as a function of time from completed DSSCs using photoanodes modified by the plasma treatments listed.

Zhuang et al. observed a relatively large hypsochromic shift for both their unaltered TiO_2 films and films with buried interfacial defects, suggesting that these undamaged surfaces favor deethylation of RhB.[17] Comparatively little deethylation of RhB was observed on films with exposed surface defects induced by a helium plasma. The as received P25 trace in Figure 5.1 has a higher relative shoulder peak intensity than other materials, indicating that these powders have fewer surface defects than the scraped P25 (P25s) powders. The trace of an NH_3/NH_3 treated powder shows the insignificant difference in the shoulder peak between P25s powder and a treated powder with significant defects. The small hypsochromic shift in RhB decomposition observed for all treatments should be indicative of defect-filled surfaces, but very little difference is seen between P25s powders with few defects and NH_3/NH_3 powders with significant levels of defects. Compared to the results of Zhuang et al. who used pure anatase films, the P25 powders behave as though they have defects. This could be a result of the crystalline mixture (~80% anatase and ~20% rutile)[18] of P25. The decreased relative shoulder peak height of the P25s and NH_3/NH_3 treated powders compared to the P25 powders is indicative of increased defects and could be due to breaking apart the porous sintered network of particles. Yet the difference in relative shoulder peak height between untreated and treated powders is insignificant. This could arise from incomplete modification of the mesoporous films as the plasma only modifies surfaces it comes into contact with, so all powdered samples have some untreated areas as the particles are not rotated or stirred during the treatment, but fixed in a porous film.

The activation energy associated with this photocatalytic reaction (14 ± 2 kJ/mole) arises from the adsorption and desorption of the reactant and products of dye

decomposition occurring at the TiO_2 surface.[19] As the temperature of the solution rises, the decomposition reaction has more energy to proceed and the flux of reactant and products on and off of the TiO_2 surface increases. The rate of charge recombination is also affected by temperature, but to a lesser degree at the small temperature range monitored. The decrease in photocatalytic activity of P25 after it has been sintered into films can be at least partially explained by a change in agglomeration size or surface area. The increase in agglomerate size reduces surface sites and accesses to surface sites available for absorption. Slight changes in defect states (oxygen vacancies) from breaking up the mesoporous network and small changes in crystallinity could also contribute to the sintered powders poor performance.

From the treatments examined thus far, the 396 and 397 eV XPS binding environments of nitrogen found in these treated films does not help the visible or UV light photocatalytic activity of TiO_2. The major nitrogen binding environment associated with the annealed films (at 402 eV) performs better possibly because the 396 and 397 eV nitrogen binding environments have been reduced. Nitrogen in these binding environments could be causing recombination centers that severely reduce the creation of surface hydroxyl radicals. This same line of thinking could be applied to understand why NH_3/O_2 10% *d.c.* treated powders perform better than NH_3/O_2 70% *d.c.* treated powders. Namely, this is because the former have a small amount of nitrogen at the 396 eV N 1s binding environment. The change in surface charge of the powders after implanting nitrogen groups into the TiO_2 probably alters how the dye absorbs to the catalyst to lower its photocatalytic activity, but no direct quantification of this has been performed yet with rhodamine dyes.[20] The nitrogen associated with either the 398 or 400 eV XPS peaks

could be the photocatalytically active nitrogen dopant that explains the improvements seen in other nitrogen doped TiO_2 photocatalysts. Urea plasma treatments were the only modification that lead to nitrogen incorporation into the 400 eV N 1s peak, which was somewhat soluble in water.[15] To protect this nitrogen environment, the urea treated films were subsequently coated with SiO_2 using an HMDSO plasma and these powders performed similar to plain HMDSO coated powders. A water-insoluble 400 eV N 1s binding environment has not yet been tried in this work.

Others have reported the increased photocatalytic activity of TiO_2 coated or coupled with plasmonically active Au nanoparticles.[21, 22] The gold either helps prevent ehp recombination by separating charges or helps light absorption by transferring plasmonic energy to a connected TiO_2 particle. The color of the film changes to a faint purple when a thin film (2-5 nm) of gold is sputtered onto the mesoporous TiO_2, so the gold is absorbing light. The unaltered photocatalytic activity of gold coated films shows that through this method of gold deposition, the particles are not helped by transferring charge or plasmonic energy to the gold.

Previous reports have suggested incorporating silica into TiO_2 improves photocatalytic activity.[23-25] Here, we found there is a difference between sputter deposited and surface polymerized silica, with the former being more implanted into the TiO_2 when compared to the HMDSO deposited SiO_2 layer.[16] The 50 W CW O_2 plasma treatment results in substantial degradation of photocatalytic performance, and there is little to no silicon incorporation in these films (0.7 ± 1.3). This along with the lower performance of O_2 cleaned samples suggests that perhaps pure oxygen plasmas not only clean the surface from carbon contamination, but also fill potential reactive sites (oxygen

vacancies) on the TiO_2 surface. The degrading effects of the oxygen plasma are to some degree negated by the increased silicon content of 4.1 ± 0.8% or 21.1 ± 5.4%, but overall photocatalytic performance is worse. A $Ti_xSi_yO_{2x+2y}$ surface could be less effective at concentrating hydroxyl groups near photocatalytically active TiO_2 sites than a more SiO_2 like coating found in the HMDSO treated samples. The similarity in photocatalytic activity between the 75 W and 220 W O_2 plasma treated films shows that the amount of incorporated silicon is less important than the surface coverage of the incorporated silicon.

The observation that the value of $\ln(A_o/A)$ initially drops for HMDSO treated powders demonstrates that RhB dye absorbs to P25 coated HMDSO surfaces better and that some of this dye is released as the P25 is irradiated. Generally all the film treatments do not create powders that exhibit significant visible light decomposition of RhB. The nitrogen modified powders are worse than P25 powders possibly because they do not create ehps of enough energy to create hydroxyl radicals and decompose the dye.

Photovoltaic behavior. The DSSC characterizations help us learn about how the films treatments affect charge transport across the cells. The maximum η_{eff}, J_{sc}, V_{oc}, and *FF* values for urea treated films are very similar to untreated films. Yet there is much more error associated with the former films because the surface absorbed functionalization induced by the urea plasma treatments could be quite labile and dissolve in the γ-butyrolactone solvent. Future experimentation should explore this hypothesis. The higher J_{sc} and *IPCE* values of NH_3/O_2 treated films signify that these films transport more electrons than the other films and the high voltage decay time, Figure 5.10, signifies there are deeper or more trap states. The increase in trap states along with the increase in

light absorption could account for the increase in the max J_{sc} for NH_3/O_2 treated films, but their V_{oc} and FF values are lower than untreated films. N_2/N_2 treated films give rise to the same N 1s binding environment as NH_3/O_2 treated films, but there is less nitrogen implanted into these films (see Table 4.2), and there is no hydrogen involved in the treatments. The N_2/N_2 treated films could have higher V_{oc} and FF values because it has lower nitrogen content, but some difference between the two treatments allows higher *IPCE* and J_{sc} values in the NH_3/O_2 treated films. More DSSC experiments should be performed on the NH_3/O_2 films treated at lower *d.c.* values (Figure 5.5a) to increase V_{oc} and FF values while still allowing for higher J_{sc} values.

The lower η_{eff}, J_{sc}, and V_{oc} values of NH_3/NH_3 treated is possibly to the result of H, NH, or Ti_3^+ on the surface of the films. These species limit the ability of the film to separate and transport charge. Although the color of these films is significantly darker, there is only a slight shoulder in the *IPCE* curve at ~630 nm signifying that the color change in these films arises from F-type centers that act as recombination sites. These films have quicker voltage decay as a result of fast recombination and possibly because surface chemical reactions quickly convert trapped charges by for instance converting Ti^{4+} sites to Ti^{3+} sites and releasing oxygen. After NH_3/NH_3 treated films are annealed, their J_{sc}, V_{oc}, and *IPCE* values improve, but the overall efficiency of the DSSCs only slightly improve. This is caused by the decrease in H or TiN content of the films and increase in the 404 eV N 1s XPS binding environment. The 397 eV XPS peak is detrimental to the films, but the 404 eV peak might be causing lower η_{eff}, and future experiments of films annealed for longer times with lower nitrogen content would reveal the effects of the 404 eV N 1s XPS peak.

5.4 Summary

Although these modifications do not improve the photocatalytic performance of the P25 materials or the photovoltaic efficiencies of the Solaronix films, valuable information has been gleaned regarding how the plasma treatments affect the surface of the TiO_2. Many of these experiments clearly provide more opportunities for experimentation and further work is vital to testing the hypotheses presented in the Section 5.3 above.

From the photocatalytic experiments, we have learned that P25 treated powders have more defects that limit RhB deentylation and improve complete RhB decomposition. The change in the decomposition rate constant with temperature is ascribed primarily to the adsorption and desorption of species onto the TiO_2. The decrease in photocatalytic activity of P25 after it has been sintered into films is explained by a change in agglomeration size or surface area of the particles. In general, the lower the nitrogen level incorporated into the TiO_2, the better the photocatalytic activity. Coating the particles with HMDSO does not diminish the photocatalytic activity; when used to coat films already plasma treated, an improvement was observed. No significant visible light decomposition of RhB occurred for all treatments. In terms of product development, the diminished photocatalytic performance of the treated TiO_2 can be applied to improve sunscreens which require reduction or elimination of the photocatalytic activity of TiO_2.[26, 27]

From the photovoltaic experiments we have learned that plasma treated Solaronix photoanodes still have the possibility of improving DSSCs. The trap states induced by Ti^{3+} centers in NH_3/NH_3 films increase ehp recombination. NH_3/O_2 treated photoanodes

have improved J_{sc} values and higher *IPCE* values at wavelengths > 600 nm. With more experimentation including photoanodes with lower nitrogen content, these V_{oc} values could be improved. Photoanodes with incorporated silicon content have not yet been tested, but would likely help increase N3 dye absorption. Photocatalytic and photovoltaic devices made from treated TiO_2 have given more insights into the induced material changes and opens up more opportunities for experimentation.

5.5 References

1. Emeline, A. V.; Kuznetsov, V. N.; Rybchuk, V. K.; Serpone, N., Visible-light-active titania photocatalysts: The case of N-doped TiO($_2$)s-properties and some fundamental issues. *International Journal of Photoenergy* **2008**.
2. Henderson, M. A., A surface science perspective on TiO_2 photocatalysis. *Surface Science Reports* **2011,** *66* (6-7), 185-297.
3. Zhang, Q.; Joo, J. B.; Lu, Z. D.; Dahl, M.; Oliveira, D. Q. L.; Ye, M. M.; Yin, Y. D., Self-Assembly and Photocatalysis of Mesoporous TiO_2 Nanocrystal Clusters. *Nano Research* **2011,** *4* (1), 103-114.
4. Fabrega, C.; Andreu, T.; Guell, F.; Prades, J. D.; Estrade, S.; Rebled, J. M.; Peiro, F.; Morante, J. R., Effectiveness of nitrogen incorporation to enhance the photoelectrochemical activity of nanostructured TiO_2:NH_3 versus H_2-N_2 annealing. *Nanotechnology* **2011,** *22* (23).
5. Romero-Gomez, P.; Hamad, S.; Gonzalez, J. C.; Barranco, A.; Espinos, J. P.; Cotrino, J.; Gonzalez-Elipe, A. R., Band gap narrowing versus formation of electronic states in the gap in N-TiO_2 thin films. *J. Phys. Chem. C* **2010,** *114* (51), 22546-22557.
6. Jo, W. K.; Shin, M. H., Visible-light-activated photocatalysis of malodorous dimethyl disulphide using nitrogen-enhanced TiO_2. *Environmental Technology* **2010,** *31* (5), 575-584.
7. Lee, S. H.; Yamasue, E.; Ishihara, K. N.; Okumura, H., Photocatalysis and surface doping states of N-doped TiO_x films prepared by reactive sputtering with dry air. *Applied Catalysis B-Environmental* **2010,** *93* (3-4), 217-226.
8. Camps, E.; Escobar-Alarcon, L.; Camacho-Lopez, M. A.; Casados, D. A. S., Visible-light photocatalytic activity of nitrided TiO_2 thin films. *Mater. Sci. Eng. B-Adv. Funct. Solid-State Mater.* **2010,** *174* (1-3), 80-83.
9. Maeda, M.; Yamada, T.; Watanabe, T., Photocatalytic properties of plasma-nitrided TiO2 films. *Journal of the Electrochemical Society* **2007,** *154* (3), P29-P31.
10. Zhang, Q. F.; Cao, G. Z., Nanostructured photoelectrodes for dye-sensitized solar cells. *Nano Today* **2011,** *6* (1), 91-109.
11. Gratzel, M., Conversion of sunlight to electric power by nanocrystalline dye-sensitized solar cells (vol 164, pg 3, 2004). *Journal of Photochemistry and Photobiology a-Chemistry* **2004,** *168* (3), 235-235.
12. Mohammadpour, R.; Zad, A. I.; Hagfeldt, A.; Boschloo, G., Comparison of trap-state distribution and carrier transport in nanotubular and nanoparticulate TiO_2 electrodes for dye-sensitized solar cells. *Chemphyschem* **2010,** *11* (10), 2140-2145.
13. Kopidakis, N.; Neale, N. R.; Zhu, K.; van de Lagemaat, J.; Frank, A. J., Spatial location of transport-limiting traps in TiO_2 nanoparticle films in dye-sensitized solar cells. *Applied Physics Letters* **2005,** *87* (20).
14. Zang, L., *Energy Efficiency and Renewable Energy Through Nanotechnology (Green Energy and Technology)*. 2011 edition ed.; Springer: London, 2011; p 957.

15. Pulsipher, D. J. V.; Martin, I. T.; Fisher, E. R., Controlled nitrogen doping and film colorimetrics in porous TiO_2 materials using plasma processing. *ACS Applied Materials & Interfaces* **2010,** *2* (6), 1743-1753.
16. Pulsipher, D. J. V.; Fisher, E. R., O_2 plasma treatment of mesoporous and compact TiO_2 photovoltaic films: Revealing and eliminating effects of Si incorporation. *Surface & Coatings Technology* **2009,** *203* (16), 2236-2242.
17. Zhuang, J. D.; Dai, W. X.; Tian, Q. F.; Li, Z. H.; Xie, L. Y.; Wang, J. X.; Liu, P.; Shi, X. C.; Wang, D. H., Photocatalytic degradation of RhB over TiO_2 bilayer films: effect of defects and their location. *Langmuir* **2010,** *26* (12), 9686-9694.
18. van der Meulen, T.; Mattson, A.; Osterlund, L., A comparative study of the photocatalytic oxidation of propane on anatase, rutile, and mixed-phase anatase-rutile TiO_2 nanoparticles: Role of surface intermediates. *J. Catal.* **2007,** *251* (1), 131-144.
19. Herrmann, J. M., Photocatalysis fundamentals revisited to avoid several misconceptions. *Applied Catalysis B-Environmental* **2010,** *99* (3-4), 461-468.
20. Miyauchi, M.; Ikezawa, A.; Tobimatsu, H.; Irie, H.; Hashimoto, K., Zeta potential and photocatalytic activity of nitrogen doped TiO_2 thin films. *Physical Chemistry Chemical Physics* **2004,** *6* (4), 865-870.
21. Cojocaru, B.; Neatu, S.; Sacaliuc-Parvulescu, E.; Levy, F.; Parvulescu, V. I.; Garcia, H., Influence of gold particle size on the photocatalytic activity for acetone oxidation of Au/TiO_2 catalysts prepared by dc-magnetron sputtering. *Applied Catalysis B-Environmental* **2011,** *107* (1-2), 140-149.
22. Kochuveedu, S. T.; Kim, D. P.; Kim, D. H., Surface-plasmon-induced visible light photocatalytic activity of TiO_2 nanospheres decorated by Au nanoparticles with controlled configuration. *J. Phys. Chem. C* **2012,** *116* (3), 2500-2506.
23. Dong, W. Y.; Lee, C. W.; Lu, X. C.; Sun, Y. J.; Hua, W. M.; Zhuang, G. S.; Zhang, S. C.; Chen, J. M.; Hou, H. Q.; Zhao, D. Y., Synchronous role of coupled adsorption and photocatalytic oxidation on ordered mesoporous anatase TiO_2-SiO_2 nanocomposites generating excellent degradation activity of RhB dye. *Applied Catalysis B-Environmental* **2010,** *95* (3-4), 197-207.
24. Kusakabe, K.; Ezaki, M.; Sakoguchi, A.; Oda, K.; Ikeda, N., Photocatalytic behaviors of silica-loaded mesoporous titania. *Chemical Engineering Journal* **2012,** *180*, 245-249.
25. Nussbaum, M.; Paz, Y., Ultra-thin SiO_2 layers on TiO_2: improved photocatalysis by enhancing products' desorption. *Physical Chemistry Chemical Physics* **2012,** *14* (10), 3392-3399.
26. Virkutyte, J.; Al-Abed, S. R.; Dionysiou, D. D., Depletion of the protective aluminum hydroxide coating in TiO_2-based sunscreens by swimming pool water ingredients. *Chemical Engineering Journal* **2012,** *191*, 95-103.
27. Serpone, N.; Dondi, D.; Albini, A., Inorganic and organic UV filters: Their role and efficacy in sunscreens and suncare product. *Inorganica Chimica Acta* **2007,** *360* (3), 794-802.

CHAPTER 6

NH_2 AND NH SURFACE PRODUCTION IN PULSED NH_3 PLASMAS ON TIO_2: A STEADY-STATE PROBE OF SHORT PULSE PLASMAS

This chapter contains data from a full paper submitted to *Plasma Processes and Polymers* and written by Daniel J. V. Pulsipher and Ellen R. Fisher. This chapter analyzes gas-phase densities and surface reactions of NH and NH_2 in pulsed NH_3 plasmas used to nitride TiO_2 surfaces by systematically varying peak plasma power and pulsing *d.c.* Interconnected trends of gas-phase densities and surface reactions are determined by using LIF, OES, and IRIS techniques. Data collected from various *d.c.* values are used to determine species behaviors during short plasma pulses in the initiation and afterglow plasma regimes.

6.1 Introduction

Nitride and oxynitride materials are becoming increasingly important in water photolysis and other catalytic processes. Consequently, nitrogen doping of materials such as TiO_2, creating an oxynitride material, extends the photocatalytic capability of the wide band gap oxide by utilizing more of the visible light spectrum, allowing for more efficient decomposition of organic pollutants.[1] Other oxynitride materials such as TaON and $(Ga_{1-x}Zn_x)(N_{1-x}O_x)$ show high activity for O_2 evolution in H_2O under visible light irradiation.[2] Although there are many approaches to introducing nitrogen into oxide mate-

rials, plasmas offer a controllable method of creating N-doped oxide materials containing N in a specific binding environment.[3] With the high controllability of plasma processes, however, comes a plethora of adjustable plasma parameters including precursor pressure, applied rf power (P), and substrate location, among others. Thus, optimizing a particular plasma process requires systematically studying the dependence of materials properties on each relevant parameter.

Although pulsed plasmas introduce additional parameters such as *d.c.* and peak applied rf power (P_p), they are often used to eliminate undesirable effects of continuous-wave (CW) plasmas. The high plasma powers needed to modify inorganic materials can result in high ion accelerating voltages that sputter reactor materials and cause substrate damage.[4] Pulsed plasmas prevent charge buildup and ion bombardment time to effectively limit film damage. They also benefit from higher instantaneous powers,[5, 6] reduced substrate temperatures,[4] treatment uniformity,[7] and more control over specific plasma species produced. Pulsing plasmas significantly impacts gas-phase densities of both charged and neutral species in the system. Changes in species densities that result from short plasma pulses have been investigated in Ar,[6,8-11] Ne,[12] O_2,[13] and Ar-based discharges sputtering Cu[5, 14] and aluminum[15] substrates. These studies show the densities of plasma species during short on times (t_{on}) or short off times (t_{off}) can be up to 10 times larger than densities in steady-state plasma conditions.[14] These studies use time-resolved measurements of fast (μs-ms) pulses to resolve temporal density profiles; here we propose steady-state measurements of fast pulses to gain similar information employing optical diagnostic tools.

As noted above, one plasma parameter unique to pulsed plasmas is *d.c.* ($d.c. = \frac{t_{on}}{t_{on} + t_{off}} x\ 100$). As can be seen from this relationship, the same *d.c.* can be achieved with different combinations of t_{on} and t_{off}, providing another level of complexity to this parameter. One major effect of changes in *d.c.* is that the contributions of ions to substrate processing is considerably different than in CW plasmas because of the different lifetimes of ions and radicals during the plasma-off time.[16] Thus, the impact of ion bombardment on both gas-phase and surface reactions leading to plasma surface modifications can be elucidated from studies of species densities and surface reactivities as a function of the *d.c.* of pulsed plasmas.

In the present work, we employed laser induced fluorescence (LIF) in conjunction with optical emission spectroscopy (OES) to determine the densities of plasma species as a function of pulsed plasma parameters. These complementary techniques provide ground state (LIF) and excited state (OES) densities, and can also provide additional relevant information on energy partitioning.[17] OES spectra are generally used to approximate trends in corresponding ground state species, yet this assumption is not always valid. By using both techniques, information about significant gas-phase plasma reactions can be gathered, and desirable plasma conditions for specific treatments can be easily selected.

In conjunction with gas-phase density data, specific surface reactivity data acquired with our imaging of radicals interacting with surfaces (IRIS) technique discloses relationships between surface reactions and changes in plasma conditions.[18, 19] The LIF-based IRIS technique allows for determining radical-surface reactivities and energy partitioning in different degrees of freedom of the radicals before and after they interact with

the substrate. IRIS data yield the surface scatter coefficient (*S*), which is effectively the ratio of scattered molecules to incident molecules during plasma processing of a substrate. We previously measured *S* values for both NH_2 [*S*(NH_2)] and NH [*S*(NH)] in CW NH_3 plasmas (45-225 W) using Si, SiO_2, Si_3N_4, polyimide, poly(tetrafluoroethylene), Pt, and Cu substrates for *S*(NH_2),[20, 21] and polyimide, poly(tetrafluoroethylene), and Pt substrates for *S*(NH).[22] These studies showed *S*(NH_x) values were highly dependent on substrate composition, relative gas-phase densities, gas-phase translational, rotational, and vibrational temperatures, and ionic content of the plasma.

Here we investigated gas-phase reactions, surface reactions, and the relationship between the two in NH_3 pulsed plasmas using TiO_2 substrates. We deduce possible contributing reactions by examining the dependence of gas phase densities and *S*(NH_x) values on *d.c.* and P_p. Via experiments with either t_{on} or t_{off} held constant, we explored the gas-phase species that are controllable over short plasma pulses. Combining gas-phase and IRIS surface reactivity data reveal significant surface reactions that contribute to NH_2 and NH surface production on carbonaceous TiO_2 substrates.

6.2 Results

Plasma Power Dependences of NH and NH_2 Densities. LIF and OES provide insight into gas-phase plasma chemistry by revealing relative densities of ground and excited state plasma species, respectively. To examine the effect of different plasma parameters on the gas-phase densities of both NH and NH_2 in our NH_3 plasmas, LIF and OES data were collected for pulsed NH_3 plasmas, Figures 6.1 and 6.2. Figure 6.1 shows normalized LIF data from NH_2 and NH using 70% *d.c.* pulsed NH_3 plasmas, along with pre-

viously reported data collected from CW NH_3 plasmas (100% *d.c.*).[20, 22] Interestingly, the trends found in CW plasmas for both NH and NH_2 also hold for pulsed plasmas when they are compared using equivalent plasma power (P_{eq}), where $P_{eq} = d.c. * P_p$. NH_2 densities start out low, reach a maximum, and then decrease to a density slightly higher than the initial density, Figure 6.1a. This trend suggests that at low P_{eq}, energy supplied to the plasma increases fragmentation of the NH_3 precursor. At higher P_{eq}, however, additional energy serves to fragment NH_2, depleting its gas-phase density. In contrast, NH densities start out low and then increase in almost a stepwise fashion, reaching a plateau at P_{eq} > ~150 W. Note that the threshold energy for this "step" occurs between P_{eq} = 70-140 W, approximately the same P_{eq} where the NH_2 densities begin to decrease. Notably, NH depletion in the gas phase does not occur under the tested plasma conditions.

OES spectra of NH_3 plasmas reveal the expected range of excited state plasma species, Figure 6.2. One of the most noticeable differences between the two spectra in Figure 6.2 is that emission from H_α^* increases dramatically at higher P_p, dominating the spectrum from a 300 W plasma. At P_p = 50 W, the most intense line in the spectrum corresponds to emission from NH at 335.8 nm. Given that it is often difficult to compare raw intensities in OES spectra, we have used actinometry to effectively normalize the results collected under different plasma conditions. Thus, Figure 6.3a shows the effect of P_p on the relative densities of specific excited state species in NH_3 plasmas. Note that NH_2^* peaks at P_{eq} = 70 W (P_p = 100 W), similar to the LIF data for ground state NH_2. The enlarged region for both NH_2^* and H_2^*, Figure 6.3b, reveals two peaks in the data for each species, and overall both species generally decline with P_p. This signifies two different deexcitation or reaction pathways may be activated as P_p increases.

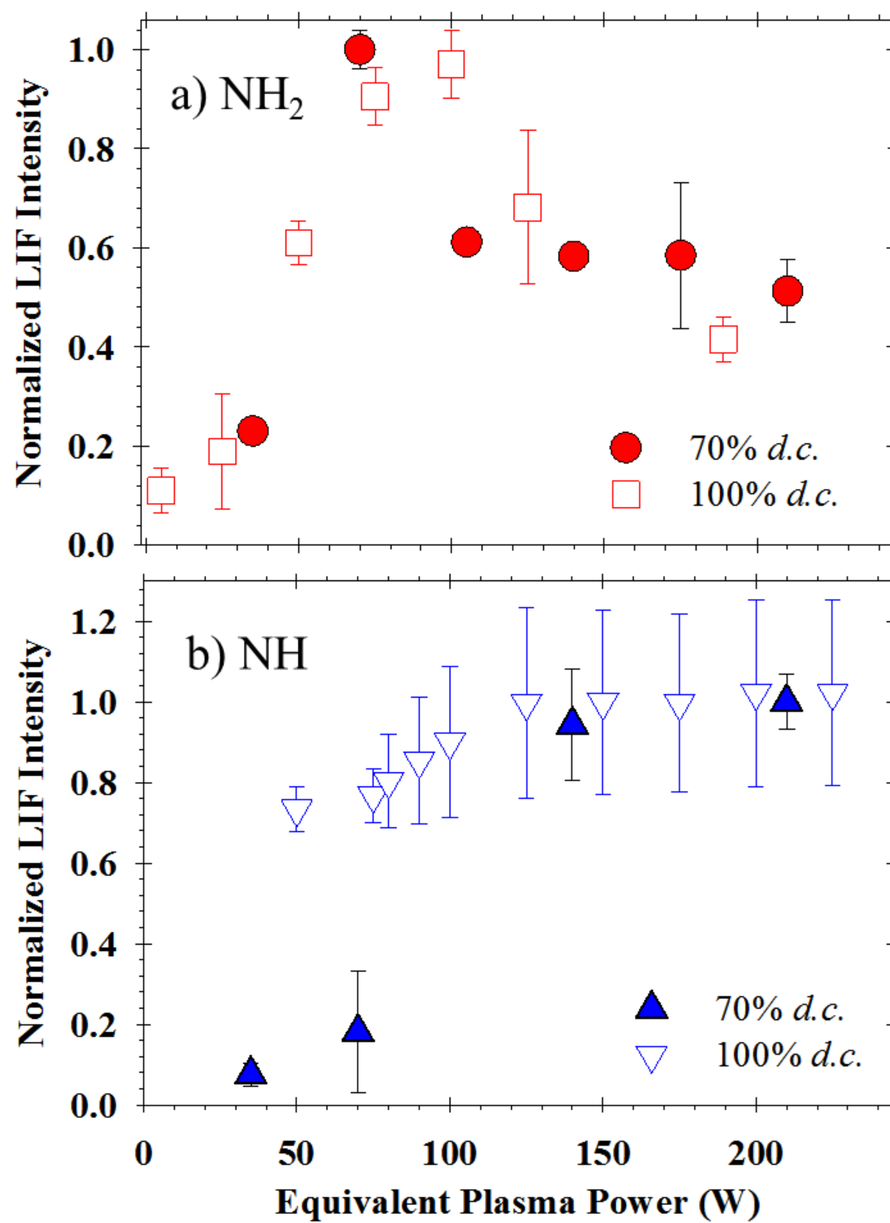

Figure 6.1. Normalized LIF intensity of a) NH_2 and b) NH radicals in NH_3 plasma molecular beams for both CW and pulsed plasmas as a function of P_{eq}.

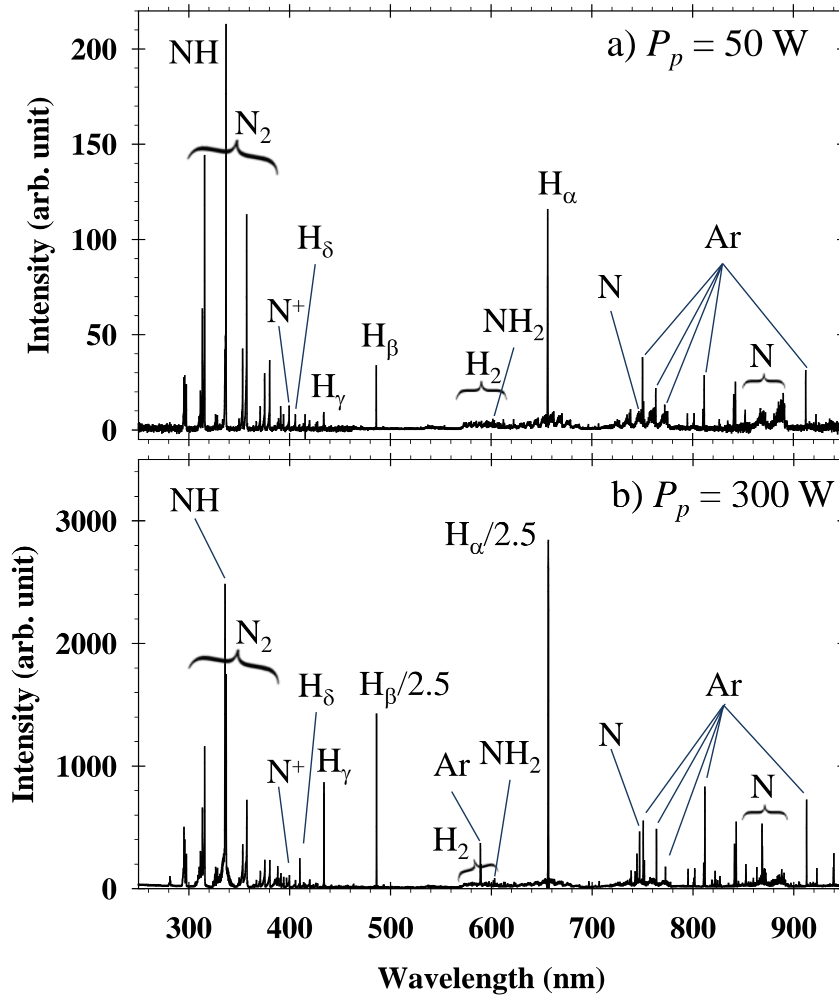

Figure 6.2. OES spectra of a) 50 W and b) 300 W peak power plasmas demonstrating changes in relative intensities of emitting species.

The maxima observed in the H_2^* and NH_2^* data are slightly offset from the peak observed in the H_α^* data. The H_α^* trace appears to be a superposition of the NH_2^* and NH^* traces. The H_α^* density is also similar to the ground state NH_2 density as they both plateau at higher P_p, whereas NH_2^* density continues to decrease.

Upon examining the other species plotted in Figure 6.3a, it becomes apparent that N^* and NH^* increase as N_2^* and H_2^* decrease with P_p, further evidence for increased NH_3 and NH_2 dissociation. The trend in NH^* correlates well with the trend in ground state densities of NH shown in Figure 6.1b; they both increase between P_{eq} = 70-140 W and then plateau at higher P_{eq}. Of the excited state molecular species monitored, NH^* is the only one that increases with increasing P_p. The two ionic species monitored are N_2^{+*} and N^{+*}. Although N^{+*} increases with P_p, N_2^{+*} initially follows a decreasing trend as does N_2^*, and then as N_2^* levels out N_2^{+*} slightly increases.

d.c. Dependence of NH and NH_2 Densities. The normalized LIF density data in Figure 6.4 reveal an increase in NH and NH_2 density with increasing *d.c.* and a slight difference in behavior depending on whether t_{on} or t_{off} is kept constant. For both sets of data, the LIF intensities were normalized to 0.5 for the 50% *d.c.* plasma conditions. Although NH_2 density increases linearly with *d.c.* when t_{on} is kept constant, it is higher for plasmas with *d.c.* < 50% when t_{off} is kept constant, Figure 6.4a, relative to keeping t_{on} constant. In contrast, NH densities increase monotonically with *d.c.* when either t_{on} or t_{off} is kept constant. Notably, the increase in NH density at high *d.c.* under constant t_{off} conditions is much more dramatic than for constant t_{on} conditions. Thus, these results demonstrate that both the plasma *d.c.* and the plasma pulsing rate affect both NH_2 and NH LIF densities.

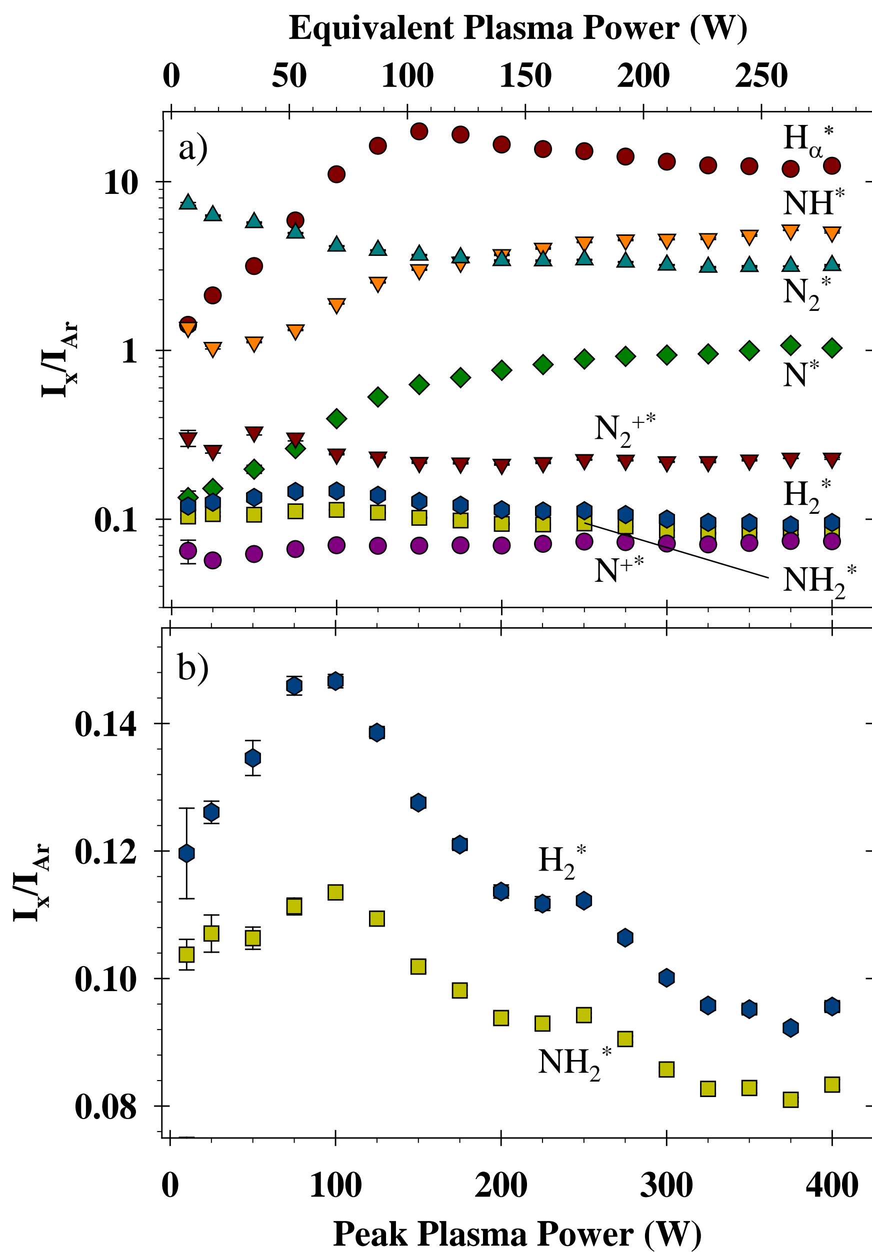

Figure 6.3. Actinometric OES data revealing trends of excited state species as a function of P_p plotted in a) showing trends of all species monitored and in b) showing a more specific region emphasizing the trends in NH_2^* and H_2^*.

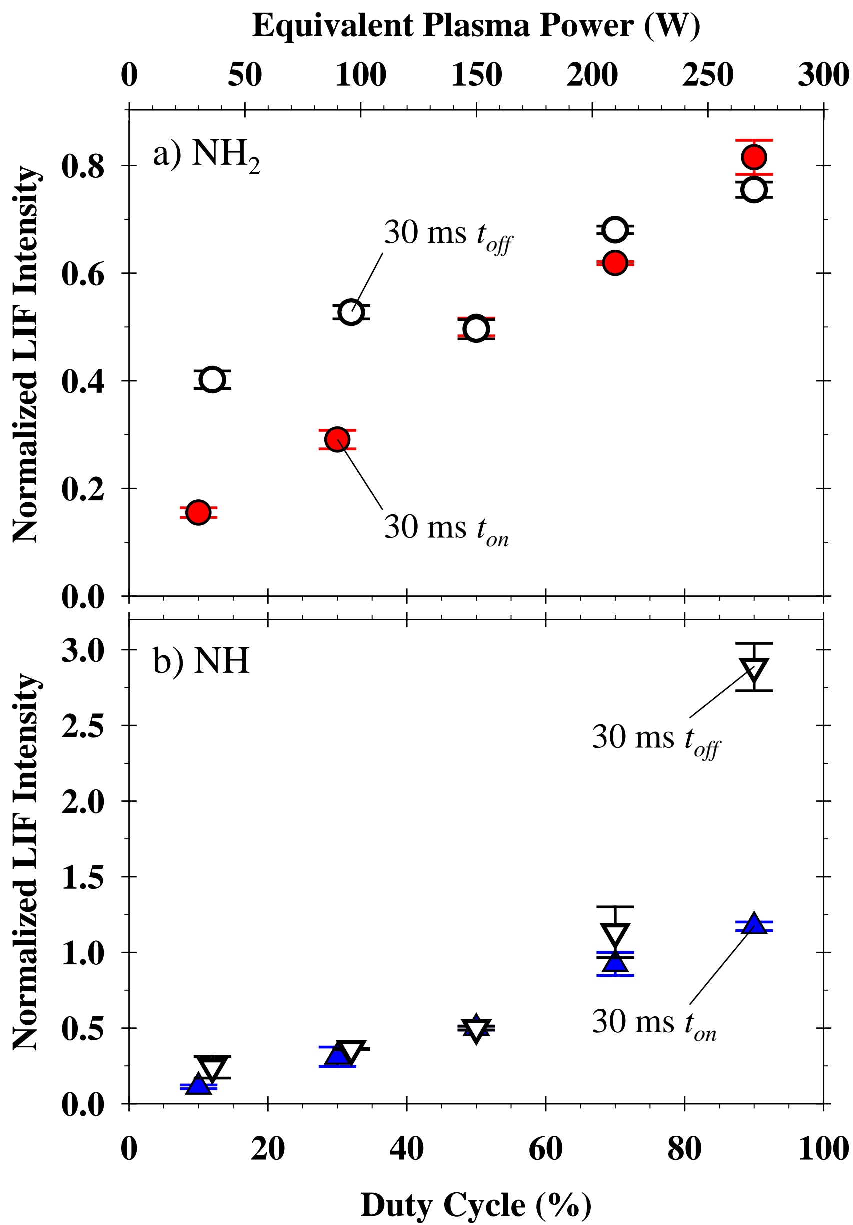

Figure 6.4. Normalized LIF intensity of a) NH_2 and b) NH radicals in the molecular beam for pulsed plasmas revealing trends with changing *d.c.* while keeping t_{on} or t_{off} constant at 30 ms.

OES data in Figure 6.5a reveal the density of most excited state species in our NH_3 plasmas do not change significantly with *d.c.* or with plasma pulse rate. The general increase in density with *d.c.* seen with both ground state NH_2 and NH species is also measured for NH_2^*, but not with NH^*. The slight increase in NH_2^* with *d.c.* is less dramatic than that observed for ground state NH_2. Notably, the singlet (NHc^*) and triplet excited states of NH behave differently with *d.c.* and with different t_{on} values at the same *d.c.*

The ion content of these plasmas also changes with *d.c.*, Figure 6.5b. The largest changes with *d.c.* occur with the N_2^{+*} t_{off} data which increases dramatically with *d.c.*, signifying that lower *d.c.* conditions with a short t_{on} produce less N_2^{+*}, similar to NHc^*, also shown in Figure 6.5b. Concurrently, N^{+*} ions are not affected by small t_{on}. In Figure 6.5b, it is not initially obvious that the molecular ion content of these plasmas increases with *d.c* because the N_2^{+*} t_{on} data decrease. However, considering that N_2^* density also decreases over *d.c.* (Figure 6.5a), and assuming that the ratio of exited state to ground state species is constant for both neutrals and ions, the emission signal from ions can be normalized to the signal from neutrals. Thus, the N_2^{+*}/N_2^* t_{on} and N^{+*}/N^* t_{on} data shown in Figure 6.5b generally increase with *d.c.* as expected.

The largest differences in behavior between constant t_{on} and constant t_{off} conditions is seen in the H_α^* data, Figure 6.6. Note that the P_p dependence of H_α^* is similar to that for ground state NH_2, Figure 6.3a, where constant t_{off} conditions lead to higher species densities at *d.c.* < 50%. When comparing H_α, H_β and H_γ data, the spread in intensity between the H_α t_{on} and the H_α t_{off} data at lower *d.c.* conditions is less pronounced in the H_β data.

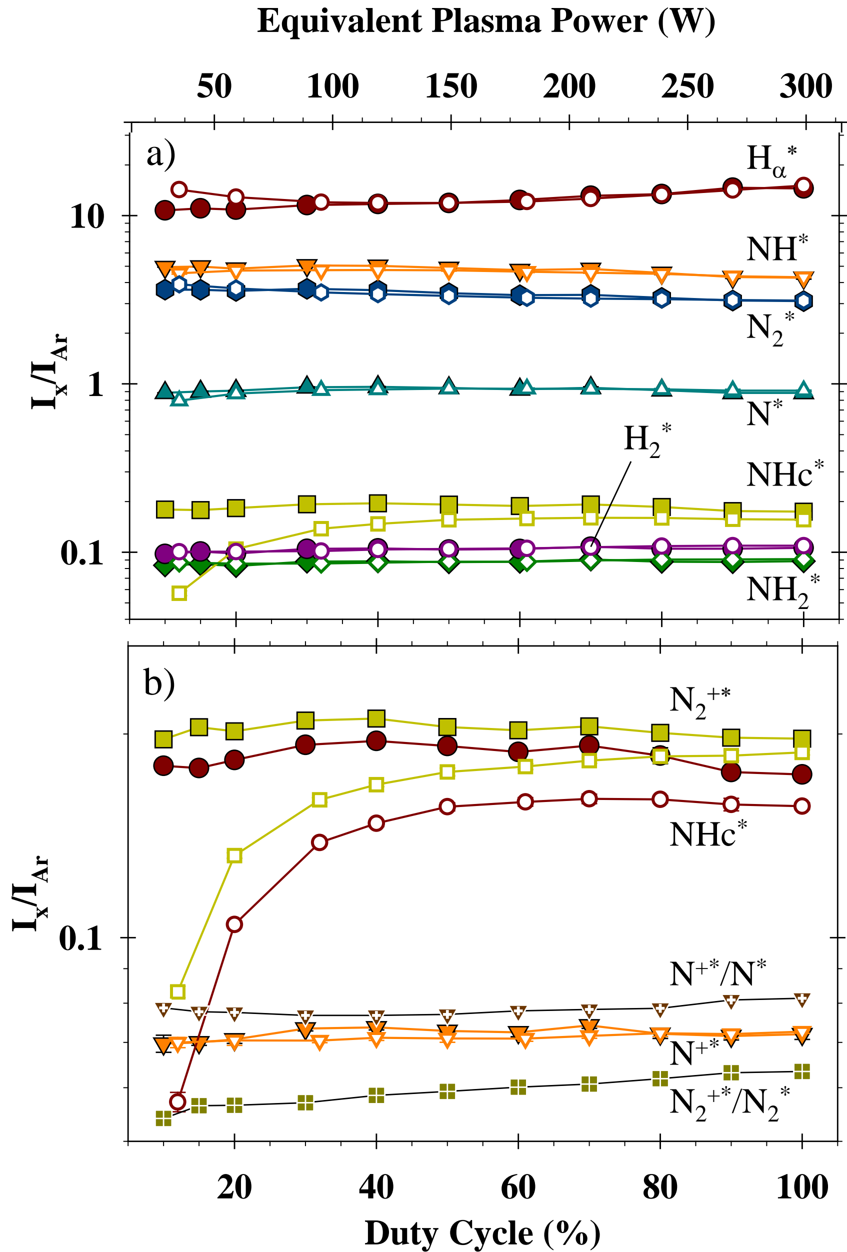

Figure 6.5. Actinometric OES data of excited state species as a function of *d.c.* for both constant t_{on} (filled symbols) and t_{off} (open symbols) conditions of a) neutral species and b) ionic species and NHc^*.

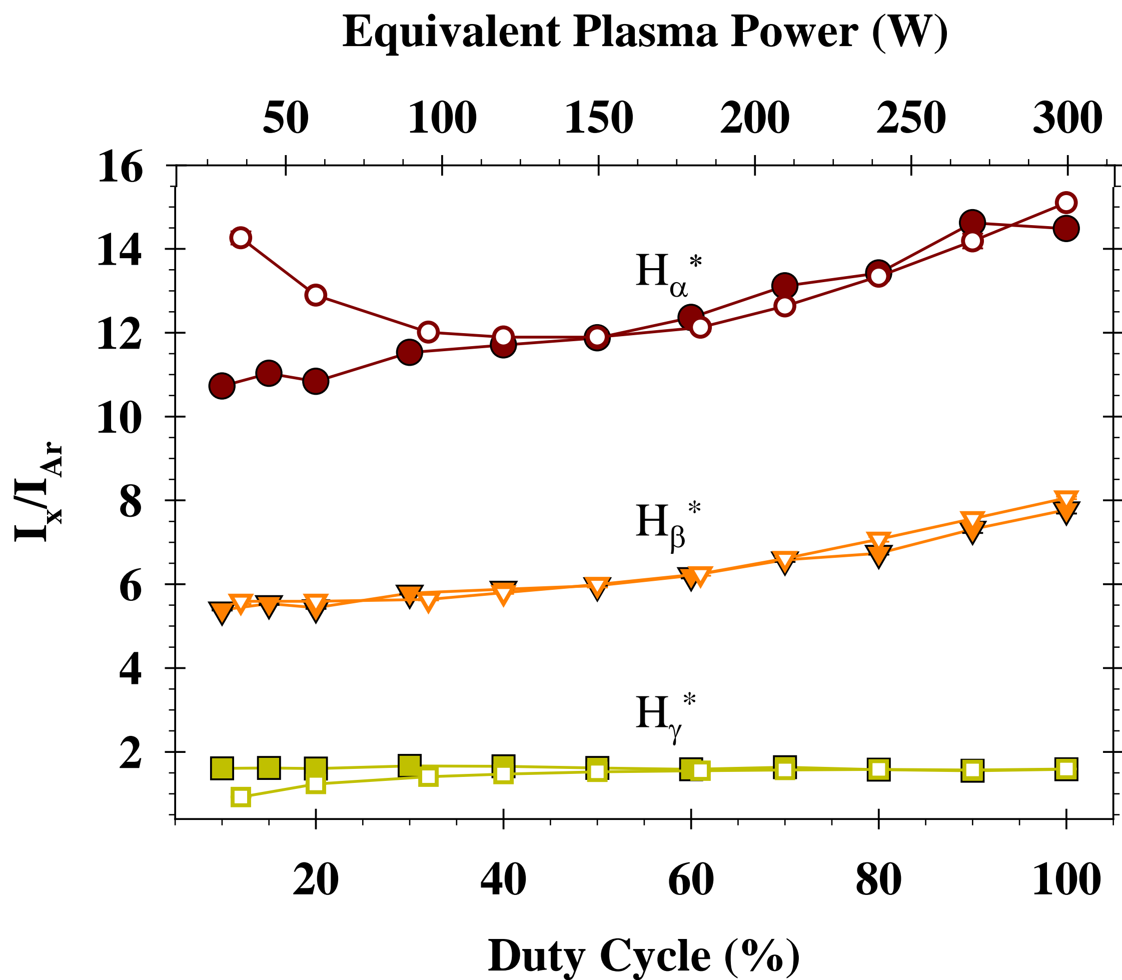

Figure 6.6. Actinometric OES data of three different excited states of hydrogen atoms as a function of *d.c.* for both constant t_{on} (filled symbols) and t_{off} (open symbols) conditions.

For H_γ, the t_{off} data displays slightly lower values than the t_{on} data at low *d.c.*, but the values are nearly identical above *d.c.* = 40%. The lower t_{off} intensities at low *d.c.* arise because the higher pulsing rate hinders formation of the H_γ excited state. A t_{on} > 3-20 ms is needed to create the convergent H_γ excited state population observed.

Surface Reactivity of NH and NH_2. Figure 6.7 shows a series of images acquired for NH_2 molecules using molecular beams formed from 50 W and 300 W NH_3 plasmas and scattered off of TiO_2 substrates. Using TiO_2 substrates is unprecedented in IRIS experiments; here we measured surface scatter coefficients for NH_2 and NH radicals interacting with two different types of TiO_2 substrates. The spatial geometry of IRIS experiment is shown in the NH_2 LIF images in Figure 6.7 (panels a-c). Figures 6.7a and 6.7e contain LIF images from molecules both in the incident molecular beam and scattered off of the substrate, whereas only signal from NH_2 in the incident molecular beam is imaged in Figures 6.7b and 6.7f. Signal arising from molecules scattered off of the substrate was obtained by subtracting the images in Figures 6.7b and 6.7f from those in Figures 6.7a and 6.7e, respectively. The resulting images are shown in Figures 6.7c and 6.7g. Cross-sectional data obtained as described above for NH_2 in the molecular beams and scattered off of the TiO_2 substrate are shown in Figures 6.7d and 6.7h. Also shown in this figure are the simulation results for these particular data sets, ultimately yielding *S* values. Results for all IRIS experiments performed for both NH_2 and NH are summarized as a function of P_p in Table 6.1 and as a function of *d.c.* in Table 6.2. Note that within experimental error, all *S* values measured for both NH_2 and NH are greater than or equal to unity, signifying a net surface production under nearly all conditions studied.

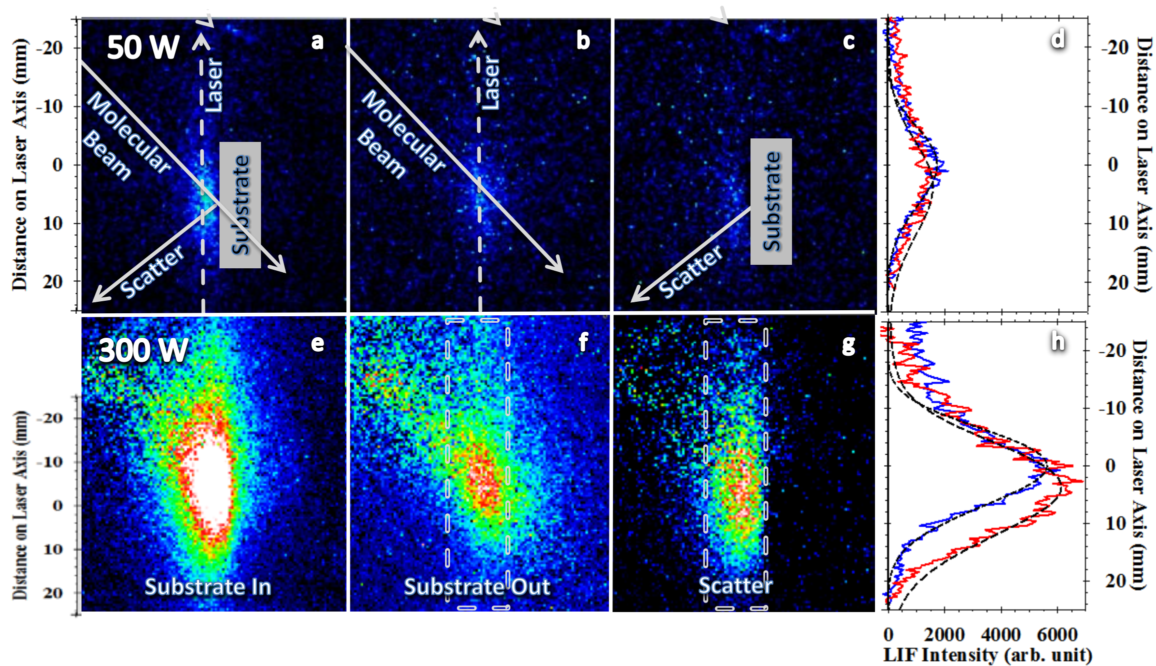

Figure 6.7. Spatially resolved LIF images and cross-sectional IRIS data for NH_2 molecules using a pulsed NH_3 plasma molecular beam with (a-d) P_p = 50 W or (e-h) P_p = 300 W. Images in panels a) and e) are signals arising from both the incident molecular beam and scattered off the surface; panels b) and f) contain images from molecules in the molecular beam only and panels c) and g) contain images resulting from scatter molecules only. The cross-sectional data arises directly from averaging a column 20 pixels wide, represented by the dashed lines in the images. Also shown in panels d) and h) are simulations to the data (dashed lines).

Both *S*(NH) and *S*(NH_2) tend to increase with P_{eq}, regardless of whether P_p or *d.c.* changes. This is discussed further below.

Initially, T/SP paste was used to create the mesoporous TiO_2 substrates used in IRIS experiments. For these initial experiments, one substrate was used to collect LIF images across all changes in P_p to compose one data set. Multiple data sets were collected to provide the weighted average *S*(NH_2) values reported in Table 6.1. After the experiments, XPS analyses of the substrates revealed a high carbon content (up to 68.6% C) specifically in the area of the substrate exposed to the molecular beam. Furthermore, XPS analysis could no longer detect any Ti atoms in this region of the substrate. This prompted the use of compact TiO_2 films in IRIS experiments, which are cheaper and easier to make, thereby allowing for a new substrate to be used for each experiment. Use of fresh substrates for each set of conditions resulted in the *S*(NH_2) values listed in Table 6.1 for compact TiO_2 substrates.

XPS analysis of untreated compact TiO_2 films stored under ambient lab conditions contained 9.3 ± 1.4% C; they contained 16.9 ± 2.7% C after being placed under vacuum in the IRIS chamber for 1 hr. When the films were exposed to the molecular beam, the carbon content, nitrogen content, and O/Ti ratio increased with increasing P_p, Table 6.1, whereas the titanium and oxygen content decreased. An Ar sputtering experiment in the XPS instrument demonstrated that much of this added carbon content could be removed within 30 min , with overall changes of 58% to 15% C and 5.4 to 2.2% N after sputtering. Notably, the changes in atomic composition of the films during an IRIS experiment do not correlate with *S*(NH_2) or *S*(NH) values.

Table 6.1. *S*(NH_2) and *S*(NH) measured at different P_p and XPS compositional data.

P_p (W)	50	100	150	200	250	300
***S*(NH) T/SP**	1.18 ± 0.13	1.4 ± 0.07	--	1.9 ± 0.09	--	1.93 ± 0.05
***S*(NH_2) T/SP**	1.29 ± 0.06	1.31 ± 0.05	1.22 ± 0.16	1.58 ± 0.11	1.59 ± 0.18	1.63 ± 0.09
***S*(NH_2) compact**	1.28 ± 0.07	1.45 ± 0.13	1.21 ± 0.07	1.64 ± 0.14	1.94 ± 0.08	1.77 ± 0.26
% C[a)]	34.8 ± 6.3	47.5 ± 1.0	49.7 ± 0.1	53.3 ± 1.0	50.4 ± 1.0	64.2 ± 4.0
% N[a)]	0.7 ± 0.1	3.8 ± 2.0	4.4 ± 0.1	3.6 ± 0.3	6.3 ± 1.5	11.4 ± 2.2
% Ti[a)]	17.0 ± 0.8	11.4 ± 0.8	10.4 ± 0.2	8.3 ± 0.6	8.9 ± 0.1	3.0 ± 0.3
% O[a)]	46.2 ± 5.5	34.6 ± 2.0	33.5 ± 0.1	32.2 ± 0.1	32.4 ± 2.0	15.4 ± 1.1
O/Ti[a)]	2.7	3.0	3.2	3.9	3.6	5.1

[a)]XPS data acquired directly after S(NH_2) IRIS measurements on TiO_2 compact films at each P_p.

Table 6.2. $S(NH_2)$ and S(NH) measured at different *d.c.* and XPS compositional data.

***d.c.* (%)**	**12.5 ± 2.5**	**30**	**50**	**70**	**90**
S(NH) t_{on}	1.27 ± 0.11	1.04 ± 0.10	1.29 ± 0.07	1.82 ± 0.06	1.78 ± 0.06
S(NH) t_{on} g.m.	--	1.71 ± 0.13	1.42 ± 0.13	1.55 ± 0.08	1.97 ± 0.12
$S(NH_2)$ t_{off}	1.40 ± 0.17	1.82 ± 0.16	1.99 ± 0.18	1.85 ± 0.12	2.04 ± 0.22
$S(NH_2)$ t_{on} g.m.	--	2.14 ± 0.25	1.95 ± 0.16	1.82 ± 0.15	1.53 ± 0.18
$S(NH_2)$ t_{on}	1.10 ± 0.20	1.33 ± 0.11	1.83 ± 0.14	1.49 ± 0.12	2.11 ± 0.16
% C[a)]	--	45.2	54.4	68.6	58
% N[a)]	--	1.8	3.5	9.1	5.4
% Ti[a)]	--	12.7	10.7	3.1	7.0
% O[a)]	--	40.3	31.3	16.6	29.6
O/Ti[a)]	--	3.2	2.9	5.4	4.2

[a)]XPS data acquired after $S(NH_2)$ t_{on} IRIS measurements on TiO_2 compact films at each *d.c.*

The morphology of the surface (mesoporous or compact) and the surface composition also did not significantly impact *S*(NH_2) values, as all but one of the values measured using the two different TiO_2 films overlap in experimental error.

Figure 6.8 shows the combined *S*(NH_2) T/SP and *S*(NH_2) compact values (weighted averages of all measurements, regardless of substrate) as a function of P_{eq}. Also plotted in Figure 6.8 are *S*(NH) values collected using T/SP substrates. Overall, both *S*(NH_2) and *S*(NH) increase substantially with P_{eq}. For NH_2, the scatter values measured are relatively constant below P_{eq} = 105 W. Above this P_{eq}, *S*(NH_2) increases dramatically and then decreases slightly at the highest P_{eq}. This behavior and the behavior of *S*(NH) with changing P_p mimic rather closely the NH LIF and OES densities in the molecular beam shown in Figures 6.1b and 6.3a, respectively.

Similar to the gas-phase NH_x density data, *S*(NH_2) values were also measured as a function of *d.c.* holding either t_{on} or t_{off} constant, Figure 6.9a. As *d.c.* increases, *S*(NH_2), values generally increase, regardless of which time parameter is held constant. Although some *S*(NH_2) values collected with constant t_{off} conditions are higher than those from constant t_{on} conditions, the majority are within experimental error. In Figure 6.9b, *S*(NH) values measured with constant t_{on} generally increase with increasing *d.c.* Figure 6.9 also includes data collected using a grounded mesh (g.m.) attached to the molecular beam defining slits to reduce the ion content in the molecular beam. Both *S*(NH_2) and *S*(NH) obtained under ion-limited conditions result in higher scatter coefficients at *d.c.* = 30%. XPS atomic composition data from substrates used in the IRIS experiments that yielded the *S*(NH_2) t_{on} values are also listed in Table 6.2.

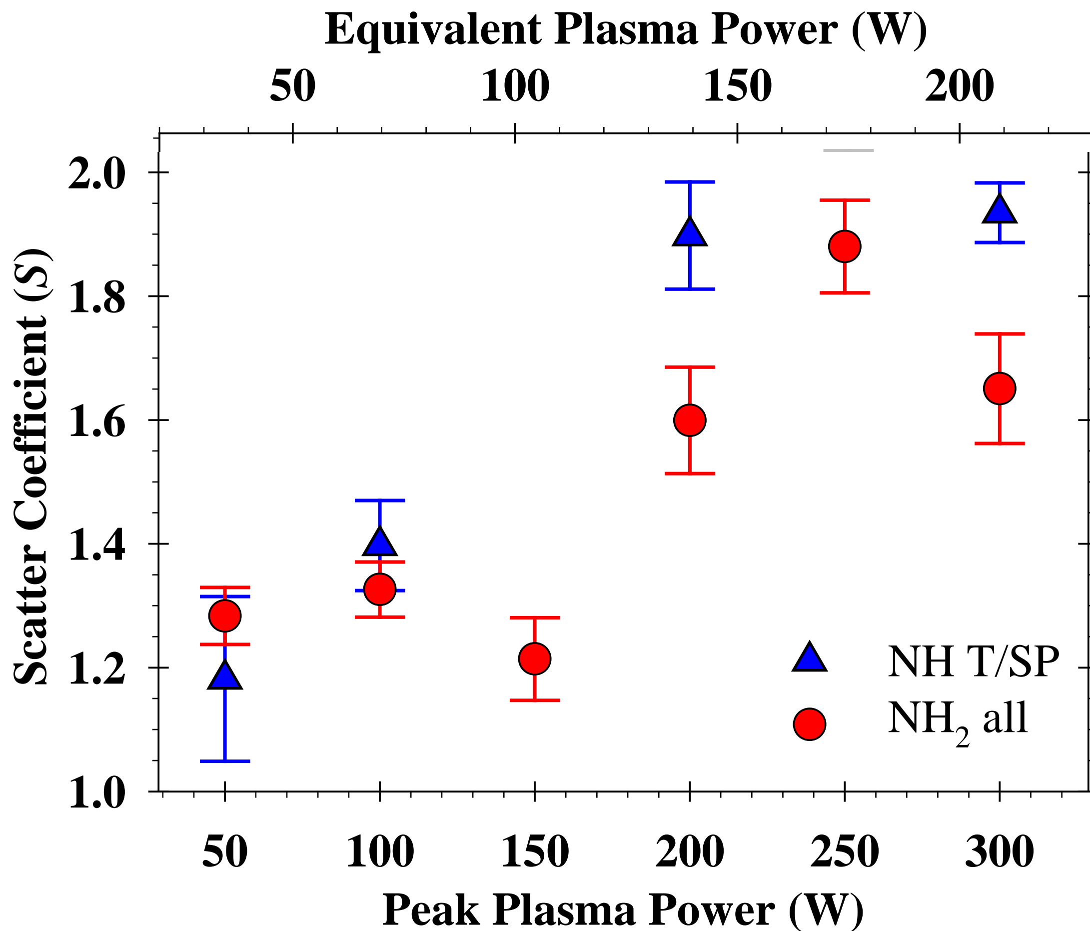

Figure 6.8. Scatter coefficients of NH and NH_2 as a function of P_p on both mesoporous and dense carbonaceous TiO_2 substrates.

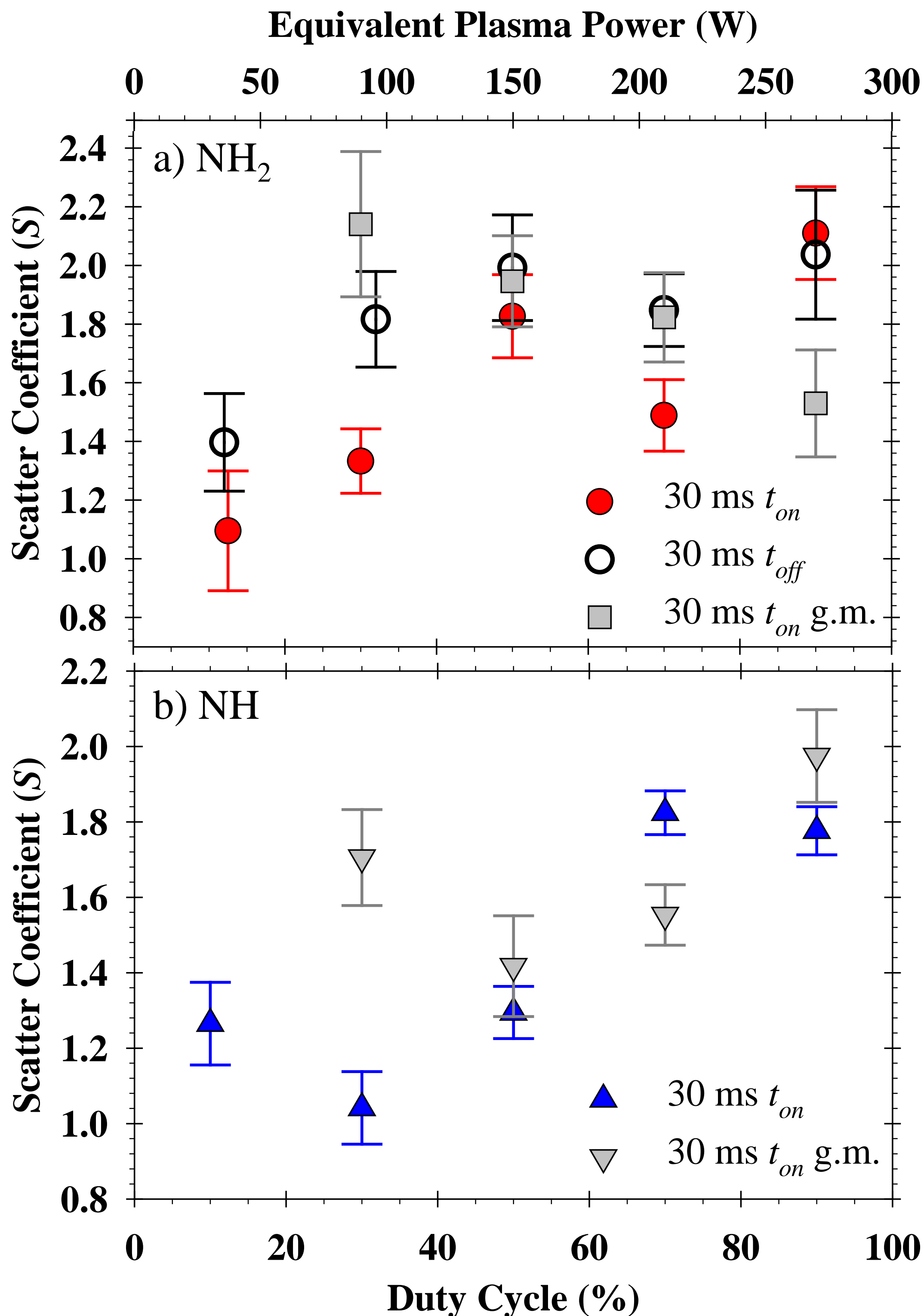

Figure 6.9. Scatter coefficients of a) NH_2 and b) NH as a function of *d.c.* on carbonaceous TiO_2 substrates for constant t_{on}, t_{off}, and g.m. conditions.

Table 6.3. Relevant gas-phase reactions resulting in NH_2 and NH production

Reaction	NH_2 Production Reactions			Reaction	NH Production Reactions		
1	NH_4^+	→	$NH_2 + H_2^+$	14	NH_4^+	→	$NH + H_2 + H^+$
2	**NH_3**	→	**$NH_2 + H$**	15	NH_3	→	$NH + H_2$
3	$NH_3 + H$	→	$NH_2 + H_2$	16	$NH_3 + H$	→	$NH + H_2 + H$
4	$NH_3 + NH_4^+$	→	$2NH_2 + H_2 + H^+$	17	$NH_3 + NH_4^+$	→	$2NH + 2H_2 + H$
5	$NH_3 + NH_4^+$	→	$NH_2 + NH^+ + 2H_2$	18	$NH_3 + NH_4^+$	→	$NH_2 + NH^+ + 2H_2$
6	$NH_3 + N$	→	$NH_2 + NH$	19	$NH_3 + N$	→	$NH + NH_2$
7	NH_3^+	→	$NH_2 + H^+$	20	**NH_2**	→	**$NH + H$**
8	$NH + H$	→	NH_2	21	$NH_2 + NH_2$	→	$NH + NH_3$
9	$NH + NH$	→	$NH_2 + N$	22	$NH_2 + N$	→	$2NH$
10	$N_2 + H_2$	→	$NH_2 + N$	23	$NH_2 + N_2$	→	$2NH + N$
11	$N_2 + NH_4^+$	→	$2NH_2 + N$	24	$N_2 + H_2$	→	$2NH$
12	$N_2 + NH_4^+$	→	$NH_2 + 2NH$	25	$N_2 + NH_4^+$	→	$2NH + NH_2^+$
13	$N_2 + NH_3$	→	$NH_2 + N_2H$	26	$N_2 + NH_4^+$	→	$3NH + H^+$

6.4 Discussion

The complex underlying physical and chemical processes occurring in plasmas are further complicated by inclusion of a substrate that can impact both gas-phase and gas-surface reactions. As discussed previously, even relatively simple systems such as the NH_3 plasmas studied here consist of an ensemble of both neutral and ionic species that interact with each other and with the TiO_2 substrates we are seeking to modify.[22] Thus, to understand the NH_x gas-phase densities and surface scatter coefficients measured here, we consider important gas phase and surface reactions with the aim of clarifying pathways for species formation and loss.

Gas-Phase Density and Production Pathways. The gas-phase production of NH_2 in NH_3 plasmas increases significantly as P_{eq} is increased from ~5 to 70 W, Figure 6.1a. NH_2 production can increase by either an increase in reactant concentration(s), an increase in collision rate and energy, activation of new production reaction pathways, and/or deactivation of consumption reaction pathways. Table 6.3 lists possible NH_2(g) producing reactions that can occur in NH_3 plasmas. From our LIF and OES data, we note that peak densities for NH_2, NH_2^*, and H_2^* occur at P_{eq} = 70 W. At lower P_{eq}, N_2^* density decreases, and plateaus at higher P_{eq}, Figure 6.3a. This suggests that H_2 production and N_2 consumption reactions (e.g. Reactions 1, 3-5 and 10-13 in Table 6.3) contribute to NH_2 density in these plasmas. Additionally, the strong correlation of NH_2^* with H_2^*, Figure 6.3b, suggests Reactions 1, 3, and 4 are significant. The decrease in NH_2 density at P_{eq} > 70 W could be a result of increased NH_2 consumption from Reactions 20-23. Similarly, the increase in density around P_{eq} = 70 W for H_α^*, N^*, and NH^* species could result from Reactions 14, 16-17, 19 and 24-26 in Table 6.3 or through other gas phase

reactions not listed in Table 6.3. If their production is not tied to NH_2 production reactions, then the equilibrium would shift Reactions 2, 4-7, and 9-12 to the left, resulting in NH_2 consumption.

Table 6.3 also contains a list of relevant NH(g) producing reactions, which affords additional insight into the gas-phase trends seen in our OES and LIF data. The observation that the maximum H_α^* density occurs at P_{eq} = 105 W demonstrates that H production continues after NH_2 density drops; thus, hydrogen production reactions like Reaction 20 are significant in NH_2 destruction and NH production. The NH_x density data are also consistent with Reaction 20 becoming significant at $P_{eq} \geq 52.5$ W, as NH density rises and the NH_2 density decreases. Additionally, after the H_α^* density maximum, NH production is limited because of the decreased availability of NH_2. Other NH production reactions consistent with our density data include N generation, and H, N_2, and H_2 consumption reactions (e.g. Reactions 16, and 23-26, Table 6.3). Although it is difficult to definitively assign relative importance of individual reactions, in general, unimolecular reactions (e.g. Reactions 14, 15, and 20) are more probable than bimolecular reactions.

As *d.c.* changes, the time allowed for ion generation changes, and reactions that depend on ion content, Reactions 14, 17-18 and 25-26, are affected. Both the N_2^{+*}/N_2^* and N^{+*}/N^* t_{on} data generally increase with *d.c.*, suggesting that indeed ion content increases with *d.c.* With short pulses, however, there may not be enough on time to obtain steady-state N_2^+ generation, as is observed for low *d.c.* conditions with a constant t_{off}. As formation of this ion necessarily requires both decomposition of the plasma feed gas as well as recombination, it is understandable that its formation may be severely repressed in low *d.c.* plasmas (constant t_{off}). Short plasma pulses will typically have an increase in

reactions involving radicals instead of ions when averaged over the entire treatment time because radicals decay slower than ions during t_{off}.[16] Once the plasma pulses off, it changes from an ionization to a recombination system, and an afterglow persists for microseconds to milliseconds.[5] During this afterglow interval, electrons recombine with ions to create neutrals and excited state species.[10, 11] Relative populations of excited state species also change in these regimes. For example, in Ar plasmas, lower excited states are more populated during initial plasma ignition, and higher excited states are more populated during the afterglow.[5]

Figure 6.10 depicts the change in density of hypothetical plasma species through one cycle of a plasma pulse. The four traces near Arrow 1 represent changes in densities during the initiation regime. Species created from secondary reactions will have slower rise times than species created from primary reactions. Arrows 2 and 3 denote density profile changes during the afterglow regime that depend on the rate of afterglow reactions and on the species lifetime, respectively. Typically, ions decay quickly and do not exhibit an afterglow peak (Curve b, Figure 6.10).[5, 10] Shortening t_{on}, t_{off}, and overall pulse periods can impact observed LIF and OES signals if a species of interest is affected by either regime. For example, a greater H^* t_{off} - H^* t_{on} difference is seen at low *d.c.* for the H_α^* state than for the higher energy H_γ^* state, Figure 6.6. Examining this from the perspective of different excited state populations suggests that for H atoms, the effects of the initial ionization regime are more pronounced than those in the afterglow regime. Alternatively, the distribution of H excited states result from afterglow recombination with electrons possessing relatively low kinetic energy, contrary to the literature trends found in Ar^*.[5]

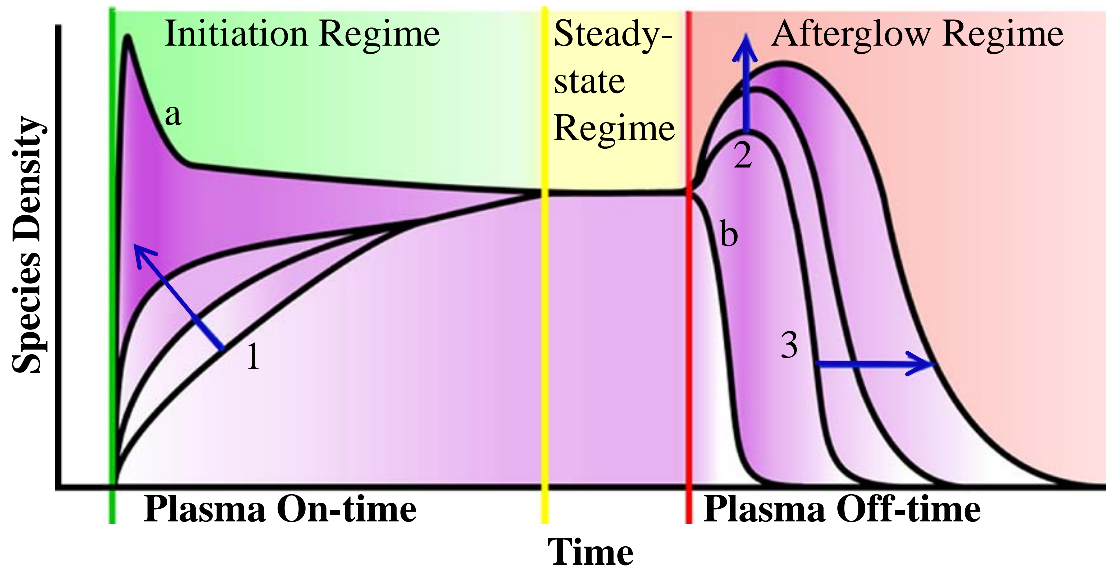

Figure 6.10. A schematic representation of possible species density profiles as a function of time for one pulsed plasma cycle with short t_{on} and t_{off} separated by regime.

The increase in H_α^* at short t_{on}, therefore, likely represents a peak in the initiation regime. Figure 6.6 demonstrates the different behavior of higher excited states of the same species at short t_{on}. Because Reaction 2 is significant, trends in NH_2 ground state data are used to approximate trends in ground state H densities. Here, H_α^* and H_β^* represent trends in ground state H density better than H_γ^*. This analysis shows that monitoring multiple excited states of the same species and applying LIF to confirm ground state trends helps clarify important reactions in plasmas.

An important difference between OES and LIF measurements is that OES examines excited states which emit primarily during the plasma glow period, whereas LIF signals are collected over the entire pulsing period. The difference observed between the NH_2 LIF data taken with constant t_{off} and t_{on}, Figure 6.4a, is not duplicated in its counterpart OES data, Figure 6.5a. There is a very slight increase in the NH_2^* t_{off} data compared to the NH_2^* t_{on} data at $d.c. \leq 20\%$, but the overall discrepancy between the LIF and OES data is attributed to both non-radiative decay pathways for NH_2^* relative to other plasma species and additional NH_2 density created during t_{off}. OES measurements also do not reflect the higher densities of NH_2 at low *d.c.* and constant t_{off} conditions because they cannot probe species during t_{off}. In the afterglow regime, it is possible that electron recombination with reactants of Reactions 1 and 7 produce NH_2 and H_x. In the initiation regime, the decomposition of NH_3 (Reaction 2) increases NH_2 density. Note that this trend in ground state NH_2 t_{off} correlates with the H_α^* t_{off} data, validating the importance of reactions producing both NH_2 and H (Reaction 2) and, therefore, the connection between ground state H densities and excited state H_α^* densities.

Species other than H_α^* and NH_2 affected by short t_{on} include N_2^*, N_2^{+*}, N^*, NH^*, and NHc^*. N_2^* has a higher density at constant t_{off} conditions and the others have lower densities than their constant t_{on} counterparts. The higher N_2^* densities in 10-20% *d.c.* plasmas and the coinciding N_2^* t_{on} and t_{off} densities in higher *d.c.* plasmas demonstrate that enhanced production of N_2^* occurs in the initial ionization regime or in a short-lived (< 3 ms) peak in the afterglow regime. N_2^* production is partially attributed to N_2^+ ion-electron recombination and N+N recombination, because both N_2^{+*} and N^* decrease in intensity at short t_{on}.

Depending on the ionization mechanism and ionized species, there is either a peak (Curve a, Figure 6.10) or a gradual rise in ion production during the initiation regime that lasts μs to ms (Arrow 1, Figure 6.10).[6, 28] A gradual rise in N_2^{+*} during the initiation regime and diminutive afterglow density explain the significantly lower relative densities at shorter pulse periods, Figure 6.5b. N^{+*} is not similarly affected by short pulses, suggesting either it does not increase in density during the plasma pulse or it establishes steady-state conditions considerably faster than 3 ms. N^* intensity decreases slightly at short t_{on} for *d.c.* < 50% because it has an initiation rise time. It also has little afterglow density because of the low contribution from ion-electron recombination of N^+, and its high reactivity to form N_2 during t_{off}.

NH density differences between LIF and OES data, Figures 6.4b and 6.5, provide insight into its temporal density profile at short t_{on} and t_{off}. The incongruity between the behavior of the triplet ground and excited states of NH is attributed to an increase in NH production during t_{off} not monitored by OES. NH LIF data for constant t_{off} conditions show a higher density for 90% *d.c.* plasmas compared to the NH t_{on} data. The longer t_{on}

of 270 ms increases NH production compared to the shorter 30 ms t_{on} and 3 ms t_{off}. Focusing on t_{off} values can explain this behavior as the short t_{off} extinguishes the afterglow peak where NH production is enhanced. Thus, the NH density for the constant t_{on} conditions is limited relative to that for the constant t_{off} experiments. Figure 6.1b data support this hypothesis if we assume the larger spread in LIF density between the high and low values of the NH (70% *d.c.*) results from larger NH densities found in pulsed plasmas compared to CW plasmas (100% *d.c.*).

The OES data also agree with this hypothesis. NH^* t_{off} decreases in intensity at short t_{on} because the rise in NH radical density during the pulse initiation regime is slow and short t_{on} will reduce the NH density. This effect is more dramatic at higher energy levels as demonstrated by the NHc^* data, which behaves similarly to the N_2^{+*} data, Figure 6.5b. Both observations are attributed to the slow rise time of their densities during pulse initiation. This information gives more weight to Reactions 14 or 20 (as opposed to Reaction 15) as being significant NH production reactions because they rely on the production of NH_4^+ or NH_2 first. Although varying P_{eq} by changing P_p affects gas-phase species more significantly than by changing *d.c.*, small t_{on} and t_{off} values can be used in conjunction with applied plasma power to have more control over NH_2, NH, N_2, N_2^+, and N densities. Thus, *d.c.* has little to do with the activation energy of specific gas-phase reactions, although it may have more influence on surface reactions, ion flux, and/or ion bombardment energy.

Surface Production Reactions. Data in Tables 6.1 and 6.2 suggest that surface production of NH_2 is not affected by the composition or morphology of TiO_2 substrates.

The IRIS apparatus is evacuated with diffusion pumps containing polyphenyl ether based oil; thus, during pumpdown (>10 min) carbon can adsorb on the TiO_2 surface. Although we have previously measured small amounts of carbon on our IRIS substrates (comparable to adventitious carbon), this is the first time we have observed such a dramatic change in the surface composition of our substrates. Hence, we attribute the changes in surface composition of TiO_2 to the oleophilic nature of amphiphilic TiO_2, which also makes it a good photocatalyst.[29] Additional changes in the thickness of this carbon layer induced by changes in P_p and *d.c* do not significantly change scatter coefficient values. Notably, carbon adsorption is enhanced by interactions with the molecular beam that generally increase with P_{eq}. This could result from the increased doping susceptibility of reduced TiO_2 in the presence of trace amounts of oil vapor. NH_3 plasmas can reduce the surface of TiO_2 substrates, causing them to appear darker, and reduced TiO_2 surfaces are more susceptible to N doping.[3] High resolution Ti_{2p} XPS spectra of IRIS substrates, however, showed no evidence of reduced surfaces, although the substrates likely oxidize somewhat upon exposure to air. Decreases in oxygen content are correlated with increases in both carbon and the O/Ti ratio, Tables 6.1 and 6.2, indicating a higher surface contamination of polyphenyl ether. The decrease in % C and O/Ti ratio at 90% *d.c.* signifies some carbon sputtering may be occurring. TiO_2 carbon doping is unlikely as Ar sputtering dramatically reduces the surface carbon content of these films, indicating the carbon is primarily at the surface and does not penetrate the TiO_2 network. Changes in morphology from mesoporous to compact films had very little effect on $S(NH_x)$, as the steady-state nature of the IRIS experiments does not allow us to discern small (e.g. μm-level) changes in scattering. Surface interactions measured do not arise from neat TiO_2 surfaces; there-

fore for the purposes of the remainder of this discussion, we will refer to these substrates as carbonaceous TiO_2.

As discussed previously,[21, 22] predominant NH_2 surface generation reactions include processes 6.27-6.29,

$$NH(g) + H(ads) \rightarrow NH_2(g) \quad (6.27)$$

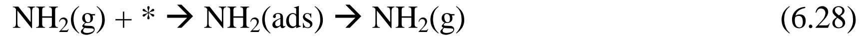

$$NH_2(g) + * \rightarrow NH_2(ads) \rightarrow NH_2(g) \quad (6.28)$$

$$NH_3(g) + 2* \rightarrow NH_2(ads) + H(ads) \rightarrow NH_2(g) + H(ads) \quad (6.29)$$

where the asterisk represents an active site on the substrate. Here, both $S(NH_2)$ and $S(NH)$ increase with increasing P_{eq}. LIF and OES data show H, NH_2, NH, and N densities all increase with P_p and then plateau, whereas H, H_2, NH, and NH_2 values increase with *d.c.* Surface reactions involving these species as reactants, therefore, likely contribute to surface production of NH_2 and NH. Reaction 6.27 accounts for NH_2 production at the surface as increasing NH and H flux to the surface at higher P_{eq} allows more NH and H surface reactions. The jump in $S(NH_2)$ values at P_p = 200 W correlates with the higher density of NH (Figure 6.8) under these conditions because Reaction 6.27 indicates NH is the limiting reagent. The peaks in $S(NH_2)$ at P_p = 100 and 250 W are attributed to processes such as Reaction 6.28, where the fraction of surface-reactant NH_2 molecules is reduced because of increase in [NH_2 (g)] in these plasmas. $S(NH_2)$ t_{off} values are marginally higher than $S(NH_2)$ t_{on} values for *d.c.* < 90%, paralleling the trend observed for NH t_{off} densities. At *d.c.* = 90%, the NH t_{off} density dramatically increases, but $S(NH_2)$ t_{off} values do not. At this point the number of reactions per NH molecule is low because H(ads) becomes the limiting reagent in Reaction 6.27, as a result of comparatively insufficient gains in H density. The increasing NH_2 flux to the surface (Figure 6.4a) also aids in H

extraction in the reverse of Reaction 6.29 to limit Reaction 6.27. Reaction 6.29 mainly depends on the activation of the substrate because NH_3 flux is relatively constant with changing P_{eq} values, and an increase in products would drive the reaction toward reactants.

The power dependence of $S(NH_2)$ on carbonaceous TiO_2 substrates is similar to the power dependence measured on Cu and Pt substrates, with $S(NH_2)$ reaching plateaus of ~1.4 and ~1.2, respectively, at $P_{eq} > 125$ W.[21] Note that these previously measured values were corrected for differences in translational and rotational temperatures for the incident and scattered NH_2. This is relevant because ion impact imparts translational energy to scattered NH_2, resulting in higher observed $S(NH_2)$. For comparison uncorrected $S(NH_2)$ values plateau at ~1.6 using carbonaceous TiO_2 substrates, very close to the values observed with the metal substrates.

The decrease in $S(NH_2)$ values under ion limited conditions (g.m. data), Figure 6.9a, correlates with a decrease in density of H(abs) with increasing *d.c.* Notably, previous work in our laboratory demonstrated ion density through the g.m. increases as P increases,[22] as do NH_x^+/NH_4^+ ($x \leq 3$) ratios. This, coupled with Reaction 6.27, explains the decrease in $S(NH_2)$ under ion limited conditions. At *d.c.* = 30%, few NH_x^+ ions penetrate the g.m. to extract H from the surface; therefore, Reaction 6.27 proceeds unhindered and an increase in $S(NH_2)$ results. As *d.c.* increases, the number of NH_x^+ ions that penetrate the g.m. increases, and the projected removal of H(abs) that occurs as they impinge on the substrate, results in lower $S(NH_2)$. At *d.c.* = 90% we measure significantly lower $S(NH_2)$ values using the g.m., similar to what was seen by Steen and coworkers using CW plasmas and Pt substrates.[22] At *d.c.* = 90%, ion densities in the IRIS molecular

beams could be high enough to affect translational energies of scattered species, as was observed in CW plasmas. Future work in our laboratory will explore this hypothesis further.

Steen and coworkers hypothesized that ultimately the gas-phase densities of plasma species control surface interactions of NH on Pt substrates.[22] As noted above, S(NH) values generally increase with both P_p and *d.c.* The H_α^*, NH_2, NH, and N^* densities all increase and then plateau with P_p whereas H_α^*, H_2^*, NH, and NH_2 values increase with *d.c.* NH_2 flux would affect NH production if Reaction 6.27 was strongly reversible. The large increases in H and NH_2 at $P_p \approx 100$ W, however, do not appear to concomitantly increase S(NH) values, suggesting the reverse of Reaction 6.27 is not favorable. The similar dependences of NH densities and S(NH) on P_p indicate that an increase in NH density boosts NH surface scatter, which would happen if the fraction of NH reacting with H_x(ads) was reduced. Support for this argument comes from the observation that the total H density diminishes at higher P_p. Thus, more impinging NH molecules are scattered off the surface. $S(NH_2)$ values increase by increasing surface-reactant NH flux whereas S(NH) values are increased by increasing the number of unreactive NH radicals. The increase in H with *d.c.* is hypothesized to be less than that for NH; therefore the increase of S(NH) for *d.c.* = 30-70%, Figure 6.9b, corresponds directly to the NH density. The S(NH) values for *d.c.* = 70% and 90% are linked to the respective insignificant change in NH t_{on} densities and increase in H density. The relatively high S(NH) value at *d.c.* = 10% may arise from a lower density of active sites on the substrate, resulting in more NH scatter. An increase in N density directly affects S(NH) values through recom-

bination with H at the substrate, but the relative density of N makes this a less significant reaction than direct NH scatter.

Another reaction that influences NH scatter, process 6.30,[22] where x = 2 or 3, accounts

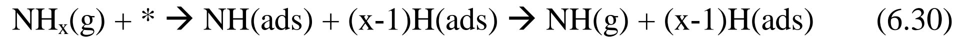

$$NH_x(g) + * \rightarrow NH(ads) + (x\text{-}1)H(ads) \rightarrow NH(g) + (x\text{-}1)H(ads) \qquad (6.30)$$

for processes involving adsorbed NH_3 and NH_2 species, and relies on surface activation. Under ion limited conditions, *S*(NH) increases at low *d.c.*, Figure 6.9b, because fewer active sites are created on the substrate. At higher *d.c.*, ion density in the molecular beam increases and more reactive sites are created, thereby decreasing *S*(NH) relative to that measured with full ion bombardment. Given this dichotomy, it is likely that Reaction 6.30 is not as significant in determining overall NH scatter under these plasma conditions.

6.5 Summary

Ground and excited state density data from LIF and OES data complement each other in studying effects of P_p and *d.c.* in pulsed NH_3 plasmas. These trends help decipher plasma-surface interactions and could suggest optimal plasma conditions for specific nitriding plasma processes, especially those related to photocatalytic TiO_2. Unimolecular reactions such as Reactions 1, 2, 15, and 20 in Table 6.3, are highlighted as major NH_2 and NH producing pathways in these pulsed plasmas, and a connection between NH_2 and NH densities through Reaction 20 was further verified. Experiments holding t_{on} or t_{off} times constant resulted in clear trends that were described in terms of a plasma initiation regime yielding a steady-state density at longer t_{on} for NHc^*, N_2^{+*}, NH^*, N^*, and H_γ^* spe-

cies and a long-lived peak in NH density in the plasma afterglow regime. NH_2 data suggest density contributions from both peaks in the initiation and afterglow regimes, but the afterglow peak is not as long-lived as the NH afterglow peak. The results of these gas-phase density measurements and IRIS surface interaction data lead to the observation that $S(NH_2)$ and $S(NH)$ measured on carbonaceous TiO_2 substrates are both significantly correlated to several gas-phase species in NH_3 plasmas. Ion densities changed by varying *d.c.* and using a g.m. affect both $S(NH_2)$ and $S(NH)$ by altering gas-phase densities and concentrations of adsorbed surface species. Ultimately, the IRIS values measured here indicate neither NH nor NH_2 are largely responsible for direct N implantation into TiO_2 materials. This suggests some other N-containing species (e.g. N atoms, N_2 or NH_3) may be responsible for direct N doping. Our data do not, however, eliminate the possibility that NH_x species contribute to the nitridation process in an indirect way.

6.6 References

1. Henderson, M. A., A surface science perspective on TiO_2 photocatalysis. *Surface Science Reports* **2011,** *66* (6-7), 185-297.
2. Maeda, K.; Domen, K., Oxynitride materials for solar water splitting. *MRS Bulletin* **2011,** *36*, 25-31.
3. Pulsipher, D. J. V.; Martin, I. T.; Fisher, E. R., Controlled nitrogen doping and film colorimetrics in porous TiO_2 materials using plasma processing. *ACS Applied Materials & Interfaces* **2010,** *2* (6), 1743-1753.
4. Pulsipher, D. J. V.; Fisher, E. R., O_2 plasma treatment of mesoporous and compact TiO_2 photovoltaic films: Revealing and eliminating effects of Si incorporation. *Surface & Coatings Technology* **2009,** *203* (16), 2236-2242.
5. Jackson, G. P.; King, F. L., Bulk plasma properties in the pulsed glow discharge. *Spectrochimica Acta, Part B* **2003,** *58* (8), 1417-1433.
6. Lewis, C. L.; Oxley, E. S.; Ban, C. K.; Steiner, R. E.; King, F. L., Determination of Ca-40(+) in the presence of Ar-40(+): An illustration of the utility of time-gated detection in pulsed glow discharge mass spectrometry. *Analytical Chemistry* **1999,** *71* (1), 230-234.
7. Agarwal, A.; Stout, P. J.; Banna, S.; Rauf, S.; Collins, K., Recouping etch rates in pulsed inductively coupled plasmas. *Journal of Vacuum Science and Technology A* **2011,** *29* (1).
8. Lotito, G.; Nelis, T.; Guillot, P.; Gunther, D., Characterization of argon metastable species as function of time, space, and current of a pulsed dc glow discharge. *Spectrochimica Acta, Part B* **2011,** *66* (8), 619-626.
9. Kang, N.; Gaboriau, F.; Oh, S. G.; Ricard, A., Modeling and experimental study of pulse modulated ICP discharge: production of Ar highly excited states. *Plasma Sources Science and Technology* **2011,** *20* (3).
10. Kang, N.; Britun, N.; Oh, S. G.; Gaboriau, F.; Ricard, A., Experimental study of Ar and Ar-N(2) afterglow in a pulse-modulated ICP discharge: observation of highly excited Ar(6d) afterpeak emission. *Journal of Physics D: Applied Physics* **2009,** *42* (11).
11. Bogaerts, A., The afterglow mystery of pulsed glow discharges and the role of dissociative electron-ion recombination. *Journal of Analytical Atomic Spectrometry* **2007,** *22* (5), 502-512.
12. Hu, D. W.; Pu, Y. K., Experimental investigation of emission intensities in an inductively coupled afterglow neon plasma. *Journal of Physics D: Applied Physics* **2009,** *42* (11).
13. Brockhaus, A.; Leu, G. F.; Selenin, V.; Tarnev, K.; Engemann, J., Electron release in the afterglow of a pulsed inductively-coupled radiofrequency oxygen plasma. *Plasma Sources Science and Technology* **2006,** *15* (2), 171-177.
14. Alberts, D.; Horvath, P.; Nelis, T.; Pereiro, R.; Bordel, N.; Michler, J.; Sanz-Medel, A., Time-resolved measurement of emission profiles in pulsed radiofrequency glow discharge optical emission spectroscopy: Investigation of the pre-peak. *Spectrochimica Acta, Part B* **2010,** *65* (7), 533-541.
15. Cunge, G.; Vempaire, D.; Sadeghi, N., Gas convection caused by electron pressure drop in the afterglow of a pulsed inductively coupled plasma discharge. *Applied Physics Letters* **2010,** *96* (13).

16. Kawai, Y.; Ikegami, H.; Sato, N.; Matsuda, A.; Uchino, K.; Kuzuya, M.; Mizuno, A., *Industrial Plasma Technology: Applications from Environmental to Energy*. Whiley-VCH: 2010; p 23-24.
17. Stillahn, J. A.; Trevino, K. J.; Fisher, E. R., Plasma diagnostics for unraveling process chemistry. In *Annual Review of Analytical Chemistry*, Annual Reviews: Palo Alto, 2008; Vol. 1, pp 261-291.
18. McCurdy, P. R.; Venturo, V. A.; Fisher, E. R., Velocity distributions of NH_2 radicals in an NH_3 plasma molecular beam. *Chemical Physics Letters* **1997,** *274* (1-3), 120-126.
19. Fisher, E. R., On the interplay between plasma ions, radicals and surfaces: who dominates the interaction? *Plasma Sources Science and Technology* **2002,** *11* (3A), A105-A112.
20. McCurdy, P. R.; Butoi, C. I.; Williams, K. L.; Fisher, E. R., Surface interactions of NH_2 radicals in NH_3 plasmas. *Journal of Physical Chemistry B* **1999,** *103* (33), 6919-6929.
21. Butoi, C. I.; Steen, M. L.; Peers, J. R. D.; Fisher, E. R., Mechanisms and energy transfer for surface generation of NH_2 during NH_3 plasma processing of metal and polymer substrates. *Journal of Physical Chemistry B* **2001,** *105* (25), 5957-5967.
22. Steen, M. L.; Kull, K. R.; Fisher, E. R., Comparison of surface interactions for NH and NH_2 on polymer and metal substrates during NH_3 plasma processing. *Journal of Applied Physics* **2002,** *92* (1), 55-63.
23. McCurdy, P. R.; Bogart, K. H. A.; Dalleska, N. F.; Fisher, E. R., A modified molecular beam instrument for the imaging of radicals interacting with surfaces during plasma processing. *Review of Scientific Instruments* **1997,** *68* (4), 1684-1693.
24. Bogart, K. H. A.; Cushing, J. P.; Fisher, E. R., Effects of Plasma Processing Parameters on the Surface Reactivity of $OH(X^2\Pi)$ in Tetraethoxysilane/O_2 Plasmas during Deposition of SiO_2. *Journal of Physical Chemistry B* **1997,** *101* (48), 10016-10023.
25. Labelle, C. B.; Gleason, K. K., Pulsed plasma deposition from 1,1,2,2-tetrafluoroethane by electron cyclotron resonance and conventional plasma enhanced chemical vapor deposition. *Journal of Applied Polymer Science* **2001,** *80* (11), 2084-2092.
26. Fuller, N. C. M.; Malyshev, M. V.; Donnelly, V. M.; Herman, I. P., Characterization of transformer coupled oxygen plasmas by trace rare gases-optical emission spectroscopy and Langmuir probe analysis. *Plasma Sources Science and Technology* **2000,** *9* (2), 116-127.
27. Trevino, K. J.; Fisher, E. R., Detection limits and decomposition mechanisms for organic contaminants in water using optical emission spectroscopy. *Plasma Processes and Polymers* **2009,** *6* (3), 180-189.
28. Fridman, A., *Plasma Chemistry*. Cambridge University Press: Cambridge, 2008; p 570-571.
29. Masao Kaneko, I. O., *Photocatalysis: science and technology*. Springer: 2002; p 114-118.

CHAPTER 7

RESEARCH SUMMARY AND PERSPECTIVES

This chapter reviews some significant findings discovered through this work and explores interesting areas where further research could be concentrated.

7.1 Research Summary

The many uses of plasmas and of TiO_2 have been brought together in this dissertation. TiO_2 materials can be plasma modified whether in compact or mesoporous films. We demonstrate how etching (Chapters 3 and 5), deposition (Chapters 3, 5, and 6), and functionalization (Chapters 3 and 4) occurs in plasmas treating TiO_2. Oxygen plasmas can be used to clean TiO_2 from carbon contaminants and sputter Si onto TiO_2 at higher powers. HMDSO plasmas can be used to coat TiO_2 with an SiO_2 layer while still preserving the underlining modification. O_2 plasma sputtering is averted by using pulsed plasmas. Nitrogen-containing plasma precursors can be used to incorporate five different nitrogen binding environments into TiO_2 materials. Ammonia plasmas can controllably saturate TiO_2 surfaces with nitrogen by varying plasma *d.c.*

We learned that TiO_2 is more susceptible to nitrogen doping when it is first reduced through the ammonia and hydrogen plasma studies. Through the IRIS experiments we discovered that TiO_2 is more susceptible to carbon contamination and/or

doping in the IRIS environment while in contact with a reducing plasma. This information can be applied to aid in doping TiO_2 with other species to improve the many devices that involve TiO_2.[1]

The photodevices created in this work show that plasma treatments affect charge recombination and transportation. Photocatalytic experiments show that the UV photocatalytic activity of P25 is diminished by nitrogen plasma treatments. The visible light photocatalytic activity is often reported for N:TiO_2 materials, but the unreported UV light photocatalytic activity of these materials is most likely diminished. Through the visible light experiments performed in this work we learned that these materials have either too many recombination centers, a light absorption mechanism that does not create electron hole pairs, or that photons with lower energy are not able to decompose RhB dye. Burying the surface defects of N:TiO_2 materials with an HMDSO plasma treatment is beneficial for these films and could prove valuable for other plasma treatments of P25. The photovoltaic experiments show that NH_3/O_2 treated films have promise to improve photovoltaic efficiencies by increasing the absorption of the solar cell and increasing charge transport, but the decrease in V_{oc} values (induced by trap states) hinder the device for materials examined.

Through the IRIS experiments we have determined that NH_2 and NH radicals are excessively produced at the TiO_2 surface with scatter coefficients exceeding 2.0. This work also gives insights into gas phase densities of NH_3 plasmas. Both NH_2 and NH scatter coefficients are dependent on gas phase neutral and ionic species densities. From trends in these densities with changing plasma parameters important gas phase and

surface reactions are deduced. The IRIS, LIF, and OES experiments performed in this work will aid in tailoring NH_3 plasma for treating a wide range of substrates.

In addition to determining gas phase densities of species in NH_3 plasmas, a steady-state LIF and OES techniques have been developed to determine the behavior of plasma species at short plasma pulses. This technique is effective in characterizing the benefits and added control of pulsed plasmas using short plasma pulses. NH_3 plasmas show low unequilibrated densities for NHc^*, N_2^{+*}, NH^*, N^*, and H_γ^* species that occur in the plasma initiation regime. Thus, short plasma on-times can be chosen to reduce the reactions involving these species. In contrast, NH densities are greatly enhanced in the afterglow regime of the plasma and a plasma *d.c.* can be selected to take advantage of this effect.

7.2 Future Directions

As with many scientific investigations, a few answers are often accompanied with a plethora of new questions and new intriguing avenues of research. There are still some holes in the plasma research of nitriding TiO_2. There are nitrogen binding environments that need more exploration. For example, the XPS N1s peak at 398 eV was often accompanied by other nitrogen binding environments and therefore there was no solid assignment given to this peak. The urea plasma treatments lead to a 400 eV N1s peak that was characterized and assigned, but other groups have found a 400 eV N1s peak that is attributed to interstitial species instead of surface adsorbed species.[2] There are a lot of other dopants, co-dopants, and heterostructures that can be used to improve TiO_2

photocatalysis including anions and cations, and there are many people that are doing this research.[3, 4] As stated in Chapter 4 the method of doping TiO_2 drastically affects its performance in photodevices, so there is still room for more research in using plasmas to dope TiO_2 materials to compare plasma doping with other doping methods. Although, in order to move forward with TiO_2 doping and photocatalysis research one must stay closely informed of the many relevant studies performed. As stated previously, in this dissertation these photocatalytic studies were performed not to find the best photocatalyst, but to help understand the treated materials.

The work on photovoltaic devices begun in Chapter 5 has not been completed. Since initiating this photovoltaic work other groups have reported improvements in DSSCs using N:TiO_2 photoanodes.[5-9] In finishing the work begun on DSSCs in this dissertation one could compare and contrast the effects of the different preparation conditions and the effects of the different binding environments on the DSSCs. There have also been studies investigating the passivation of photoanodes by using thin oxide layers like Al_2O_3[10] and SiO_2.[11] Yet one could conceivably take advantage of the increased J_{sc} from N:TiO_2 photoanodes and the decreased back electron transfer from an SiO_2 coatings using plasma treatments similar to those outlined in this dissertation. Additionally, intermixing Si into the TiO_2 matrix would have a different effect than coating the DSSC with SiO_2 by using the O_2 and HMDSO plasmas used in this work. There have been further studies that have investigated other dopants to improve the TiO_2 based photoanodes of DSSCs like those investigating F codoping,[12] N and B codoping,[13] B doping,[14] Al and W codoping,[15] and others; yet, the list of doped TiO_2 materials for photovoltaics is not nearly as long as the list for doped TiO_2 materials for photocatalyst.

There are plenty of opportunities for further research in the basic chemistry of photodevices using wide band gap oxides and it is a fast moving field.

The novel technique used in this work to examine plasma densities at short pulse durations opens up many possibilities for future research. Knowing how species behave at short plasma pulses will allow plasma chemists more control in enhancing the balance between plasma etching, deposition, and functionalization. Upon discovering this technique, our interest was generated to examine multiple plasma systems and draw correlations between the different plasma systems and plasma species that behave differently in either the initiation or afterglow regimes of the plasma. There has been little work in the plasma community on the behavior of species in the initiation and afterglow regimes of plasmas (Ar, Ne, O_2, and Ar-based sputtering discharges) as mentioned in Chapter 6. The short-pulse behavior of species in other plasma precursors such as N_2, H_2O, HMDSO, acrylic acid, allylamine, SF_6, CF_4 and others could be studied to allow the determination of the optimized pulsed plasma parameters.

The IRIS work presented in this dissertation has only been performed on TiO_2 substrates. There are other metal oxide materials including ZnO, Ta_2O_5,[16] Al_2O_3, and P_2O_5 that can be plasma nitrided for a variety of applications ranging from photodevices, hard coatings, and flame retardants. The behavior of NH and NH_2 radicals on these other oxide material surfaces will allow broader conclusions to be made about the roles of NH and NH_2 radicals. Additionally, atomic fluorescence and absorption spectroscopy would be intriguing to use in examining other species of interest in these plasma nitriding systems if the analysis can be configured to allow lower wavelengths: 206.7 nm for excitation of nitrogen (N(2p3 4S3/2) → N(3p 4S3/2)).[17]

7.3 References

1. Chen, X. B., Titanium dioxide nanomaterials and their energy applications. *Chinese Journal of Catalysis* **2009,** *30* (8), 839-851.
2. Emeline, A. V.; Kuznetsov, V. N.; Rybchuk, V. K.; Serpone, N., Visible-light-active titania photocatalysts: the case of N-doped TiO_2: Properties and some fundamental issues. *International Journal of Photoenergy* **2008,** *2008*.
3. Liu, G.; Wang, L. Z.; Yang, H. G.; Cheng, H. M.; Lu, G. Q., Titania-based photocatalysts-crystal growth, doping and heterostructuring. *Journal of Materials Chemistry* **2010,** *20* (5), 831-843.
4. Teh, C. M.; Mohamed, A. R., Roles of titanium dioxide and ion-doped titanium dioxide on photocatalytic degradation of organic pollutants (phenolic compounds and dyes) in aqueous solutions: A review. *Journal of Alloys and Compounds* **2011,** *509* (5), 1648-1660.
5. Kim, S. R.; Al-Mamun, M.; Ko, Y. H., Surface modification and retardation of back reaction by nitrogen ion-beam treatment in dye-sensitized solar cells. *Chemical Physics Letters* **2012,** *538*, 77-81.
6. Guo, W.; Shen, Y. H.; Boschloo, G.; Hagfeldt, A.; Ma, T. L., Influence of nitrogen dopants on N-doped TiO_2 electrodes and their applications in dye-sensitized solar cells. *Electrochimica Acta* **2011,** *56* (12), 4611-4617.
7. Guo, W.; Wu, L. Q.; Chen, Z.; Boschloo, G.; Hagfeldt, A.; Ma, T. L., Highly efficient dye-sensitized solar cells based on nitrogen-doped titania with excellent stability. *Journal of Photochemistry and Photobiology a-Chemistry* **2011,** *219* (2-3), 180-187.
8. Kang, S. H.; Kim, H. S.; Kim, J. Y.; Sung, Y. E., Enhanced photocurrent of nitrogen-doped TiO_2 film for dye-sensitized solar cells. *Materials Chemistry and Physics* **2010,** *124* (1), 422-426.
9. Tian, H. J.; Hu, L. H.; Zhang, C. N.; Liu, W. Q.; Huang, Y.; Mo, L.; Guo, L.; Sheng, J.; Dai, S. Y., Retarded charge recombination in dye-sensitized nitrogen-doped TiO_2 solar cells. *J. Phys. Chem. C* **2010,** *114* (3), 1627-1632.
10. Lin, C.; Tsai, F. Y.; Lee, M. H.; Lee, C. H.; Tien, T. C.; Wang, L. P.; Tsai, S. Y., Enhanced performance of dye-sensitized solar cells by an Al_2O_3 charge-recombination barrier formed by low-temperature atomic layer deposition. *Journal of Materials Chemistry* **2009,** *19* (19), 2999-3003.
11. Mohan, V. M.; Shimomura, M.; Murakami, K., Improvement in performances of dye-sensitized solar cell with sio_2-coated TiO_2 photoelectrode. *Journal of Nanoscience and Nanotechnology* **2012,** *12* (1), 433-438.
12. Yang, S. M.; Xue, H. B.; Wang, H. J.; Kou, H. Z.; Wang, J. C.; Zhu, G. H., Improved efficiency of dye-sensitized solar cells applied with nanostructured N-F doped TiO_2 electrode. *Journal of Physics and Chemistry of Solids* **2012,** *73* (7), 911-916.
13. Tian, H. J.; Hu, L. H.; Zhang, C. N.; Mo, L.; Li, W. X.; Sheng, J.; Dai, S. Y., Superior energy band structure and retarded charge recombination for Anatase N, B codoped nano-crystalline TiO_2 anodes in dye-sensitized solar cells. *Journal of Materials Chemistry* **2012,** *22* (18), 9123-9130.

14. Subramanian, A.; Wang, H. W., Effects of boron doping in TiO_2 nanotubes and the performance of dye-sensitized solar cells. *Applied Surface Science* **2012,** *258* (17), 6479-6484.
15. Ko, K. H.; Lee, Y. C.; Jung, Y. J., Enhanced efficiency of dye-sensitized TiO_2 solar cells (DSSC) by doping of metal ions. *Journal of Colloid and Interface Science* **2005,** *283* (2), 482-487.
16. Maeda, K.; Domen, K., Oxynitride materials for solar water splitting. *MRS Bull.* **2011,** *36*, 25-31.
17. Es-Sebbar, E.; Gazeau, M. C.; Benilan, Y.; Jolly, A.; Pintassilgo, C. D., Absolute ground-state nitrogen atom density in a N_2/CH_4 late afterglow: TALIF experiments and modelling studies. *Journal of Physics D-Applied Physics* **2010,** *43* (33).